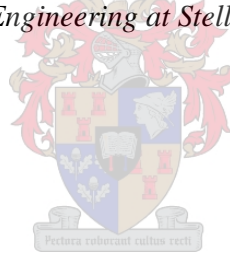# Near-Beta Titanium Alloys Produced Using Laser Powder-Bed Fusion

by

Sabrina Mary-Ann Rudolph

*Thesis presented in partial fulfilment of the requirements for the degree
of Master of Engineering (Mechanical)
in the Faculty of Engineering at Stellenbosch University*

Supervisor: Prof. Thorsten Hermann Becker
Co-supervisor: Dr. Gerrit Matthys Ter Haar

March 2023

Declaration

By submitting this thesis electronically, I declare that the entirety of the work contained therein is my own, original work, that I am the sole author thereof (save to the extent explicitly otherwise stated), that reproduction and publication thereof by Stellenbosch University will not infringe any third party rights and that I have not previously in its entirety or in part submitted it for obtaining any qualification.

Date: March 2023

i

Abstract

β titanium alloys are used extensively in the aerospace industry to fulfil a multitude of applications due to their favorable properties, including the exhibition of high strength, workability, corrosion resistance, interchangeable combinations of strength and toughness, and ability to be heat treated over a wide range.

However, little to no literature is available on the printability and mechanical performance of β titanium alloys subjected to additive manufacturing (AM), which is largely used for rapid prototyping and the production of complex components.

Therefore, in this research, the printability and consequent mechanical performance of two β titanium alloys, viz. Ti-5Al-5V-5Mo-3Cr (Ti-5-5-5-3) and Ti-15Mo-3Nb-3Al-0.2Si (Beta 21S), are considered whereby laser powder bed fusion is the means of manufacture.

The process parameters were optimized experimentally in which the region of experimentation was determined using simulation software. The density was evaluated using the Archimedes' principle. Pores were analyzed using optical microscopy. Additionally, the resulting microstructures were studied using scanning electron microscopy to further characterize the two alloys. The hardness and tensile properties of the as-built samples were investigated. A strong correlation was found between those reported and that of literature.

The results demonstrate performance competitive with traditionally manufactured products, but more complex builds require investigation to alleviate uncertainties regarding the performance thereof. Additionally, the processing windows developed correlate with literature and provide insight into the combinations of process parameters which yield dense parts.

The research presented herein reports the methods used to characterize the printability and mechanical performance demonstrated by commercially available β titanium alloys, Ti-5-5-5-3 and Beta 21S, produced by laser powder bed fusion.

Uittreksel

β-titaanallooie word vir menigte toepassings in die lugvaartindustrie gebruik as gevolg van hul voordelige eienskappe, ondermeer hoë sterkte, werkbaarheid, korrosieweerstandigheid, verwisselbare kombinasies van sterkte en taaiheid, en die vermoë daarvan om oor 'n wye reeks hittes behandel te word.

Daar is egter min literatuur beskikbaar oor die sogenaamde drukbaarheid en meganiese verrigting van β-titaanallooie wat onderworpe is aan additiewe vervaardiging (AV), wat grootliks gebruik word vir vinnige prototipering en die vervaardiging van komplekse komponente.

In hierdie navorsing word die drukbaarheid en gevolglike meganiese verrigting van twee β-titaanallooie, nl. Ti-5Al-5V-5Mo-3Cr (Ti-5-5-5-3) en Ti-15Mo-3Nb-3Al-0.2Si (Beta 21S), oorweeg, met laserpoeierbedsamesmelting as die vervaardigingsmiddel.

Die proses parameters is eksperimenteel geoptimaliseer, waar die gebied van eksperimentering met behulp van simulasie sagteware bepaal is. Die materiaaldigtheid is deur die Archimedes-beginsel bepaal. Porieë is met behulp van optiese mikroskopie (OM) geëvalueer en die resulterende mikrostrukture is met behulp van skandeerelektronmikroskopie (SEM) bestudeer om die twee allooie verder te karakteriseer. Die meganiese eienskappe van die monsters is ondersoek. Dié eienskappe sluit in hardheid en treksterkte. 'n Sterk korrelasie is gevind tussen die eienskappe wat gerapporteer is en dié van die literatuur.

Die resultate toon meganiese werkverrigting aan wat mededingend is met tradisioneel-vervaardigde produkte, maar meer komplekse konstruksies vereis verdere ondersoek om enige onsekerhede oor die werkverrigting daarvan te verklaar. Die verwerkingsgebied wat ontwikkel is, stem ooreen met die literatuur en bied insig in die verskillende kombinasies van prosesparameters wat dig parte lewer.

Hierdie navorsing rapporteer die metodes wat gebruik word om die drukbaarheid en meganiese werkverrigting te karakteriseer wat deur kommersieel-beskikbare β-titaanallooie, Ti-5-5-5-3 en Beta 21S, wat deur laserpoeierbedsamesmelting vervaardig is, gedemonstreer word.

iii

Acknowledgements

The completion of this study could not have been possible without the guidance and expertise of Prof. Thorsten Becker, who supervised this project and organised the funding to meet its completion. His support throughout has been a comfort in the numerous situations where Murphy's Law had reared its ugly head.

Additional thanks is owed to the *Centre for Materials Engineering* at the University of Cape Town, which authorised the use of much of its equipment where the assistance of Penny Louw, the laboratory manager, was always given with such patience and zeal.

A debt of gratitude is owed to my mother, brother and friends for their continuous love, support, and prayer throughout this journey.

Last, but not least, I am thankful to my Lord and Saviour, Jesus Christ, for walking beside me every step of the way and comforting me in my darkest moments. He was my strength when I had needed it most.

Table of Contents

List of Tables

List of Figures

1. INTRODUCTION

The research conducted herein seeks to gain a deeper understanding into the performance of metallic materials produced through Additive Manufacturing (AM) and, consequently, report on the observed relationships between the mechanisms involved therein. The Materials Engineering research group in the *Department of Mechanical and Mechatronic Engineering* at Stellenbosch University, in collaboration with the *Centre for Materials Engineering* (*CME*) at the University of Cape Town, focuses on the development of numerical experiment techniques to obtain material properties and develop material models for predictive capabilities. Additionally, the research group investigates material analysis and characterisation, and seeks to establish links between manufacturing processes, microstructure, and material performance. The group aims to provide expertise in the field by developing the skillset within South Africa.

Much of the research currently carried out pertains to Ti-6Al-4V (Ti-6-4) due to its extensive use in the aerospace and biomedical industries, arising from its high specific strength, corrosion resistance, and biocompatibility. However, the analysis and characterisation of other commercially available titanium alloys are necessary to allow the fulfilment of the multitude of applications available. In this study, Ti–15Mo–3Nb–3Al–0.2Si (Beta 21S) and Ti-5Al-5V-5Mo-3Cr (Ti-5-5-5-3), being metastable and near-β alloys, respectively, are investigated.

Many factors influence material performance within the scope of AM. Therefore, using the information available on Ti-6-4, an efficient means of experimental design, known as D-optimal design, is introduced to establish a processing window as a function of laser power, scan speed, and hatch spacing, which encompass an array of energy density inputs. The processing window is defined using the optimal density criterion. The need to use D-optimal design arises from the evident complex relationships between the aforementioned parameters and achieving dense components. Ultimately, the optimisation of the design space is necessary to quantify the relationship between these parameters and density using nonlinear regression. This approach is applied to Ti-6-4 in which the available literature is used to verify the statistical model.

The design approach is consequently applied to the titanium alloys in question. The material performance of parts within the processing window is determined, whereby the hardness and tensile properties are explored. Additionally, the resulting microstructure is of interest to the study and can be used in conjunction with the processing window to establish links between the process parameters and the resulting microstructure.

The methods used to present the findings of this research were carried out using the equipment and laboratory facilities made available by the department, in conjunction with *MetalHeart* and the *CME*.

The information explored in this research has significant value in the advancement of material characterisation and analysis within the field of AM.

1.1 Background

To minimize costs, reduce energy expenditure, and expand capabilities, manufacturing industries are investigating means to improve manufacturing techniques. Traditional manufacturing methods, such as casting, forging, and machining, are time-consuming endeavours that incur substantial amounts of waste material.

Unlike traditional manufacturing, Laser Powder-Bed Fusion (LPBF), a method of AM techniques, aims to minimize the impact on the environment by reducing the amount of waste material induced and optimizing resource efficiency. Furthermore, the metal powder is reported to be reusable to repeatable extents according to Gokuldoss et al. (2017).

The current market is driven by innovation and competition. Therefore, to meet demands, companies require rapid prototyping. Changes to designs can be easily implemented using AM techniques. LPBF seeks to reduce costs and lead times during the tooling phase of production, giving AM techniques an advantage over traditional manufacturing methods (Fousová et al., 2015).

Additionally, parts with complex geometries and high precision are achievable, granting manufacturers the flexibility to produce optimal parts. Parts can be designed according to customers' unique design requirements without the need for expensive setup arrangements. This also grants manufacturers the opportunity to produce in low volumes, therefore, making AM techniques more cost-effective than traditional manufacturing methods in such applications (Pereira, Kennedy, & Potgieter, 2019). Single unit, low-volume production is implemented in several sectors, ranging from metallic aerospace products to fashion (Pereira, Kennedy, & Potgieter, 2019). Consideration should be given to titanium alloys used in such sectors.

Furthermore, to penetrate the wider commercial market and provide the industry with the confidence that it needs to implement this means of manufacture, a few key requirements must be fulfilled. These include high process stability, continuous certification and provision of design rules, quality control processes, etc. (Pereira, Kennedy, & Potgieter, 2019). The most important of these, related to the topic of investigation, is the need for a database containing the properties of the materials.

As such, this research aims to provide industry with insight into the mechanical performance of dense near-β- and metastable-β-titanium alloys produced using LPBF, along with recommended post-manufacturing processes to improve performance and the mechanisms involved therein. Research can no longer be limited to Ti-6-4 as many major industries, including the aerospace industry, rely on a variety of titanium alloys to fulfil their intended purposes.

The appropriate sources are consulted to understand the microstructure of wrought β-titanium alloys and the necessary post-manufacturing processes required to achieve mechanical properties competitive with those of the wrought counterparts.

The research aims to characterize the printability of these alloys and emulate the properties displayed by their wrought counterparts. The information obtained will be used to expand the database of LPBF-produced, β-titanium alloys.

1.2 β-Titanium Alloys

Currently, there are six β-titanium alloys commercially produced for applications in the aerospace industry, viz. Ti-10V-2Fe-3Al (Ti-10-2-3), Ti-3Al-8V-6Cr-4Mo-4Zr (Beta C), Ti-15V-3Cr-3Al-3Sn (Ti-15-3-3-3), Beta 21S, Ti-5-5-5-3 and Ti-35V-15Cr (Alloy C) (Cotton et al., 2015).

Beta 21S and Ti-5-5-5-3 are investigated in this study due to their availability, use in major industries and favorable properties. Beta 21S offers better oxidation resistance compared to other metastable β-titanium alloys, as well as the ability to retain its strength at elevated temperatures, making it suitable for its application in plug-and-nozzle assemblies. Additionally, this alloy exhibits increased corrosion resistance and the ability to age harden (Macias-Sifuentes et al., 2021). Ti-5-5-5-3, much like Beta 21S, is used in the aerospace industry, specifically in landing gear components. It offers high strength, excellent fatigue resistance, fracture toughness, and hardenability (Sánchez-Amaya et al., 2017).

1.3 Objectives

The research conducted seeks to investigate the parameters to produce β-titanium alloys that are high in density and showcase competitive mechanical properties. As such, the aim is to establish a processing window that outlines combinations of process parameters that produce dense parts. From this processing window, the hardness and tensile properties can be determined and compared to that of wrought counterparts.

The following objectives are considered to meet the outcome of the research.

3

- Use D-optimal design to define a set of processing parameters from which a processing window of dense parts can be determined.
- Characterize hardness and tensile properties found within processing window.
- Establish connections between determined properties and microstructure or other potential influences.
- Make recommendations for property improvements and further study.

1.4 Motivation

Valuable insight can be inferred from the metallurgy of metallic components. This insight can be used to draw conclusions about expected behavior and provide solutions for improvements. From this, appropriate applications can be assigned to fulfil functions. Such insight is especially important in the aerospace, biomedical, and automotive industries because failure to meet design requirements could lead to the endangerment of the end-user. Therefore, it is important to characterize the performance of materials in AM.

Much of titanium's popularity is owed to its high specific strength and its ability to be age hardened. β-titanium alloys are widely used in the aforementioned industries due to these favourable properties, making them viable candidates for AM fabrication. Furthermore, β alloys lower the β-transus temperature by 100 – 200 ºC compared to Ti-6-4 (975 °C) and allow for lower flow stresses due to the high β-phase content since it is generally softer than α-phase. Therefore, less thermomechanical processing is required (Cotton et al., 2015). Less energy would be needed during post-manufacturing heat treatments – potentially for aging.

A vital inhibitory factor for material performance is porosity, which is the result of an inadequate set of process parameters. With an increase in porosity comes a decrease in the elastic modulus, ultimate tensile strength, elongation-to-failure, and most importantly a significant decrease in fatigue strength. Pores increase the stress concentration within the material and behave as initiation sites from which cracks can propagate (Moeinfar et al., 2022).

Consequently, before direct links can be made between the performance and the metallurgy of the material, defects need to be eradicated. However, due to the complex interactions between process parameters and the combinations thereof, it is imperative to develop a processing window detailing combinations of parameters that result in dense components – more specifically, void of defects.

From this, the properties of dense parts achieved using optimal combinations of process parameters can be investigated and reported. Properties investigated include tensile and

4

hardness properties, which are used to assess how the LPBF-produced β-titanium alloys compare to the wrought data and to report the reasons for the differences found, if any.

Furthermore, recommendations for further study can be made. Ultimately, this will provide industry with the information it needs to introduce these β alloys into commercial production using AM techniques.

However, large costs are incurred in acquiring gas- or plasma-atomized, prealloyed metallic powders. Taking into account the complexities and high costs involved, as well as the limited resources available for this study, optimization tools are consulted in which it is sought to optimize the experimental procedure. This is to be done by minimizing the number of samples produced, while maximising the amount of statistically sound data achievable with said number of samples. Additionally, using such tools will hopefully establish an effective means to charaterize processing windows in such cases where resources are limited.

1.5 Scope

The thesis focuses on establishing a processing window to outline a domain of processing parameters responsible for producing dense, β-titanium parts. In the design of the experiment, a statistical tool is implemented to optimize the design space using D-optimality. The result is a surface response that predicts density and can be used to establish the processing window mentioned. From the window of dense parts, the mechanical performance of the β alloys is examined to formulate links between the microstructure and the investigated tensile and hardness properties.

Mechanisms such as dislocation movement and plastic deformation are not considered as they are beyond the scope of the project. In addition to this, heat treatments are not performed; only as-built properties are reported in this research. However, post-manufacturing recommendations are deliberated briefly.

Additional limitations to this study include the equipment and materials used. The only LPBF system made available to this study was the SLM®280HL system (*SLM Solutions*) offered by *MetalHeart*, which implements the use of a hopper coating mechanism, laminar gas flow to ensure a soot-free powder bed, and baseplate heating. Furthermore, only prealloyed powders were considered. Porosity data was determined using Archimedes' density principle, which has limited accuracy, but was considered due to the high volume of samples and limited funding. As such, the implementation of more accurate techniques was not possible. This technique was, however, deemed accurate enough to establish processing windows for the alloys in question.

1.6 Thesis Outline

The contents of the thesis are outlined in this section.

Chapter 2 reviews the relevant literature required for a fundamental understanding of concepts covered in the thesis. This chapter first considers the crystal structure of titanium and the fundamentals of the structure. Additionally, the microstructural characteristics offered by the β-phase are studied, as well as the chemistry of β-titanium alloys in current production. A thorough review of the processes involved in AM, specifically LPBF, including the influence of the various mechanisms involved, is reported. Discussions about previous studies on the selected LPBF-produced, β-titanium alloys are included. Finally, the heat treatment response and mechanical performance of the said alloys are reviewed.

Chapter 3 includes the design of the experiment in which the planning and statistical methods of the research are described.

Chapter 4 describes the experimental methodology followed to achieve the objectives of the project. The methodology includes the analysis techniques employed to examine the powder, density, and pores of the samples. Additionally, the sample preparation and process description of the mechanical testing used to determine the hardness and tensile properties are included in this chapter.

Chapter 5 reports the results obtained from the design of the experiment, specifically the design matrix determined and the model developed from the porosity data collected. This chapter also includes the results obtained from the microstructural analysis and mechanical testing conducted, as well as the powder characterisation techniques used.

Chapter 6 discusses the results in detail, including the relationships and analyses of these, as well as the links found between this study and the literature.

Chapter 7 summarises the findings. Recommendations are made for improvements to the methods used and suggest a direction for future study that would further benefit the research field.

2. LITERATURE REVIEW

The outcome of this chapter seeks to establish a foundation of appropriate knowledge to assist in meeting the objectives of this research. Therefore, the fundamentals of titanium's crystal structure and microstructure are explored. Additionally, AM, specifically LPBF, is investigated in which the process, build parameters, scan strategy, and build attributes are considered. Furthermore, the literature on the mechanical performance and printability of LPBF-produced Ti-6-4, Beta 21S, and Ti-5-5-5-3 is studied. The mechanical properties of these LPBF-produced alloys is compared with that of the wrought counterparts.

2.1 Titanium Crystal Structure Fundamentals

Titanium can exist as pure or alloyed in two crystallographic allotropes, either a hexagonal-close-packed (HCP) or body-centerd-cubic (BCC) crystal structure, known as α- and β-phase, respectively. The appearances of said crystal structures can be seen in Figure 1.
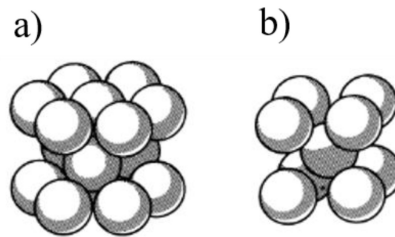
Figure 1: A schematic of the a) hexagonal-close-packed and b) body-centerd-cubic crystal structures (Donachie, 2010)

The α-phase exists naturally in unalloyed titanium but the growth of β-phase can be facilitated upon heating to a particular temperature known as the β-transus temperature. In pure titanium, this temperature is approximately 882.5 °C (Donachie, 2010). However, this transus temperature can be elevated or lowered with the addition of certain elements. Elements responsible for elevating the transus temperature are known as α-stabilising elements, whereas those responsible for lowering the transus temperature are known as β-stabilising elements. Examples of α-stabilising elements are aluminium, oxygen and nitrogen. Molybdenum, iron, vanadium, chromium, and manganese are examples of β-stabilising elements (Donachie, 2010).

The α- and β-phase can exist simultaneously. Their respective quantities in relation to one another are responsible for multiple variations of material properties. Alloys in which the microstructure is dominated by α-phase will exhibit a higher creep strength,

lower density, lower strain rate sensitivity, and improved weldability. With the introduction of β-phase into the microstructure, the titanium alloy will respond better to heat treatment, demonstrate improved fabricability, and higher short-time strength. However, these properties come at the expense of the aforementioned properties presented by the α-phase (Donachie, 2010). As such, the mechanical properties can be tailored by altering the ratio of α- to β-phase to fulfil an intended purpose.

Furthermore, these crystal structures can exist in three microstructure alterations, viz. lamellar, equiaxed, and bimodal. The lamellar microstructure consists of fine, alternating layers of α- and β-phase. Equiaxed structures, on the other hand, have approximately equal dimensions in all directions. Bimodal microstructures include a combination of both lamellar and equiaxed structures. Additionally, these microstructure alterations can exist in either fine or coarse grains, which refers to small or large grain sizes, respectively (Callister & Rethwisch, 2011).

Apart from the crystal structures α and β, these alterations and their grain sizes have an additional influence of the mechanical properties exhibited. Their corresponding influences on selected mechanical properties can be seen in Table 1.

Table 1: The Influence of Microstructure on Selected Mechanical Properties (Sefer, 2014)

Property	Lamellar	Equiaxed	Fine	Coarse
Young's Modulus	No effect	Positive/Negative (texture)	No effect	No effect
Strength	Negative	Positive	Positive	Negative
Ductility	Negative	Positive	Positive	Negative
Fracture Toughness	Positive	Positive	Positive	Positive
Fracture Crack Initiation	Negative	Positive	Positive	Negative
Fracture Crack Propagation	Positive	Negative	Negative	Positive
Creep Strength	Positive	Negative	Negative	Positive
Super-Plasticity	Negative	Positive	Positive	Negative
Oxidation Rate	Positive	Negative	Positive	Negative

Materials with fine grains are typically harder, stronger, and tougher than those with coarse grains, because the former has a greater total grain boundary area to impede dislocation motion. Hence, the behavior seen in Table 1. However, coarse grains offer considerably better creep strength at lower temperatures (Coble creep), because requisite creep diffusion at low temperatures occurs along grain boundaries more so than through bulk grains. Therefore, coarse grains – which have less total grain boundary area than fine grains – offer fewer pathways for such diffusion mechanisms.

Moreover, it can be seen from Table 1 that the lamellar microstructure presents excellent fracture toughness, creep strength, and fatigue crack growth properties. The high fracture toughness associated with the lamellar microstructure is attributed to the ability to deflect cracks propagating along the differently-orientated lamellar packets. The equiaxed microstructure, on the other hand, offers high fatigue resistance and ductility, because this microstructure allows for much deformation in all directions due to its shape. A bimodal microstructure is often employed, because it combines the advantages presented by both lamellar and equiaxed microstructures and, thus, exhibits well-balanced properties (Sefer, 2014).

2.2 Microstructure of β-Titanium Alloys

Upon investigating the crystal structure of titanium and what differentiates the α and β structures, the microstructure is now considered and how the alloys are categorized accordingly. This is important to note for the reason that the microstructure dictates the overall behavior of the alloy. However, the definition of titanium β alloys has been difficult to describe due to the continuum of β-phase stabilisation and the subjectivity with which the distinction between α+β and β alloys has been established (Cotton et al., 2015). β-stabilised chemistries have been separated into categories detailing the types according to increasing β-stability. These categories are termed α-matrix α+β → β-matrix α+β → unstable (metastable) β → practically stable β → stable β (Cotton et al., 2015).

Metastable β alloys are defined according to Cotton et al. (2015) as alloys in which the β-phase is present upon quenching, but decomposes to α and stable β on annealing or working in the α+β field. Practically stable β occurs when the alloy is sufficiently β but transforms once heated to an adequate temperature in service. Titanium alloys are established as stable β alloys whereby the β-transus temperature lies below room temperature or if the β-phase is retained upon quenching.

However, there are limitations to the definition of a stable β alloy: nearly all commercial alloys are metastable, metastable athermal ω-phase is formed during quenching, and the kinetics of β-phase decomposition are not considered during quenching. Therefore, to provide clarity, the Molybdenum-Equivalent (Mo-Eq) equation, reported in wt. %, was defined, as seen by Equation 1.

$$\begin{aligned}
Mo - Eq = {}& 1.0(wt.\% \, Mo) + 0.67(wt.\% \, V) + 0.44(wt.\% \, W) \\
& + 0.28(wt.\% \, Nb) + 0.22(wt.\% \, Ta) \\
& + 2.9(wt.\% \, Fe) + 1.6(wt.\% \, Cr) + 1.25(wt.\% \, Ni) \\
& + 1.7(wt.\% \, Mn) + 1.7(wt.\% \, Co) - 1.0(wt.\% \, Al)
\end{aligned} \tag{1}$$

The Mo-Eq equation is used to characterize the β-phase stability, and is a combined quantity of the effects of the β-phase stabilising, α-phase stabilising, and neutral elements on the β-phase stability in a titanium alloy. Molybdenum is chosen as an arbitrary baseline whereby other elements are normalized to an equivalent Mo value. The higher the Mo-Eq value of a given titanium alloy, the more likely the alloy is able to retain close to 100% volume of β-phase upon quenching from the single β-phase field to room temperature (Kolli & Devaraj, 2018). This can be seen graphically from the schematic seen in Figure 2.
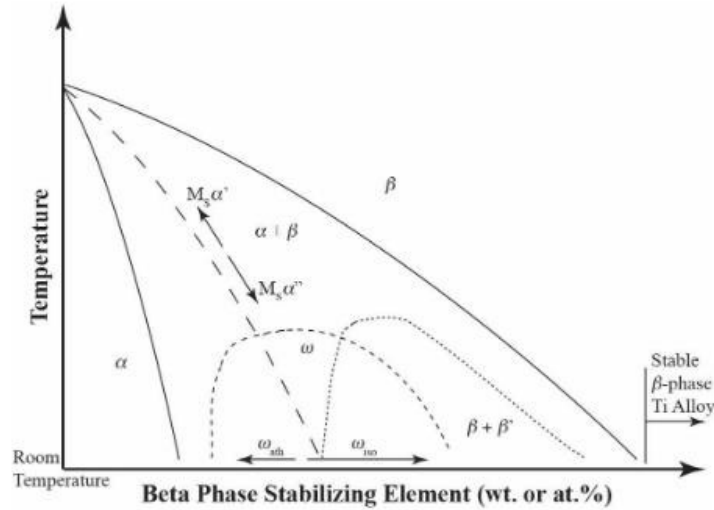
Figure 2: A schematic of the pseudo-binary isomorphous phase diagram (Kolli & Devaraj, 2018)

Furthermore, from Figure 2, it can be seen that to suppress the formation of α'-martensite ($M_s\alpha'$) phase, orthorhombic α"-martensite ($M_s\alpha''$) phase, and equilibrium HCP α-phase, β-stabilising elements are alloyed in sufficient quantities (Kolli & Devaraj, 2018). The aforementioned phases are characteristically brittle, thus unfavorable.

2.3 Chemistry of β-Titanium Alloys in Current Production

As mentioned in the first chapter of this study, there are six commercially available β-titanium alloys in current production, viz. Ti-10-2-3, Beta C, Ti-15-3-3-3, Beta 21S, Ti-5-5-5-3, and Alloy C.

Among the six alloys, common characteristics are shared, including chemical composition. All contain aluminium – apart from Alloy C – because of the beneficial attributes it offers. Being the principle substitutional α-stabiliser, it provides solid-

solution strengthening. Additionally, this element is alloyed to reduce density and formulation costs.

Vanadium and molybdenum are isomorphous β-stabilisers, being cost-effective alloying elements with a low tendency to segregate upon solidification. However, vanadium has limited oxidation resistance in elevated-temperature applications, which is why it is not found in Beta 21S, an alloy used in such services.

Iron and chromium, eutectoid β-stabilisers, are the most cost-effective constituents and the most efficient in terms of solid-solution strengthening, making them the β-stabilisers of choice. Despite iron being an effective β-stabiliser, it is a rapid diffuser, making it an unfavorable alloying element in applications prone to creep.

The β-transus temperature is affected by the aforementioned alloying elements, either in raising or lowering it as previously discussed. The Mo-Eq, taking into account the contribution of these alloys, can be used to estimate the β-transus temperature. As such, the Mo-Eq and corresponding β-transus temperatures can be seen in Table 2.

Table 2: Commercial Titanium β alloys in Current Production with Corresponding Mo-Eq and β-Transus Temperatures Adapted from Cotton et al. (2015)

Alloy	Mo-Eq (wt. %)	β-Transus Temperature (ºC)
Ti-10-2-3	9.5	790 – 805
Ti-5-5-5-3	9.6	820 – 880
Ti-15-3-3-3	11.9	750 – 770
Beta 21S	12.8	795 – 810
Beta C	16	715 – 740
Alloy C	47.5	NA*

*Stable below β-transus temperature

2.4 Additive Manufacturing: Laser Powder Bed Fusion

After reviewing the materials in question, the production process is considered. This section covers the LPBF process by which parts are produced, as well as the build parameters, attributes, and scan strategies that influence the quality and behavior of produced parts. LPBF has been used extensively to produce Ti-6-4 components and, consequently, there is a substantial amount of literature. Therefore, a review of Ti-6-4 is included in this section to provide insight into potential similarities found in Beta 21S and Ti-5-5-5-3 and to assist in the design of the experiment discussed in the subsequent chapter.

2.4.1 Process

The LPBF process begins with a thin layer of metal powder, typically between 20 and 60 μm thick, fed from a feed container and deposited over a base plate or a previously fused layer of powder by means of a powder scraper. The process, as seen in Figure 3, is followed by laser melting, which utilizes a high-intensity laser beam to densify the powder material. The build platform is then lowered by the intended layer thickness to accommodate the next layer of powder. The powder layering and laser melting processes are repeated continuously until the part has been completed. The cross section of the intended part geometry is generated with a computer-aided design (CAD) file, which is commonly saved in stereolithographic (STL) file format.
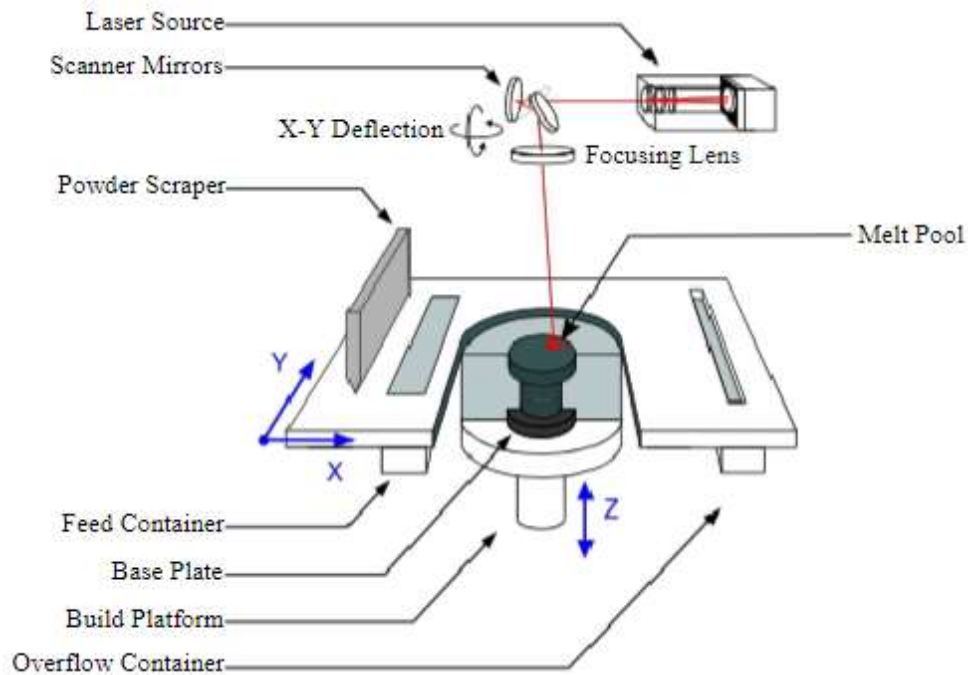
Figure 3: The typical layout of the LPBF Process (Craeghs et al., 2011)

The aforementioned process is performed in a closed chamber within an inert environment and under overpressure conditions to prevent oxygen contamination and to control the vaporization of powders. The inert atmosphere is achieved using gases such as argon and nitrogen, depending on the reactivity of the metal.

2.4.2 Build Parameters

The process parameters involved in fabricating materials using LPBF vary among metals and their alloys, because these parameters depend on the way in which the physical and chemical properties interact with the laser. Careful consideration of these parameters is required due to the adverse effects which may result. Such effects include

porosity, cracks and an altered chemical composition due to selective vaporization, occuring when the vaporization temperature of one or more metal constituents has been exceeded. Not only do the process parameters need to be optimized to produce functional parts, but also to reduce energy expenditure and production time to satisfy market demands and increase profitability.

Most research conducted on process optimization investigates volumetric energy density (*VED*) or energy input (*E*), which is defined by Equation 2:

$$VED \ or \ E = \frac{P}{v \cdot h \cdot t} \tag{2}$$

VED (J/mm^2) is a function of *P*, the effective laser power (W), *v*, the laser scan speed (mm/s), *h*, the hatch spacing (mm), and *t*, the layer thickness (mm) of the powder bed. These parameters can all be adjusted to vary *VED*. Although Equation 2 is a measure of the energy supplied to the process, it does not take into consideration other factors, such as scan strategy, composition of the metal, atmosphere used, and powder-bed temperature.

Dilip et al. (2017) conducted a study, investigating the influence of LPBF process parameters on the melt pool geometry, porosity, and microstructure of Ti-6-4. This was done by analyzing single-track deposits and bulk samples, whereby experiments utilizing multiple combinations of scan speed and laser power were performed. The laser power ranged from 50 to 195 W, while the range of scan speed was 500 – 1200 mm/s.

At the lower limits of laser power and scan speed, a continuous and uniform weld bead was achieved. However, when keeping the laser power constant and increasing the scan speed, it was discovered that the deposits became discontinuous and inconsistent, eventually, resulting in balling – the fragmentation of track deposits. Bulk parts fabricated using low laser power and high scan speed may result in porosity due to the low *VED* from said combination.

When maintaining a constant scan speed, increasing the laser power causes an increase in the width of the melt pool due to the higher intensity of the laser beam. However, the balling phenomenon did not occur at the higher power settings.

It was concluded that scan speed and laser power have a significant effect on the melt pool geometry, whereby the bead width would decrease as the scan speed increases for all power settings. Much like the decrease in scan speed, an increase in the laser power settings would result in an increase in the bead width due to the increase in *VED*.

VED was proven to be directly proportional to the depth of penetration. Therefore, at low scan speeds and high laser power, the energy density would increase according to Equation 2 and cause an increase in the depth of the single-track melt pool. The converse is also true. The melt pool geometry can be seen in Figure 4.
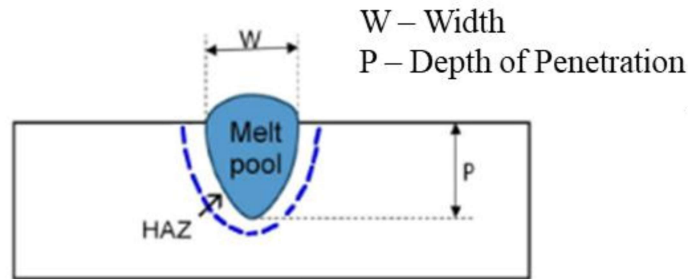
Figure 4: Schematic of the melt pool geometry (Dilip et al., 2017)

Upon examining the porosity in the bulk parts, a direct correlation between the porosity evolution and the applied *VED* was observed. However, the closer to the upper and lower limit of the range of the applied *VED*, the more porosity was found in the bulk parts, but for different reasons. Insufficient melting of powder particles was caused by a low *VED*, while a high *VED* resulted in the keyhole effect. The keyhole effect occurs when metal constituents vaporize, forming bubbles of gas which get trapped below the surface of the melt pool. This results in the formation of spherical pores (Dilip et al., 2017).

2.4.3   Scan Strategy

In addition to the build parameters mentioned previously, the scan strategy influences the density of a component. It also has a strong influence on the meso- and microstructures, which commonly result in the anisotropy of properties demonstrated by LPBF-produced metals. This can be attributed to either the presence of high porosity or columnar prior-β grain structures, both of which can be amended using the appropriate scan strategy. The β-grain grows along the deposition direction but is limited to growth in the perpendicular direction due to the thin layer of α-phase that forms along the β-grain boundary, which serves as a path along which damage can preferentially occur and accumulate.

Therefore, to curb the anisotropy in the properties found, a study was carried out by Kumar, Prakash, and Ramamurty (2018), in which Ti-6-4 samples with four different combinations of layer thickness and scan rotation were produced using LPBF. The combinations included two variations of layer thickness, viz. 30 and 60 μm, paired with two different scan rotations, being 90 and 67°. The four combinations can be seen in Table 3 along with the accompanying scan speed, laser power, hatch spacing, and *VED*.

14

The combinations are labelled; the 3D representation of the microstructure of each combination can be seen in along with the accompanying scan speed, laser power, hatch spacing, and *VED*. The combinations are labelled; the 3D representation of the microstructure of each combination can be seen in Figure 5 with reference to the table here mentioned.

Table 3: Different Combinations of Process Parameters Studied by Kumar, Prakash, and Ramamurty (2018) to Assess the Meso- and Microstructures of LPBF-Produced Ti-6-4

Label	Laser Power [W]	Scan Speed [mm/s]	Hatch Spacing [mm]	Layer Thickness [μm]	Scan Rotation [°]	VED [J/mm³]
a)	280	1200	0.14	30	90	55.6
b)	280	1200	0.14	30	67	55.6
c)	340	1250	0.12	60	90	37.8
d)	340	1250	0.12	60	67	37.8
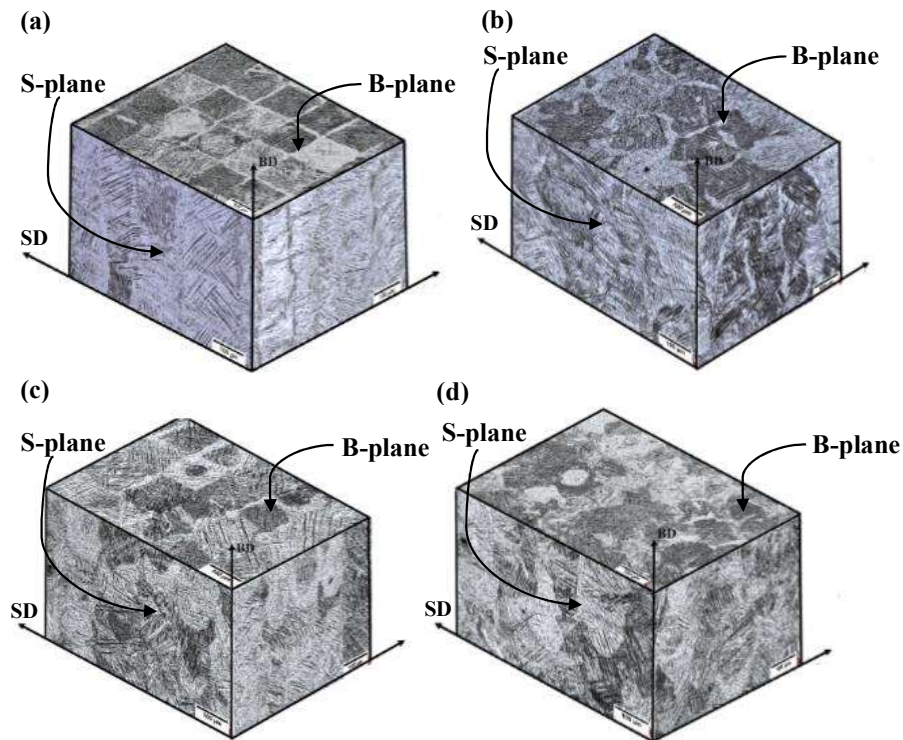
Figure 5: 3D representations of the microstructure of Ti-6-4 samples with a) 30 μm layer thickness and 90° scan rotation, b) 30 μm layer thickness and 67° scan rotation, c) 60 μm layer thickness and 90° scan rotation, and d) 60 μm layer thickness and 67° scan rotation (Kumar, Prakash, and Ramamurty, 2018).

The yield strength, σ_Y, ultimate tensile strength, σ_T, and the elongation to failure, e_f – among other mechanical properties – were reported by Kumar, Prakash, and Ramamurty (2018). Measurements for each property were taken in the S- and B-directions, being the transverse and build directions, respectively, as seen in Figure 5. The properties mentioned are noted in Table 4 for each combination of layer thickness and scan rotation used.

Table 4: Mechanical Properties of Ti-6-4 Produced using Different Combinations of Layer Thickness and Scan Rotation (Kumar, Prakash, & Ramamurty, 2018)

Sample Code	Direction	Sample Layer Thickness [μm]	Scan Rotation	σ_Y [MPa]	σ_T [MPa]	e_f [%]
B3090	B	30	90	1161 ± 30	1237 ± 30	7.6 ± 1
S3090	S	30	90	1029 ± 8	1091 ± 6	7.8 ± 0.8
B3067	B	30	67	1121 ± 42	1186 ± 42	8.1 ± 0.6
S3067	S	30	67	1121 ± 9	1202 ± 11	10.1 ± 0.3
B6090	B	60	90	1151 ± 11	1222 ± 25	9.8 ± 1.1
S6090	S	60	90	1115 ± 18	1183 ± 22	9.7 ± 0.3
B6067	B	60	67	1102 ± 16	1145 ± 14	12.5 ± 1.4
S6067	S	60	67	1063 ± 17	1137 ± 23	12.8 ± 0.9

The reported range of σ_Y and σ_T are significantly higher than what is typically reported for wrought Ti-6-4, being approximately $850 - 900$ MPa and $950 - 1000$ MPa, respectively. This is ultimately due to the finer microstructural features found, which lead to higher σ_T.

However, when considering the fractographs obtained on the tensile tested samples of B3090 and S6067, which demonstrated the lowest and highest combinations of σ_Y and e_f, respectively, the former indicated that failure occurred along the columnar prior-β boundaries. This is because the tensile load was applied normal to the columnar prior-β grains. Sample S6067, on the other hand, demonstrated a corrugated fracture surface, possibly due to the equiaxed nature of the prior-β grains in the S plane. Consequently, Kumar, Prakash, and Ramamurty (2018) suggest that the presence of these columnar prior-β grains may be marginally detrimental to the tensile behavior of LPBF-produced Ti-6-4, because of the anisotropy found in σ_Y and e_f. This can be further substantiated by the fact that the properties of 6067 show marginal anisotropy and high ductility when compared to the properties of other samples, because the columnar prior-β grains are completely equiaxed.

Regarding the anisotropy of the properties presented by 6090, it is interesting to note that the difference in σ_Y in the B and S planes is approximately only 3%. Kumar, Prakash, and Ramamurty (2018) suggest that this is likely because the melt zone boundaries do not overlap, resulting in the epitaxy being broken up. Concerning 3067, properties present no anisotropy with relatively high σ_Y, being only 3.4% lower than that of B3090, which displays the highest σ_Y.

The ductility of all measured samples complies with the minimum ductility condition of 5%, which is generally mandated by the aerospace industry (Kumar, Prakash, & Ramamurty, 2018).

With regards to the porosity of the samples in this study, it is reported to be substantially smaller than the levels reported by Cain et al. (2015), which utilized a scan rotation of 90°. However, this discrepancy may be the result of the variation of process parameters used between both studies. It is clear that the presence of columnar prior-β grains can be circumvented by the addition of an appropriate scan strategy, resulting in relatively isotropic properties. Any discrepancies in the properties found along different planes may be likened to porosity. Therefore, further investigation into the optimization of LPBF process parameters is essential to investigate the effect of porosity on the anisotropy of LPBF-produced parts.

2.4.4 AM Build Attributes

Several attributes result from the processes involved in AM. Of particular interest are those which affect the performance of materials. One issue is the inherent anisotropy brought on by the growth of columnar prior-β grains previously mentioned. Another detrimental feature is residual stress. The temperature gradient mechanism is commonly cited as the cause of this. The feedstock material is heated rapidly due to the high *VED*, causing the material to expand. The expansion is, however, prohibited by the surrounding material, thus resulting in a compressive stress state in the heated zone. When the heat source is removed, the melted material cools down and shrinkage tends to occur, which imparts a tensile stress state on the subsequent layer. This stress state is restrained by the plastic strain formed during the heating stage (Li et al., 2018). The tensile residual stress thus leads to distortion and/or crack formation. Therefore, reducing the temperature gradient is imperative to minimize the residual stresses. One such method is to pre-heat the base plate and maintain its temperature throughout the LPBF process.

Another internal defect brought on by LPBF is porosity formation. Four types of pores are described by Sola and Nouri (2019), which can be seen in Figure 6.
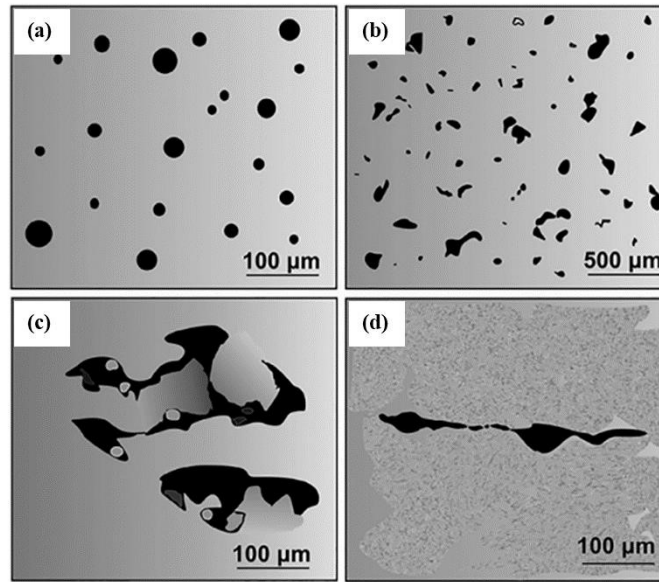
Figure 6: Characteristic pores induced during the LPBF process: (a) entrapped gas porosity, (b) incomplete melting-induced porosity, (c) lack-of-fusion with unmelted particles inside large irregular pores and (d) cracks (Sola & Nouri, 2019)

Defect formation is influenced by three main factors, viz. equipment-related, powder-related, and process-related factors. Regarding equipment-related defect formation, optical system alignment, quality and cleanness of mirrors, control of the beam deflection mechanisms, and calibration of beam energy profile influences the quality of the finished part. In addition, inadequate flow of the inert gas in the build chamber is likely to cause pore formation whereby metal feedstock is vaporized with high *VED* and then condensed in the relatively cold atmosphere, causing potential interference with the laser beam. Therefore, this prevents the correct transmission of power to the powder bed. Oxidation contamination is also a possibility despite the inert atmosphere created in the build chamber. This could aid in the formation of balling and cause poor bonding between layers.

Powder-related defect formation occurs due to poor feeding efficiency as a result of inadequate powder flowability, which is caused by irregularly shaped powder particles. As such, spherical particles with a controlled particle-size distribution are essential to ensure the consistent layer formation of feedstock material. However, pores within the particles may be transferred to the as-built parts because of inert gas trapped during the powder production process. This trapped gas causes the pores to grow at elevated temperatures. In addition to this, surface-absorbed moisture is potentially a source of hydrogen-related defects. Therefore, to effectively reduce the risk of porosity due to

18

the moisture content, it is necessary to dry the feedstock material. Employing baseplate heating may further reduce this risk.

Finally, and of particular importance to this study, is process-related defect formation. Lack-of-fusion – a consequence of low power-to-speed ratios – causes the incomplete junction of subsequent layers and adjacent melt pools. As a result, the powder bed becomes increasingly uneven, causing cavities filled with loose powder or inadequately melted particles. Conversely, if the power-to-speed ratio is too high, high *VED* causes the vaporization of one or more metal constituents, resulting in large pores due to the previously-discussed keyhole effect. A relatively large hatch spacing causes insufficient overlap between adjacent tracks, resulting in characteristic pores arranged in straight lines. Reducing the hatch spacing thus decreases the likelihood of defects. Layer thickness is another important parameter considered to ensure part quality. Overheating may occur if the layers are too thin, whereas interlayer bonding is unsuccessful if the layers are too thick (Sola & Nouri, 2019).

2.5 Review of AM-Produced Titanium Alloys

This section reviews the alloys in question with reference to literature in the AM context.

2.5.1 Review of AM-Produced Ti-6-4

Ti-6-4 is an α+β alloy and has largely been the focus of recent studies investigating AM capabilities and properties. The popularity of this alloy arises from its favorable mechanical properties, including its high strength, low density, high fracture toughness, excellent corrosion resistance, and superior biocompatibility, making it suitable for a variety of industries.

Ti-6-4 was developed in the 1950s for the aerospace industry, which currently dominates its demand. However, other industries, such as marine, automobile, energy, chemical, and biomedical industries, find use for this versatile alloy (Donachie, 2010).

The industries in which Ti-6-4 finds itself often require complex components to be manufactured to fulfill the intended function. As such, AM has been a noteworthy adversary for traditional manufacturing methods to achieve said complex geometries, along with many other benefits as previously discussed.

However, this does not come without limitations. Porosity, unfavorable microstructure, and residual stress are among some of the limitations found. These affect the macroscopic behavior of the alloy and, therefore, post-manufacturing processes, such as heat treatment and hot isostatic pressing (HIP), are often employed to alleviate these performance inhibitors. However, applying HIP post manufacture results in the loss of

shape accuracy, while the heat treatment thereof may not result in a uniform microstructure due to the shape irregularities (Liu and Shin, 2019).

For this reason, Liu and Shin (2019) conducted a study in which the analysis of the porosity, microstructural evolution, and residual stresses, along with the accompanying properties, of as-built samples are considered. The processes considered for analysis are Directed Energy Deposition (DED), LPBF and Electron Beam Melting (EBM).

The recorded porosity and residual stresses found in as-built Ti-6-4 can be seen in Table 5. LPBF produces the highest residual stresses. As such, post-manufacturing heat treatment by means of stress-relief annealing is essential to alleviate these stresses to improve part performance. Stress relief treatments typically used on Ti-6-4 operate within a temperature range of 480 – 650 °C for 1 – 4 hours, according to Donachie (2010).

Liu and Shin (2019) also reported that Ti-6-4 experiences α + β → β → liquid → β → α + β/α' transformation in the complete melting and solidification case.

Table 5: Reported Porosity and Residual Stress Found in DED-, LPBF-, and EBM-produced Ti-6-4 (Liu and Shin, 2019)

AM Process	Porosity (vol. %)	Residual Stress, σ (MPa)
DED	0.01 – 0.27	-
LPBF	0.1 – 0.5	100 – 500
EBM	0.1 – 0.3	Very low

Porosity is largely the result of an inadequate melt pool geometry, which depends on the process parameters and the consequent *VED*. A study conducted by Promoppatum, Onler, and Yao (2017) defines measurable criterion upon which to assess the validity of the melt pool geometry in Ti-6-4.

Determining the likelihood of lack-of-fusion is done by analyzing the melt pool depth. To ensure adequate penetration into subsequent layers, Promoppatum, Onler, and Yao (2017) suggest the width of the melt pool at the depth of the subsequent layer be at least the laser diameter, as seen in Figure 7. This ensures sufficient coverage by the melt pool.

Fully covered the powder layer　　　**Partially covered the powder layer**

a)　Laser Diameter

Powder Layer

Layer Thickness

b)　Laser Diameter

Powder Layer

Layer Thickness

Insufficient Penetration
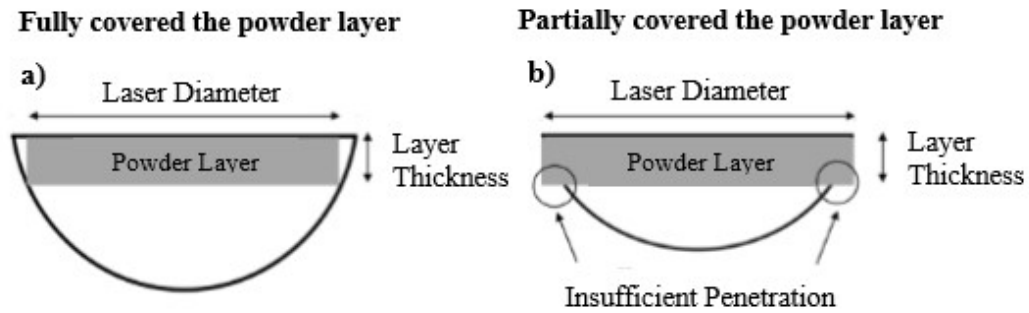
Figure 7: A graphical representation of the effect of melt pool depth: a) the powder layer is fully covered by the melt pool, resulting in the unlikely occurrence of lack-of-fusion, whereas b) the powder layer is insufficiently covered by the melt pool, likely causing lack-of-fusion (Promoppatum, Onler, & Yao, 2017).

Based on the information found, Promoppatum, Onler, and Yao (2017) define a comprehensive processing window with validated criteria for Ti-6-4. In the window seen in Figure 8, the undesirable regions are shaded grey and indicate areas in which over melting, the balling effect, and incomplete melting are likely to occur. Incomplete melting is to be expected at a *VED* of less than 36.9 J/mm^3 and when scan speeds of less than 333 mm/s are achieved. The criterion set out for the scan speed was determined using Equation 3, where r_0 is the laser radius – being 50 μm in this case – k_s is the thermal conductivity of the solid, l is the layer thickness – being 30 μm for this study – ρ_s is the density of the solid, and C_p is the specific heat.

$$v > \frac{2r_0k_s}{l^2\rho_sC_p} \tag{3}$$

Equation 3 is a function of heat propagation time – the time required for heat to travel through a layer of powder – and total heating time – the time taken for the laser to travel a distance equal to the laser diameter.

21
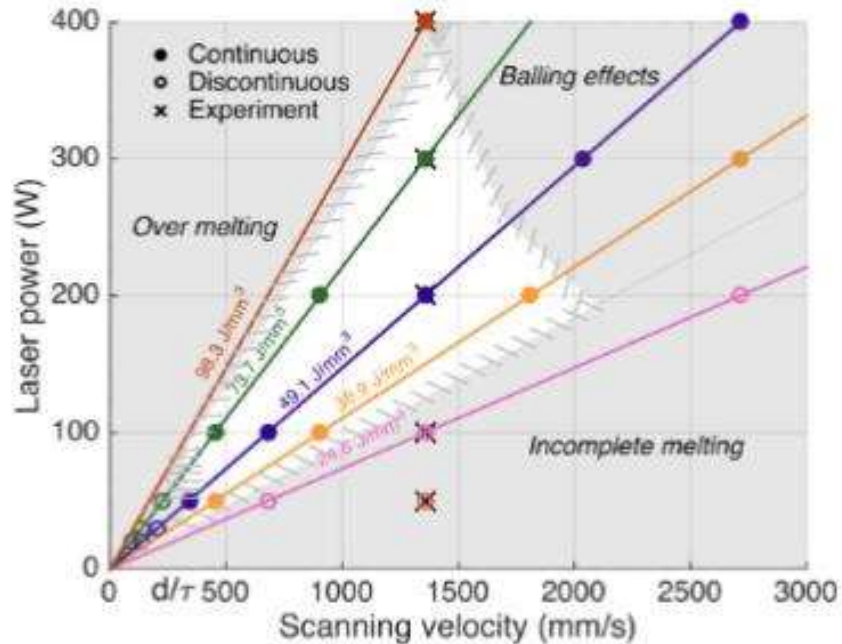
Figure 8: The processing window for Ti-6-4 produced using Direct Metal Laser Sintering (DMLS) (Promoppatum, Onler, & Yao, 2017)

The processing window in Figure 8 also demonstrates the likely occurrence of the balling effect in which molten metal tends to spheroidize to minimize the surface area, much like the formation of a mercury ball. This is caused because of high surface tension and low wettability of molten metal and leads to poor part performance due to substantial porosity and inadequate bonding between layers.

Yadroitsev et al. (2010) note a criterion for this effect based on the length and width of the melt pool geometry whereby the length-to-width ratio is not to exceed π according to the Plateau-Rayleigh analysis of the capillary instability of cylindrically-shaped liquid. The balling effect is expected to occur should this criterion not be met. The corresponding process parameters needed to cause this – as analyzed by Promoppatum, Onler, and Yao (2017) – are depicted and outlined according to the processing window in Figure 8.

The last of the undesirable regions – over melting – outlines parameters in which the input energy is significantly high, causing the keyhole effect. This results in high porosity and occurs at *VED* values higher than approximately 87 J/mm^3 (Gong et al., 2015).

Regarding the microstructure of the samples, it was found that all cases within the continuous melting region of the processing window revealed columnar grains.

22

Furthermore, all samples under energy densities of 49.1 and 73.7 J/mm^3 exhibited approximately the same microstructure in which, according to the side surfaces seen in Figure 9 a) and c), the prior-β grain demonstrates columnar growth along the build direction with fine acicular martensite. From Figure 9 b) and d), the grain growth, as seen on the top surfaces, follows the scanning direction, which is unidirectional for every layer according to Promoppatum, Onler, and Yao (2017). It was concluded that the columnar grains are likely to occur regardless of the laser power and scan speed, resulting in strong anisotropic properties. Ti-6-4 samples printed in the vertical direction typically have 20 – 30 MPa lower σ_T and σ_Y than those printed in the horizontal direction. However, the elongation increases by approximately 2% in the vertical direction.
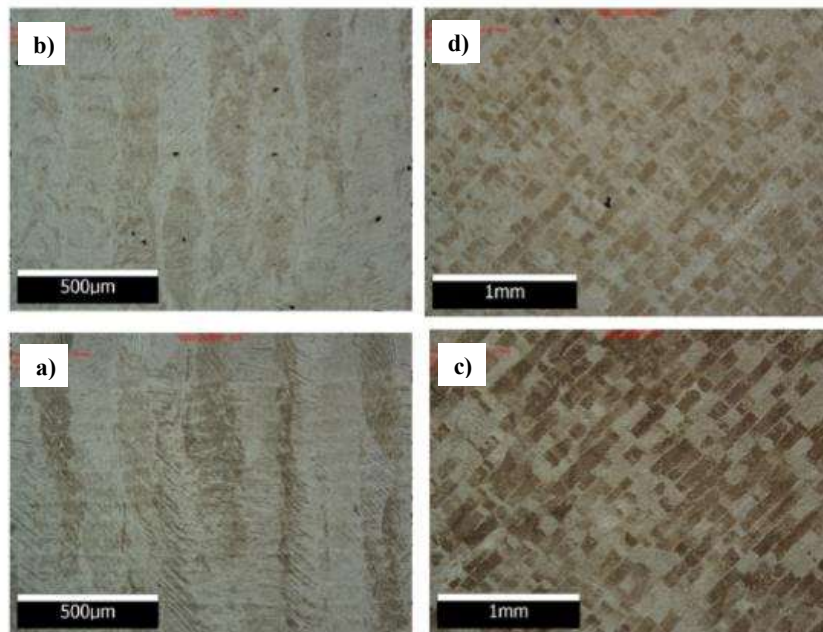
Figure 9: Microstructures of top and side surfaces of Ti-6-4 DMLS samples: a) side surface – energy density of 49.1 J/mm^3, b) top surface – energy density 49.1 J/mm^3, c) side surface – energy density of 73.7 J/mm^3, d) top surface – energy density 73.7 J/mm^3 (Promoppatum, Onler, & Yao, 2017).

2.5.2   Ti-5-5-5-3 Printability and Microstructural Evolution

After assessing the effect of various process parameters on AM-produced Ti-6-4, it is important to consider the alloys in question and how they compare with the results found. Bakhshivash et al. (2019) conducted a study in which the printability and microstructural evolution of Ti-5-5-5-3 were investigated. The *VED* values were varied. After which, an analysis of the corresponding microstructural evolution was performed to provide a thorough understanding into the optimization of the

microstructure and density of Ti-5-5-5-3, while maintaining a relatively precise geometry.

The printability was investigated by producing 27 cylindrical samples – with the geometric dimensions as seen in Figure 10 – using a *Renishaw* AM400 machine.
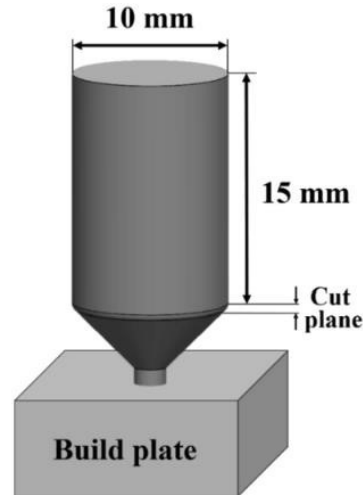
Figure 10: A schematic of Ti-5-5-5-3 sample print dimensions (Bakhshivash et al., 2019)

The *VED* values were varied from 21 J/mm^3 to 584 J/mm^3. Furthermore, the scanning speed and laser power settings were selected to satisfy the industrial requirements in terms of the production rate. The hatch spacing and layer thickness were kept constant at 95 and 45 μm, respectively. The scanning strategy used was a chessboard pattern and kept constant to negate the effects thereof.

Archimedes' density tests and μ-CT scans were performed to determine the relative densities of each sample. The highest relative densities obtained were for *VED* values between 50 and 175 J/mm^3, as seen in Figure 11. The drop in relative density beyond this range can be attributed to the heat input. The lower and higher *VED* values responsible for the drop in relative density are the result of insufficient and excess heat input, respectively.

24
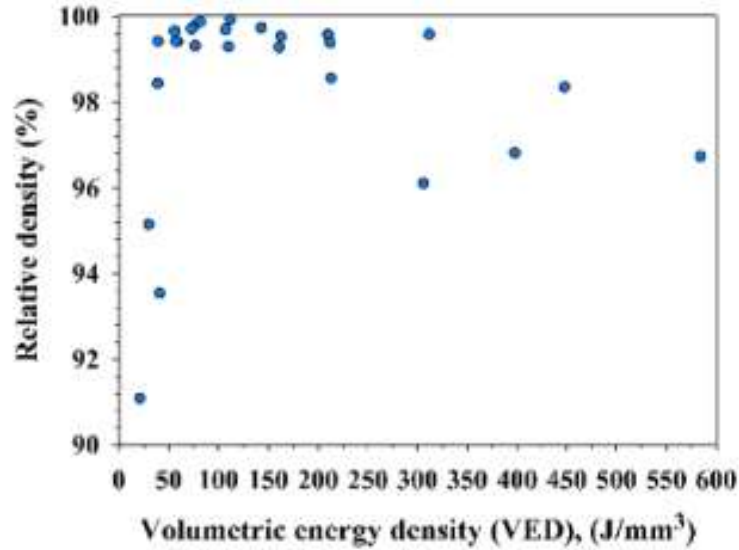
Figure 11: The effect of VED on the relative density of Ti-5-5-5-3 (Bakhshivash et al., 2019)

As seen in Figure 11, there are three regions of low, medium, and high *VED* values, which were responsible for the low, high, and medium relative densities obtained, respectively. When considering the porosity associated with these regions, one can see from Figure 12 that the pores observed for low *VED* values are irregularly shaped and relatively large. This is, according to Bakhshivash et al. (2019), the result of poor inter/intra-overlapping between melt pools and weak bonding between melted layers due to insufficient applied energy, i.e., lack-of-fusion. This is in accordance with the behavior noted for Ti-6-4.
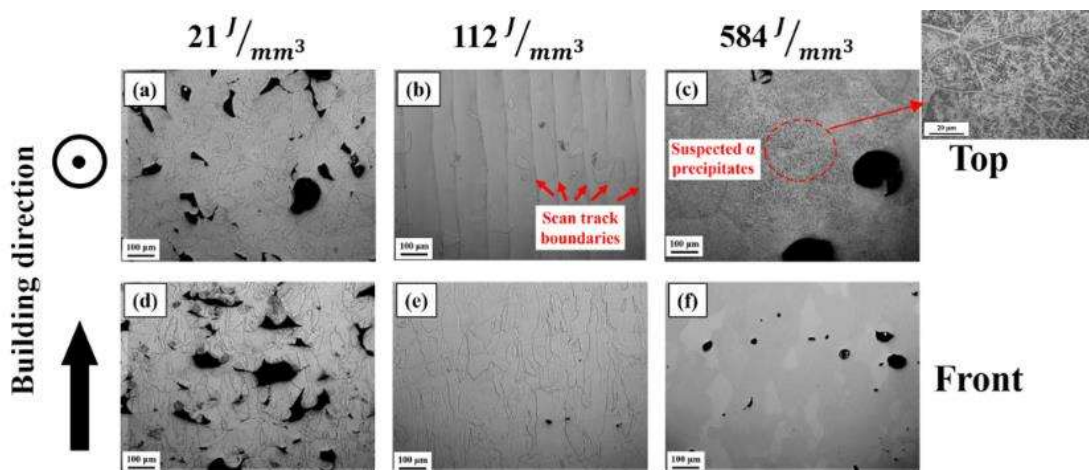
Figure 12: Optical micrograph images of selected samples printed at a) and d) low, b) and e) medium, and c) and f) high VED values (Bakhshivash et al., 2019)

25

The internal pores associated with the high *VED* values, on the other hand, appear to maintain a spherical shape. As discussed in the previous section, these pores may be the result of the keyhole effect.

From Figure 12 b), the grain growth attributed to the application of medium *VED* is epitaxial. According to Yan, Xiong, and Faierson (2017), the re-melting of a previously solidified layer induces heterogeneous nucleation at the melt pool boundary and epitaxial grain growth. Therefore, the transverse columnar grain size is determined by the grain size of the substrate layer. Therefore, the resulting growth occurs along their easy growth direction. This concept can be seen in Figure 13.
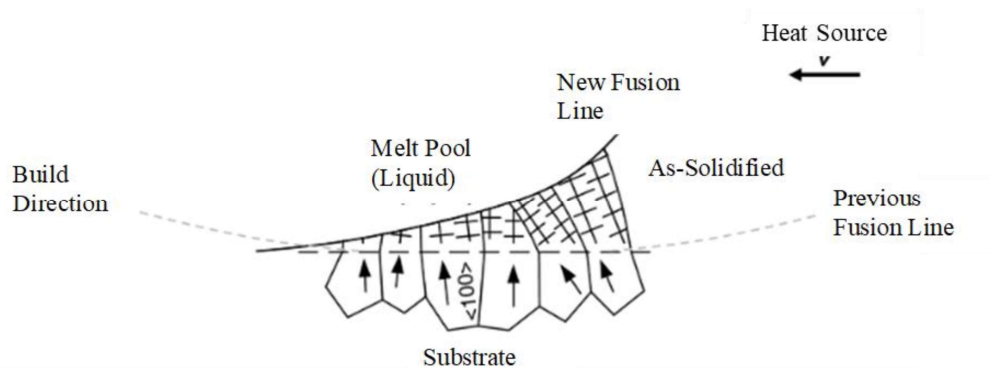
Figure 13: A schematic illustrating the epitaxial grain growth in the easy growth direction indicated by the arrows shown in the grains (e.g. <100> in BCC and FCC metals; <1010> in HCP metals) (Yan, Xiong, & Faierson, 2017)

When examining the microstructures of samples printed at the medium and high *VED* values, Bakhshivash et al. (2019) reported that the latter consisted of β- and fine secondary α-phase, while the former revealed the presence of only β-peaks in the X-ray diffraction (XRD) pattern. This is due to the steep temperature gradient present during the LPBF process.

However, upon further investigation beyond the macro-analysis performed, it was discovered that the sample printed at the medium *VED* value was at the early stage of aging, i.e., $\beta \rightarrow \beta + \omega$, since the $\beta \rightarrow \alpha$ transformation occurs in two steps summarised as $\beta \rightarrow \beta + \omega \rightarrow \beta + \alpha$. The ω-phase, an HCP shape with a short c/a ratio and more equiaxed morphology than the α-phase, nucleates and essentially behaves as nucleation sites for an α-needle matrix. As such, the development and aging of α-phase may occur well after a part has been commissioned.

Yet, when considering the sample printed at the high *VED* value, α-needles are clearly present and absent of ω-particles, suggesting a complete $\beta \rightarrow \beta + \omega \rightarrow \beta + \alpha$

transformation took place where secondary α-needles exist in a matrix of primary β-phase. The bottom layers, having undergone a longer heating period and more reheating and remelting cycles than the layers printed last, consist of wider α-needles suggesting that bottom layers have fully-grown α-needles, while the top layers are in the final stages of the ω → α transformation.

2.5.3   Beta 21S Printability and Microstructural Evolution

Beta 21S, the second titanium β alloy under consideration, was investigated by Pellizzari et al. (2020) to determine its biocompatibility through microstructural, mechanical, and cytotoxicity analyses. Cylindrical samples, much like Figure 10, were printed with a height and diameter of 10 and 4 mm, respectively. Samples were printed using a SISMA SPA machine (*MYSINT100*) with a laser spot diameter of 55 μm. The *VED* ranged 40 – 90 J/mm^3. The scan strategy implemented a 90 °C rotation and the layer thickness was kept constant at 20 μm. Unfortunately, no further information was provided regarding the laser power and scan speed. However, the process parameters were optimized to achieve maximum density.

The microstructure of Beta 21S is of particular interest to this study. The XRD analysis performed by Pellizzari et al. (2020) confirms the presence of a single metastable β-phase where neither α- nor α'-martensite were detected in the as-built condition. The grain growth occurred along the build direction much like Ti-5-5-5-3, shown in Figure 13. A study conducted by Macias-Sifuentes et al. (2021) confirms these findings. The study reports using a Renishaw *AM400* machine and, unfortunately, also shares no information regarding the build parameters used. The columnar grain growth can be seen in the scanning electron microscopy (SEM) analysis performed Figure 14 b).
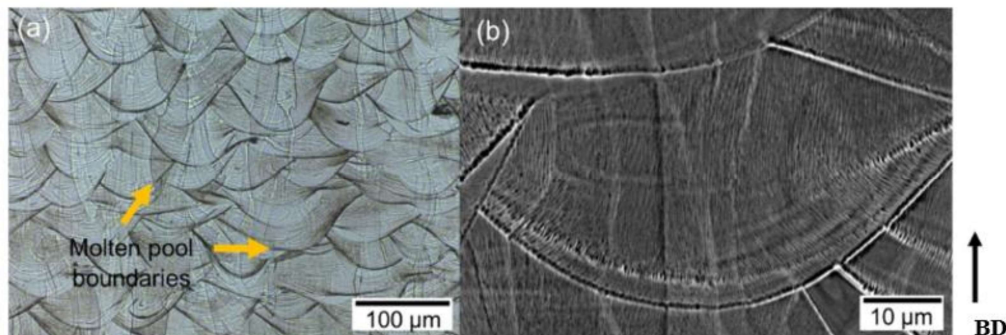
Figure 14: (a) Optimal and (b) SEM micrographs of Beta 21S in the as-built condition (Macias-Sifuentes et al., 2021)

In addition to this, Macias-Sifuentes et al. (2021) report the formation of dendrites. As each layer partially re-melts the previous layer, grain growth from existing grains is facilitated. The heat flux is directed parallel to the build direction. Therefore, the

growth of dendrites is, consequently, seen through epitaxial growth through multiple layers.

2.5.4 Reported Mechanical Properties

Both studies conducted by Zhang et al. (2022) and Macias-Sifuentes et al. (2021) on Ti-5-5-5-3 and Beta 21S, respectively, report hardness findings comparable to that of the wrought counterparts in the solution-treated condition. A summary of this comparison can be seen in Table 6. As previously mentioned, the process parameters used in the study carried out by Macias-Sifuentes et al. (2021) are not stipulated. However, Zhang et al. (2022) do mention that a laser power, scan speed, layer thickness, and hatch spacing of 350 W, 1400 mm/s, 30 μm and 120 μm are used for Ti-5-5-5-3, respectively. Additionally, the properties reported were obtained from samples having undergone baseplate heating at 200 °C. These conditions closely resemble those used in this study.

The solution treatment of T-5-5-5-3 is usually conducted at the β-transus temperature (820 – 880 °C) minus 20 – 60 °C in which it is soaked for one hour and finally air cooled. Beta 21S, on the other hand, is solution treated above the β-transus temperature (795 – 810 °C) between 816 – 899 °C for 3 – 30 minutes (Cotton et al., 2015).

Table 6: Comparison between the Hardness of LPBF-Produced T-5-5-5-3 and Beta 21S and that of Wrought Counterparts in the Solution-Treated Condition

	Hardness (LBBF) [HV]	Corresponding *VED* [J/mm^3]	Hardness (Wrought) [HV]
Ti-5-5-5-3	~285 – 295 (Zhang et al., 2022)	69	314 ± 16 (Solution-Treated Condition) (Opini et al., 2016)
Beta 21S	278 ± 5 (Macias-Sifuentes et al., 2021)	Unknown	274 (Solution-Treated Condition) (Wilson, 2017)

Similarly, the tensile properties of LPBF-produced Ti-5-5-5-3 and Beta 21S are comparable with that of the wrought counterparts in the solution-treated condition, as shown in Table 7. According to Colombo-Pulgarín et al. (2021), high ductility and low hardness are typical of Ti-5-5-5-3 in the as-built condition when compared to Ti-6-4. Moreover, Beta 21S demonstrates higher ductility and lower hardness when compared to Ti-5-5-5-3. This makes sense as ductility decreases with a decrease in Mo-Eq. Beta 21S exists as metastable β at room temperature and, consequently, behaves in a more ductile manner. Ti-5-5-5-3, being near-β, shows a comparative increase in hardness due to the precipitation of α-phase which typically occurs in the heat-affected zone, reaching temperatures close to the β-transus temperature. The heat-affected zone

may also exceed the β-transus temperature and cause the dissolution of pre-existing α-phase. Ti-5-5-5-3 is thus capable of showing a larger variation in hardness and ductility depending on the energy input and cooling rates, causing different morphologies and α-β ratios.

Table 7: Comparison between Tensile Properties of LPBF-Produced T-5-5-5-3 and Beta 21S and that of Wrought Counterparts in the Solution-Treated Condition

	Mechanical Properties	Ti-5-5-5-3		Beta 21S	
LPBF	σ_Y [MPa]	838 ± 9		917 ± 1	(Macias-Sifuentes et al., 2021)
	σ_T [MPa]	885 ± 7 MPa	(Zhang et al., 2022)	946 ± 19	
	e_f [%]	6.8 ± 0.6		25.3 ± 3.0	
Wrought (Solution-Treated Condition)	σ_Y [MPa]	~800		~883	(Boyer, Welsch and Collings, 1994)
	σ_T [MPa]	~880	(Cotton et al., 2015)	~931	
	e_f [%]	~15		~12	

2.6 Heat Treatment

During the LPBF process, residual stresses are thermally induced because of the steep temperature gradient present during the formation of layers, causing rapid solidification. Underlying layers are re-heated and then cooled, restricting the contraction of the solidified layers below. Tension between layers form as a result (Malefane, du Preez, & Maringa, 2017). Therefore, it is important to consider heat treatment to relieve the residual stresses found in metastable β-titanium alloys and to strengthen through the precipitation of secondary α-phase. Stress relief annealing is often employed as an intermediate step during thermo-mechanical processing. It is usually performed at sub-transus temperatures in the α+β-phase field, preferably followed by air cooling. Water or oil cooling may cause additional residual stresses due to the high cooling rate.

Furthermore, the concept of hardenability is considered, because it is related to the ability of a metastable or near-β alloy to strengthen during solution treatment and aging. Hardenability is characterized by a titanium alloy's ability to produce an age-hardening response in the supersaturated β-phase, whereby the ability to retain the metastable β-phase results in higher hardenability with increasing section thickness.

During quenching, the formation of α'-martensite and orthorhombic α''-martensite must be suppressed for the alloy to be hardenable. Additionally, it is not favorable for secondary α-phase to form during quenching, because it restricts the growth of primary β-phase, which improves ductility. As such, alloys are heat treated according to Figure 15 in which solution treatment occurs at either super-transus or sub-transus temperatures, soaked at said temperatures, and then quenched. Solution treatment is often followed by isothermal aging in the α+β field to achieve desirable mechanical properties (Malefane, du Preez, & Maringa, 2017).
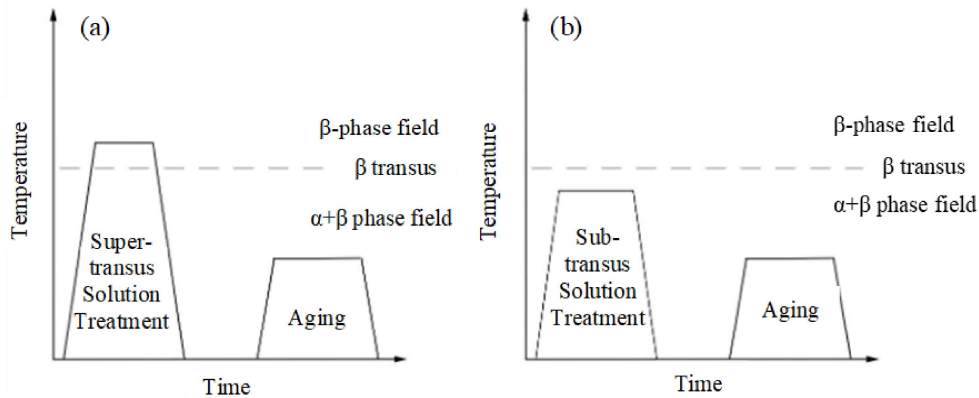
Figure 15: Schematic representation of (a) super-transus and (b) sub-transus solution treatments followed by aging (Malefane, du Preez, & Maringa, 2017)

Metastable β alloys with high Mo-Eq values are solutionized at temperatures just above the β-transus temperature, whereas metastable β alloys with lower Mo-Eq values and near-β alloys are solutionized at temperatures slightly below. These two categories are differentiated as β and α+β solution treatments, respectively.

Cases in which β solution treatments are utilized, a homogenous microstructure forms, consisting of β-phase. The alloy is highly ductile in this state but lacks sufficient strength. Therefore, the alloy is aged in the α+β field to grow the primary α-phase. However, this comes at the expense of some of the ductility as the metastable β-phase decomposes into secondary α-phase precipitates.

For α+β solution treatments, the β-phase is enriched according to the lever rule for equilibrium phase diagrams. However, primary α-phase limits the growth of β-phase by pinning its grain boundaries. As a result, the alloy has significantly higher strength but at the expense of the ductility.

As stated, solution treatment is often followed by aging, in which there are four aging methods, viz. isothermal aging at high temperatures, isothermal aging at low temperatures, duplex (two-step aging), and direct aging. High-temperature aging usually occurs between 85 and 195 °C below the β-transus temperature for durations of less than 24 hours. Brittle isothermal ω-phase and β'-phase, which are intermediate metastable phases, do not form during high-temperature aging. However, these form during low-temperature aging and, as a result, the duration is much longer than high-temperature aging.

Referring to Figure 2, for alloys with low Mo-Eq values, the aging process results in the formation of isothermal ω-phase before equilibrium α-phase is formed. This intermediate metastable phase causes embrittlement of the alloy where the precipitates are sheared during deformation, resulting in strong localized slip. Additionally, premature fracture is expected with little to no ductility. Therefore, in such cases, high-temperature aging is preferred to prevent this embrittlement. Furthermore, alloys with higher Mo-Eq values form the intermediate β'-phase, which serve as nucleation sites for the precipitation of secondary α-phase.

Duplex aging is a combination of low- and high-temperature aging, usually carried out in that order for short periods of time. Depending on the Mo-Eq value of the alloy, either isothermal ω-phase or β'-phase will form during the first step. Transformation is completed in the second step. Research has shown that duplex aging results in a more uniform and fine dispersion of α-phase precipitates, causing a good balance between strength and ductility.

The fourth and final method of aging, viz. direct aging, is simply aging without an initial solution treatment, and is usually performed after cold working. A homogenous distribution of secondary α-phase forms as a result. Furthermore, this method of aging deters the formation of brittle ω-phase. The treatment must, however, be customized according to the composition of the alloy (Kolli & Devaraj, 2018).

3. DESIGN OF EXPERIMENT

This chapter outlines the design of the experiment carried out to optimize the density of LPBF-produced Ti-5-5-5-3 and Beta 21S, and create processing windows for each alloy, as was done for Ti-6-4 by Promoppatum, Onler, and Yao (2017). The design of the experiment seeks to define a set of processing parameters from which the processing windows of dense parts can be determined, using D-optimal design.

3.1 Design Constraints and Preliminary Planning

As discussed previously, the *VED* can be varied by changing the process parameters, i.e., scan speed, laser power, hatch spacing, and layer thickness. The density of a fabricated part is influenced by these parameters and the resulting *VED*. Numerous *VED* values can be generated with multiple combinations of parameters. However, unfavorable melt pool characteristics and porosity may form. The parameters varied in this research are laser power, scan speed, and hatch spacing, where layer thickness is kept constant. Varying the layer thickness could potentially require multiple builds. Given the limited resources and funding, this will not be possible in this study. However, keeping the layer thickness constant has utility in reducing the complexity of the experimental design by establishing a correlational or causal relationship between the parameters of interest and porosity.

The outcome of this section seeks to establish the range of parameters to which the design space is constrained. In doing so, the boundaries of a processing window can be defined for each alloy. The boundaries are important for indicating the onset of either over melting, incomplete melting, or balling. The range of process parameters must, therefore, allow for the possibility of nonoptimal density. As such, the parameters are constrained according to information inferred from the literature.

Promoppatum, Onler, and Yao (2017) define a processing window for Ti-6-4 and suggest that the established processing window can be extended to other materials or similar processes, provided there are limited modifications. The processing window in Figure 8 and the accompanying boundaries and criteria – along with other relevant research – are used as a guide for the design of this experiment. Furthermore, the experiment will include Ti-6-4 as a control group. Ti-6-4 will serve as a means to assess the validity of this study by comparing the results obtained with what is observed by Promoppatum, Onler, and Yao (2017) and other available research materials.

First, the scan speed is considered. The properties and accompanying values required to calculate the minimum velocity per Equation 3 can be seen in Table 8. The values stipulated are taken from single sources since the outcome is only used as a guideline and, therefore, does not require stringent accuracy.

Table 8: Required Properties to Calculate the Minimum Velocity as per Equation 3

	Required Properties* and Parameters for Equation 3					
	Solid Density, ρ_s [kg/m³]	Specific Heat, C_p [J/kg°C]	Layer Thickness, l [μm]	Thermal Conductivity, k_s [J/m°C]	Laser Radius, r_0 [μm]	Source
Ti-5-5-5-3	4650	500	30	5.3	40	(Parida and Maity, 2019)
Beta 21S	4940	710	30	7.5	40	(Boyer, Welsch and Collings, 1994)

*The stipulated properties were recorded at room temperature.

The resulting minimum velocity for each alloy can be seen in Table 9. According to Promoppatum, Onler, and Yao (2017), Equation 3 suggests that for the melt pool configuration to be controlled by the *VED*, the scan speed needs to be higher than the velocity calculated. The properties reported in Table 8 may vary slightly for the powder sourced. Therefore, to account for any variation among properties which may increase the velocity calculated in Equation 3 and to keep the experiments identical for both alloys, a minimum velocity of 400 mm/s.

Table 9: Calculated Minimum Velocity for Scan Speed Parameter Constraint

	Minimum Velocity, $V_{min} > \frac{2r_0 k_s}{l^2 \rho_s C_p}$ [mm/s]
Ti-5-5-5-3	203
Beta 21S	190

From the processing window in Figure 8, the maximum scan speed reaches just over 2000 mm/s. Since the purpose of the experiment is to define a clear processing window, a maximum scan speed of 2500 mm/s is used.

The range of power used in the research carried out by Promoppatum, Onler, and Yao (2017) spans 100 – 400 W. *Metal Heart* was contracted to print the samples using an SLM®280HL machine from *SLM Solutions*, which has a rated power of 400 W. However, machine operators suggested that a maximum power of 350 W be used because the power output is capped below 400 W. The range of laser power is thus set to 80 – 350 W.

33

Regarding hatch spacing, the range considered is 40 – 110 μm. Many research papers use a hatch distance within this range (Promoppatum, Onler, & Yao, 2017) (Bakhshivash et al., 2019).

Given that *VED* is a function of laser power, scan speed, and hatch distance, it can be used to further constrain the design space. Based on the research carried out by Promoppatum, Onler, and Yao (2017), a *VED* range of 36.9 – 98.3 J/mm^3 for Ti-6-4 is defined to establish optimal density within the processing window, while Bakhshivash et al. (2019) define a range of 50 – 175 J/mm^3 for Ti-5-5-5-3 in which the highest values of relative density were obtained. For Beta 21S, Pellizzari et al. (2020) define a more conservative range of 40 – 90 J/mm^3 in which process parameters were optimized to achieve a maximum density. Therefore, to conglomerate the information mentioned and establish an extensive processing window, a range of 30 – 250 J/mm^3 is used for the research carried out.

A summary of the process parameters is shown in Table 10 below.

Table 10: Process Parameter Constraints

Process Parameter	Range	Unit
Laser Power	80 – 350	W
Scan Speed	400 – 2500	mm/s
Hatch Spacing	40 – 110	μm
VED	30 – 250	J/mm^3
Layer Thickness	30	μm

3.2 D-Optimal Design

The design constraints discussed in the previous section were implemented in *Design-Expert* (version 13) software. *Design-Expert*, a statistical software package, is a statistical analysis tool, which provides guidance for users to plan, execute, and analyze experiments effectively. Using the design of experiments method, one can separate important from insignificant factors, qualify the relationships between the factors and responses, and determine the optimal factor settings.

Optimal designs estimate statistical models with fewer experimental runs, thereby reducing the cost of experimentation. For this study, the response surface method is implemented to produce a mathematical model that can be used to predict a response. Since the primary objective of this study is to determine the optimal density, the desired outcome is a prediction of porosity in response to the various combinations of process parameters. When the minimum porosity points are found, the optimal density is determined. Porosity is the percentage of the void space. Calculating the relative

density of the material, being the fraction of the volume occupied by the mass of the substance of interest, one can determine the porosity.

The D-optimal design approach is adopted in which the optimal set of design runs are chosen from a candidate set of possible treatment runs using the D-optimality criterion. Consider Equation 4 below where Y is a matrix of observations – the response – and X is the matrix of design variables. The term B denotes the vector of tuning parameters or coefficients, and e is the vector of errors.

$$Y = X \cdot B + e \tag{4}$$

To estimate B, the least-squares method is implemented using Equation 5.

$$B = (X^T \cdot X)^{-1} X^T \cdot Y \tag{5}$$

The D-optimality criterion states that the optimal set of points in the experiment maximizes the determinant $|X^T X|$ and, therefore, leads to response surface models in which the maximum variance of the predicted response is minimized. Matrix X is a random set of possible candidate points selected based on the postulated model. From this initial candidate set, a subset that maximizes the determinant $|X^T X|$ is selected (Myers & Montgomery, 1995).

The number of model points needed increases proportional to the number of factors studied. Therefore, for a design with three factors – as in this study – at least 4, 10 and 20 points are needed for linear, quadratic, and cubic models, respectively. It is unlikely that laser power, scan speed, and hatch spacing affect porosity independently because melting is influenced by the energy input, which is a function thereof. Therefore, there are likely nonlinear interactions between parameters that contribute to the pore volume, and, as such, a linear response is not likely. It was hypothesized that the response would fit a quadratic model because this is the next highest order after a linear response, and it was thought to maintain a conservative approach to the experimental design. However, there may be more complex interactions between the parameters. Therefore, should the model be best described as cubic, additional points are added to the design to accommodate a cubic response. Providing contingency to accommodate quartic and higher-order models is not considered feasible for this study. Additional information on the model points can be found in Table 11, including a description of each.

Apart from the required and additional model points, more unique points are necessary to test how the model fits the data. These points are used in a "lack of fit" test for the model and, therefore, must be at locations in the design space that are different from the model points. The *Design-Expert* software suggested at least three lack-of-fit points be used, in which case it was decided to use five.

Table 11: D-Optimal Design Model-Point Information

	Description	Quantity of Design Points
Required Model Points	Minimum number of runs required	10
Blocks	Number of experimental units that are similar to one another	1
Additional Model Points	Number of additional points added to the design to increase the robustness of the model	25
Lack-of-Fit Points	Replicated points used to determine whether a regression model is a poor fit to the data or not	5
Replicate Points	Model points with repeating combinations of process parameters	5
Additional Center Points	Additional points set midway between high and low values	5
Total Number of Runs	Sum of all model points	50

Introducing blocks or blocking can be used to reduce or eliminate the contribution to experimental error caused by nuisance factors. It was decided to limit the number of blocks to one, which means that blocking was not implemented in this design, because the experiment was performed under very controlled conditions. All samples were printed simultaneously, meaning that the conditions were kept constant for all samples. Moreover, introducing more blocks to the design would require additional builds. Funding for which is unavailable and defeats the purpose of implementing D-optimal design in this study.

Centerpoint runs are interspersed among the experimental runs to provide a measure of process stability and inherent variability, and to check for curvature in the model. According to Myers et al. (1992), the best overall design performance occurs when the number of center points ranges between two and five. Therefore, it was decided to use a maximum of five center points in the design. Typically, the center points of the design are repeated to give an adequate estimate of the variation of the response.

Furthermore, replicates of some model points are necessary to estimate the experimental error. *Design-Expert* suggested adding four replicate points to the design. It was decided to add five, thereby bringing the total number of experimental runs to 50.

36

3.3 Model Diagnostics

It is important to consider that not all terms have significance for the response of the model and may reduce the accuracy with which the model predicts porosity. Therefore, certain terms are removed to improve the fit of the model.

Before the significance of terms is analyzed, the need for a response transformation is assessed. A transformation is required if the residuals within the model vary with the magnitude of the predicted values (Miller, 1984). Ideally, the error should be constant for the model to accurately predict the response. Therefore, it may be necessary to apply a response transformation to ensure the normality of the residuals. *Design-Expert* offers several response transformations, including square root, natural log, base-10 log, inverse square-root, inverse, and power.

Thereafter, the significance of each term in the model is assessed according to four different criteria offered by the software, viz. the p-value criterion, Akaike information criterion (AICc), Bayesian information criterion (BIC), and adjusted R^2 criterion. The p-value criterion selects terms with a p-value greater than 0.1 and suggests the removal of said terms. The AICc criterion suggests the removal of terms which reduce the overall AIC value of the response; the lower the value, the better the fit of the model. BIC suggests terms similar to AIC. The adjusted R^2 criterion is implemented by suggesting the removal of terms that reduce the overall adjusted R^2.

After the insignificant terms are removed, the modified response is compared with the original model. The models are compared based on the normal plot of residuals and the difference between the adjusted and predicted R^2 values, which gives insight into the distribution of error throughout the model and how much influence the model has on the variation seen. The normal plot of residuals illustrates the theoretical percentiles versus the observed percentiles. The plot should be approximately linear if the error terms follow a normal distribution. The adjusted R^2 which is a modified version of R^2, is then taken into account. It is a representation of the amount of variation in the data that is explained by the model. The R^2 measurements tend to be biased by independent variables; the adjusted R^2 adds precision and reliability by considering its impact. The predicted R^2, on the other hand, represents the amount of variation in predictions that is explained by the model. Ideally, both should be as close to unity as possible with a maximum difference of 0.2 between them – this is a general rule of thumb used to show that the model is not over-fit (Anderson & Whitcomb, 2017).

Based on whether an improvement is seen in the normal plot of residuals and R^2 values, the modified or original model is selected to predict porosity. Moreover, after the removal of terms, the model response is assessed and compared to those of the different orders by evaluating the graphs of observed (actual) porosity versus the predicted

porosity. A point within the ideal graph should fall directly on a 45° line, indicating that the model is capable of accurately predicting the response. The model is then selected on the basis of the best fit of this graph.

3.4 Scan Strategy

According to the studied literature, it was decided to implement a 67° scan rotation. The vector of the scan velocity is 67° relative to the previous layer. Given that the layer thickness is kept constant at 30 μm, it can be inferred from the study by Kumar, Prakash, and Ramamurty (2018) that a scan rotation of 67° is appropriate to achieve relatively isotropic properties in Ti-6-4.

An additional reason for implementing such a scan strategy is due to the fact that limited powder is available for this research because of the substantial cost incurred in sourcing and obtaining the material. Samples can only be printed horizontally on the build plate as the volume of powder that is required to build samples vertically exceeds the available powder volume. Therefore, because this scan strategy tends to reduce anisotropy somewhat, the properties achieved should give an indication of the behavior expected in all directions without the need for building both parts that align with and are perpendicular to the build direction. Importantly, the density should not be affected by the orientation of the sample.

A graphical representation of the how the layers in cylindrical samples are orientated can be seen in Figure 16 in which the build direction coincides with the z-axis.
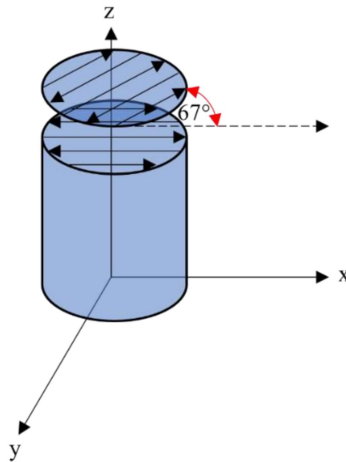
Figure 16: A graphical representation of the scan strategy implemented (not drawn to scale).

38

The samples contain 333 layers, all of which are 30 μm thick, totaling a built height of 10 mm. The samples were printed directly onto the base plate.

4. METHODS AND MATERIALS

This chapter outlines the methodology followed to achieve the project objectives to reach the overall objective of the investigation. This entails a description of the methods and materials used to gather the porosity data for the processing windows, as well as the sample preparation and testing techniques used to determine the microstructures, and hardness and tensile properties of Beta 21S and Ti-5-5-5-3. A schematic illustrating the experimental process carried out can be seen in Figure 46 in Appendix A: Experimental Methodology, along with a table outlining the experimental methods each sample has undergone (Table 41).

4.1 Powder Characterision

The approximate 10th, 50th and 90th percentiles of the particle size distribution for both alloys is $d_{10} = 15$ μm, $d_{50} = 30$ μm, and $d_{90} = 45$ μm, respectively, where d denotes the diameter. The nominal chemical composition of the primary alloy constituents of ANCOR Ti-5-5-5-3 and ANCOR Ti Beta 21S Grade A from *Hoeganaes Specialty Metal Powders: ©GKN* can be seen in Tables 12 and 13, respectively, as provided by the supplier. Both powders were produced using gas atomization, resulting in spherical powder particles.

Table 12: ANCOR Ti-5-5-5-3 Chemical Composition as Supplied

Chemical Composition Nominal (wt. %)						Maximum (wt. %)			
Ti	Al	Mo	V	Cr	Fe	O	C	H	N
Bal.	4.5	5.1	4.8	2.9	0.42	0.13	0.01	0.003	0.03

Table 13: ANCOR Ti Beta 21S Chemical Composition as Supplied

Chemical Composition Nominal (wt. %)					Maximum (wt. %)			
Ti	Al	Mo	Nb	Si	O	C	H	N
Bal.	2.9	15.3	2.93	0.25	0.14	0.01	0.002	0.023

The specific particle size distributions of each alloy can be seen in Table 14, as provided by the supplier, which were determined using laser diffraction particle size analyses.

Table 14: Specific Particle-Size Distribution of Ti-5-5-5-3 and Beta 21S Metal Powders

	Particle-Size Distribution		
β Alloy	d_{10} (μm)	d_{50} (μm)	d_{90} (μm)
Ti5553	14	31	49
Beta 21S	13	27	49

The apparent densities of the Ti-5-5-5-3 and Beta 21S powders are 2.3 and 2.6 g/cm^3, respectively, as reported by the supplier.

Chemical composition, morphology and particle size analyses were performed according to ASTM F3049-14 to compare information received from the supplier using the methods and instruments tabulated in Table 15.

Table 15: Powder Characterisation Analysis Techniques and Instrumentation

Characteristic	Method/Technique	Instrument
Chemical Composition Analysis	Inductively Coupled Plasma-Optical Emission Spectroscopy (ICP-EOS)	ICP-OES spectrometer (Arcos FHE12, *SPECTRO Analytical Instruments GmbH*, Germany)
Particle Size Distribution	X-Ray Computed Tomography Scanning	nano-CT scanner (Nanotom S, *General Electric Sensing and Inspection Technologies/Phoenix X-ray GmbH,* Germany)

The chemical composition analysis was performed by the *South African Nuclear Energy Corporation* (*NECSA*) at the *Pelindaba Analytical Laboratory*.

X-ray computed tomography (CT) scans were used to analyze Beta 21S and Ti-5-5-5-3 powder samples to determine the sphericity, which is a measure of how spherical an object is, and confirm the particle size distribution provided by the powder supplier. CT scans were performed at the *Central Analytical Facilities* (*CAF*), Stellenbosch, by Muofhe Tshibalanganda and Carlyn Wells. Details regarding the CT scanning apparatus can be found in Table 16.

Table 16: CT Scanning Instrumentation Specifications

X-Ray Filament	240 kV/320 W
Capable Voxel Resolution	1.5 μm
Reconstruction Software	Datos
Data Analysis Software	VGStudioMax 3.2, *Volume Graphics*, USA

It is important to note the shortcomings of the apparatus. The resolution of the CT scanning, which is limited to the scan resolution and the time allotted to testing, allows

small defects to be overlooked. In this study, a minimum voxel size of 5 μm was possible, so pores or defects smaller than 5 μm diameter will not be detected.

4.2 Printing Process

The machine parameters reported in Table 17 were used on a selective laser melting system (SLM®280HL, *SLM Solutions GmbH,* Germany).

The SLM®280HL uses a hopper to feed the powder into a coater which moves across the powder bed to distribute the next layer. The build chamber uses argon gas to create the inert atmosphere. Laminar gas flow across the powder bed ensures the bed remains soot free and that previously scanned tracks do not disrupt subsequent tracks with spatter. The machine also supports baseplate heating, which was implemented in this study to reduce the effects of residual stress on the properties. The base plate was kept at a temperature of 200 °C throughout the build for all alloys. A standard scan rotation of 67° is implemented on the SLM®280HL machine.

Table 17: Fixed Machine Parameters

	SLM®280HL
Beam Focus Diameter [μm]	80
Stripe Length [mm]	10
Rated Laser Power [W]	400
Maximum Scan Speed [mm/s]	10 000
Oxygen Threshold Level [%]	0.05

4.3 Sample Geometry

A cylindrical geometry with both a diameter and height of 10 mm was used. This geometry was deemed simple enough to implement in this study. More complex geometries may impede the heat dissipation. Since the *VED* is varied significantly, this may cause inconsistencies in the data should a geometry with sharp or irregularly shaped edges be used.

The geometry used for the tensile samples is described in section 4.7 along with the tensile testing procedure.

50 cylindrical samples were printed for each alloy, termed as "model samples" as they were used for the characterisation of the D-optimal model used to predict porosity. Each sample is number 1 – 50 followed by their respective parameter sets in parentheses. For example, Sample 1 has a respective power-speed-hatch-spacing

combination of 350 W, 1167 mm/s and 40 μm, respectively, and is, therefore, denoted as Sample 1 (350-1167-40).

Three parameter sets are tested for their tensile properties. Each group is named T1, T2, T3 and is grouped according to the *VED* used, being high, medium, and low, respectively. Three samples are printed for each group, totalling nine tensile samples per alloy.

4.4 Archimedes' Density Testing

To analyze the response of the generated nonlinear regression model, in which the objective is to minimize the porosity, data are added to the *Design Expert 13* software to generate a response surface for further enhancement of the model. The densities of the as-built samples are used to establish the respective porosities. First, it is important to define the difference between relative and absolute density. Absolute density is the ratio between the mass and the volume of a body. Relative density, on the other hand, is the ratio between the density of an object and the density of some other reference object at some given temperature. Absolute density is usually expressed in grams per cubic centimetre (g/cc), while relative density is dimensionless.

The Archimedes' principle was employed to determine the relative density of each sample. This form of testing is non-destructive, as well as economic and a fast procedure with which to determine the density of solid materials. A precision scale (ABT 120-5DM, *Kern & Sohn GmbH*, Germany) with a sensitivity of 0.0001 g was used along with a specific density measurement device according to ASTM B311-13. To prevent the formation of air bubbles on the surface of the samples, isopropanol was used as the suspension liquid instead of distilled water.

To ensure the accuracy of results, the absolute density of the isopropanol used in the calculation was measured by means of a 25 mL Bingham pycnometer in accordance with ASTM-D1217 in conditions used to weigh the samples densities. The pycnometer was calibrated and found to have a volume of 24.509 mL. The relative densities of the Beta 21S and Ti-5-5-5-3 samples were calculated using the theoretical densities of Beta 21S and Ti-5-5-5-3 being 4.94 and 4.65 g/cc, respectively, as reported in Table 8.

4.5 Microscopy Analysis

The pore and microstructural analyses were performed using optical and scanning electron microscopy (OM and SEM, respectively). OM was done using an inverted metallurgic microscope (GX51, *Olympus Co., Ltd.*, Japan*)*, while SEM analyses were conducted using a high-resolution field emission scanning electron microscope (MERLIN, *Carl Zeiss AG GmbH,* Germany). An *electron high tension* (*EHT*) *voltage*

of 20 kV and backscattered electron detector (BSD) were used with a working distance range of 8.5 – 9.5 mm.

4.6 Microhardness Testing

Vickers microhardness tests were conducted on the cross sections of the longitudinal and lateral planes, being the z and x-y planes, respectively. The surfaces on which the microhardness measurements were taken, as well as the coordinate system, can be seen in Figure 17.
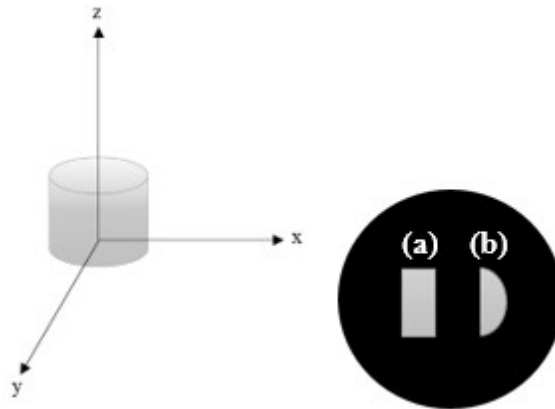
Figure 17: a) Longitudinal (z plane) and b) lateral (x-y plane) cross-sectional surfaces on which Vickers microhardness measurements were taken.

Measurements were initially taken at Stellenbosch University using an *Emcotest Durascan* automatic indentation device with a type 556 diamond-shaped indenter. Testing was carried out according to ASTM E348-10. For each measurement, a load of 2 kg was applied for 10 seconds. Ten measurements were made at random on each surface. Indentations were analyzed using a 40x/0.65 *Nikon* lens with a depth and field width of 0.17 and 0.6, respectively. Indentation diagonals were measured using *ECOS Workflow V2.10* software to determine microhardness values.

Testing was later done on a Vickers-hardness tester (HWDM-3, *TTS. Unlimited, Inc.*, Japan) at the *CME* under the same loading conditions previously mentioned because the apparatus at Stellenbosch University had to undergo maintenance and recalibration.

4.7 Tensile Testing

The tensile performance of three sets of parameters, based on varying levels of *VED* and hardness as reported in Tables 30 and 31, were calculated in Chapter 5.

Coincidentally, the same sets of parameters were used for both alloys because the corresponding porosities obtained were less than 1 % and showed significant variation in hardness and *VED*. The selected parameters are reported in Table 18. Tables 19 and 20 show the corresponding hardness, *VED*, and porosity found when analyzing the model samples.

Three tensile samples per parameter set (T1, T2 and T3) were built for each alloy, according to the dimensions set out in ASTM Standard E8/E8M – 21 (2021) for powder-metallurgy, flat, tension test specimens. A total of nine tensile samples were printed for each alloy. A technical drawing of the tensile samples as outlined by the standard is shown in Figure 53 in Appendix D: Tensile Sample and Property Information. The technical drawing was detailed from the CAD model made, which was converted to STL file format. The samples were machined at *Executive Engineering* according to the technical drawing shown in Figure 54. This was done to ensure that the cross-section in the test section of the samples was constant to prevent an uneven distribution of stress during testing.

Tensile testing was performed on a tensile testing machine *(*Instron 5982*, Illinois Tool Works Inc.,* USA) with a 100kN force transducer (model *2580*). The loading was applied with a strain rate of 0.47 mm/min. The displacement in the 25.4 mm gauge section was measured using Digital Image Correlation (DIC) cameras (Imager M-lite 5M and E-lite 5M, *LaVision GmbH,* Germany). The software used to analyze the results is *Strainmaster* 1.3.0.

Table 18: Parameters Sets Selected for Tensile Testing: Beta 21S and Ti-5-5-5-3

Sample No.	VED [J/mm^3]	Power [W]	Scan Speed [mm/s]	Hatch Spacing [mm]
T1.	250	350	1167	0.04
T2.	167	80	400	0.04
T3.	47	248	2500	0.07

Table 19: Corresponding Hardness and Porosity Readings for Selected Tensile-Sample Parameters: Beta 21S

Sample No.	Hardness [HV] Lateral Plane	Hardness [HV] Longitudinal Plane	Scaled Porosity [%]
T1.	299 ± 9	305 ± 6	0.546
T2.	282 ± 6	290 ± 5	0
T3.	266 ± 8	277 ± 5	0.501

45

Table 20: Corresponding Hardness and Porosity Readings for Selected Tensile-Sample Parameters:
Ti-5-5-5-3

Sample No.	Hardness [HV] Lateral Plane	Hardness [HV] Longitudinal Plane	Scaled Porosity [%]
T1.	334 ± 25	365 ± 46	0.400
T2.	297 ± 9	308 ± 9	0
T3.	276 ± 8	278 ± 5	0.241

4.8 Elemental, Oxygen and Nitrogen Analyses

The elemental, oxygen and nitrogen analyses were performed at *NECSA*. The chemical composition was determined using an *ICP-OES* spectrometer (Arcos FHE12, *SPECTRO Analytical Instruments GmbH*, Germany). A combustion analyzer (ELTRA-ONH, *ELTRA GmbH*, Germany) was used to perform the oxygen and nitrogen analysis.

5. RESULTS

This chapter outlines the experimental and numerical/regression analysis results from the procedures described by the design of the experiment and the experimental methods. The results reported are used to develop the processing windows, and to characterize the hardness and tensile properties of Ti-5-5-5-3 and Beta 21S processed within the limits of the processing window.

5.1 Powder Characterisation

Tables 21 and 22 compare the chemical compositions measured by NECSA to those reported by the supplier.

Table 21: Ti-5-5-5-3 Chemical Composition Analyzed by NECSA Compared to Results from Supplier

	Chemical Composition Nominal (wt. %)						Maximum (wt. %)			
	Ti	Al	Mo	V	Cr	Fe	O	C	H	N
NECSA	Bal.	4.45	4.79	4.69	3.17	0.41	0.16	-	-	<10 mg/kg
Supplier	Bal.	4.5	5.1	4.8	2.9	0.42	0.13	0.01	0.003	0.03

Table 22: Beta 21S Chemical Composition Analyzed by NECSA Compared to Results from Supplier

	Chemical Composition Nominal (wt. %)					Maximum (wt. %)			
	Ti	Al	Mo	Nb	Si	O	C	H	N
NECSA	Bal.	2.4	11.7	2.20	0.27	0.21	-	-	<10 mg/kg
Supplier	Bal.	2.9	15.3	2.93	0.25	0.14	0.01	0.002	0.023

There are slight discrepancies (~0.5 wt. %) in the chemical composition of the alloy elements when comparing the information supplied by the *Hoeganaes Specialty Metal Powders: ©GKN* and the results from the analysis performed by *NECSA*. The largest discrepancy found was for the molybdenum in Beta 21S where a difference of 3.6 wt. % is seen.

The 10th, 50th, and 90th percentiles of the particle size distribution were analyzed using CT scanning. The results for each powder are compared with the information supplied by *Hoeganaes Specialty Metal Powders: ©GKN* in Table 23. The 10th percentile closely coincides with that reported by the supplier. However, there are relatively large differences between the 50th and 90th percentiles, viz. ~9 and ~15 μm, respectively. This can in part be explained by the 5 μm voxel size used, which could result in an inaccurate representation of the true particle size distribution. It is important to note

that laser diffraction particle size analyses were performed by the supplier to determine the percentiles of each powder. This is a more accurate technique.

Furthermore, powder samples were taken from the top of the powder containers. The powders should have been mixed prior to taking samples for analysis because smaller particles may have settled at the bottom of the containers during transit and storage. The samples taken are thus not an accurate representation of the total powder.

Table 23: Comparison of Particle Size Distribution Received from Supplier with Analysis Performed using CT Scanning

		Particle-Size Distribution		
		d_{10} (μm)	d_{50} (μm)	d_{90} (μm)
CAF	Ti-5-5-5-3	14.2	21.2	37.6
	Beta 21S	12.9	19.2	31.3
Supplier	Ti-5-5-5-3	14	31	49
	Beta 21S	13	27	49

The mean sphericities of the particles in each powder were also determined. Beta 21S and T-5-5-5-3 each report a mean sphericity of 0.59 ± 0.06 and 0.57 ± 0.06, respectively. The closer to unity sphericity is, the more spherical a particle is. Although the results suggest relatively low sphericities, this can in part be explained by Figure 18 in which the presence of satellite particles is revealed. However, the values do not appear to accurately represent the sphericity based on what is seen in Figure 18 and should be closer to one that what was obtained. This would suggest that the means of analysis (XCT) is not accurate enough. Laser diffraction particle size analysis should be employed in future to provide better insight into the particle size distribution and sphericity of the alloy powders.
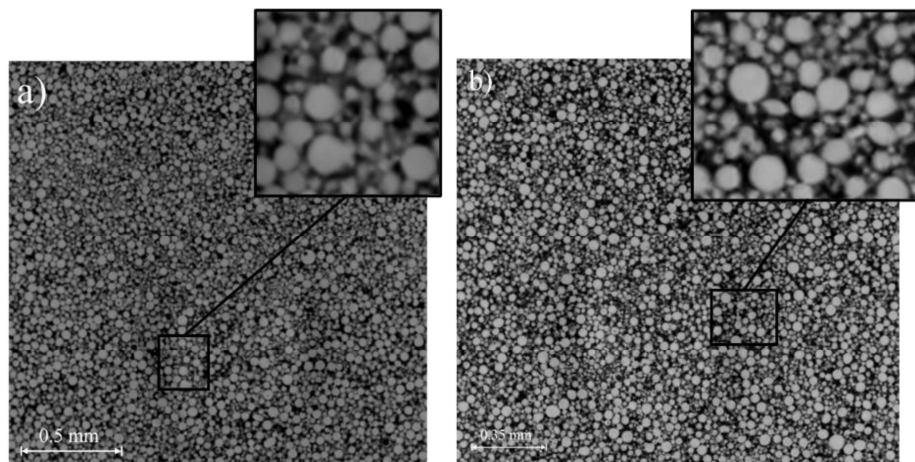
Figure 18: The powder morphology of a) Beta 21S and b) Ti-5-5-5-3 showing evidence of poor sphericity

5.2 Experimental Design

The design points generated by *Design-Expert* are shown in Figures 19 and 20. The exact combinations of process parameters for each experimental run can be found in Table 41 in Appendix B: Detailed Design Matrix and Porosity Data.
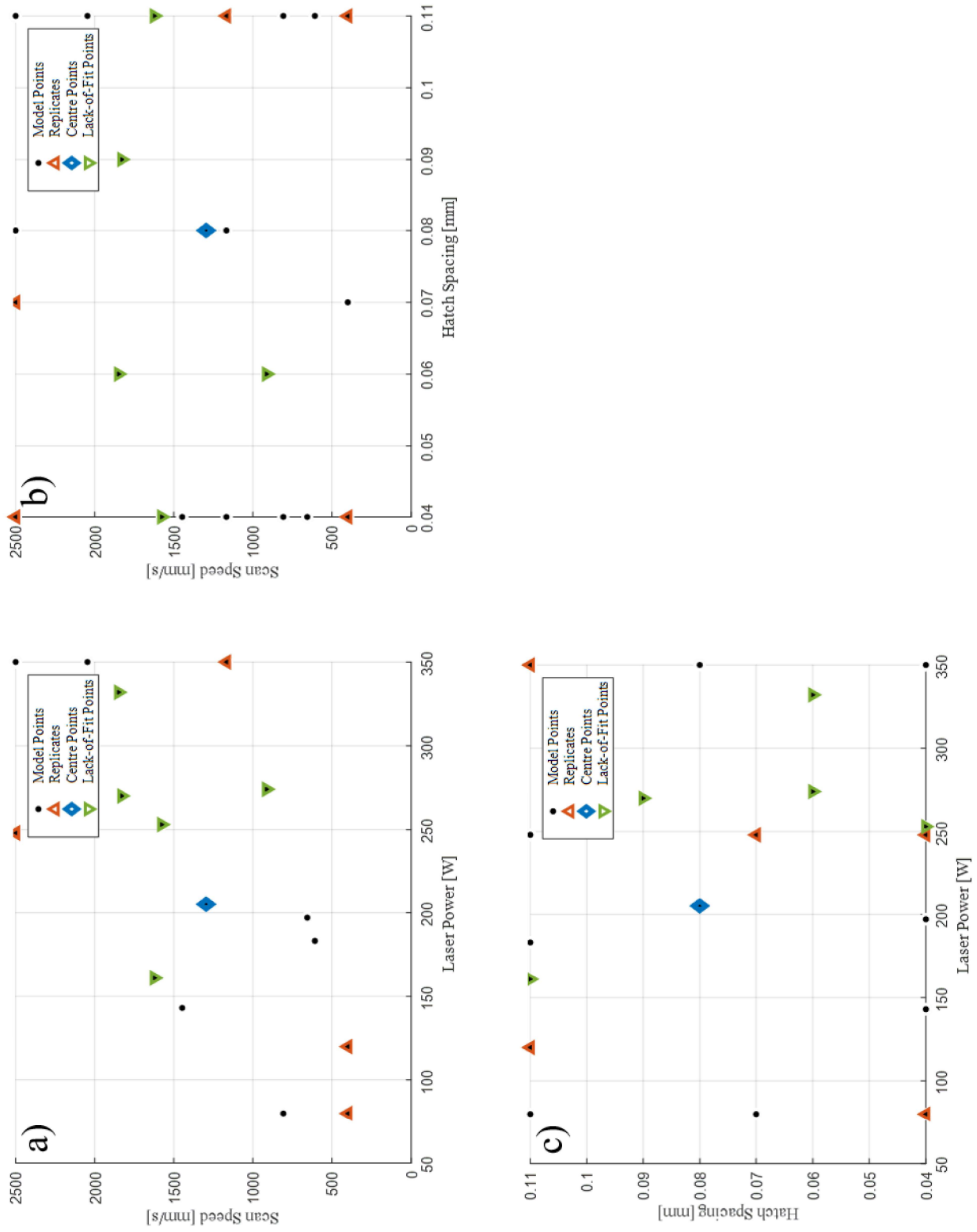
Figure 19: A scatter plot matrix of the model points in the constrained design space: a) v vs P, b) v vs h, and c) h vs P
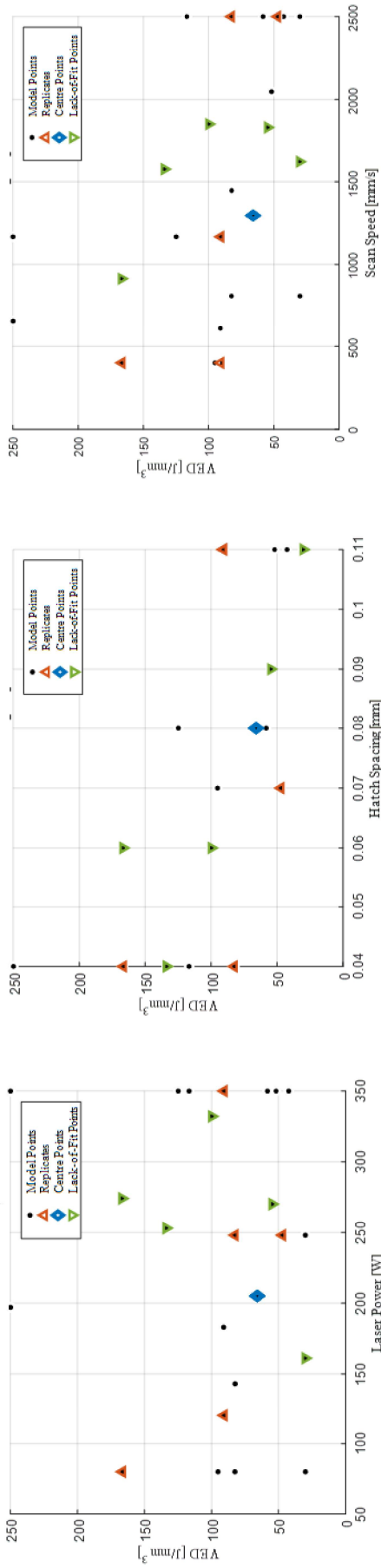
Figure 20: *A scatter plot of the model points in constrained design space: VED vs laser power, hatch spacing and scan speed, respectively*

51

5.3 Archimedes' Density Testing Results

The results reported in this section were obtained using the methods described in Section 4.3. The density data can be found in Appendix B: Detailed Design Matrix and Porosity Data. The respective ranges of absolute density, relative density, and percentage porosity determined from the density testing can be seen in Table 24 below. Recalling the theoretical densities used to calculate the relative densities – 4.94 and 4.65 g/cc for Beta 21S and Ti-5-5-5-3, respectively (Table 8) – it is clear from the relative densities reported for Beta 21S and Ti-5-5-5-3 that the density of the powder used is greater than the theoretical value reported, as the maximum relative density is greater than 100%. On the other hand, the Ti-6-4 powder seems to have more or less the same density as the theoretical value used (4.43 g/cc). Therefore, the results were scaled. The maximum density was set to 100%, and the rest of the readings were scaled using the maximum density, as this should not affect the model. To remain consistent, this was done for the Ti-6-4 results.

Table 24: Porosity Range of Ti-6-4, Beta 21S and Ti-5-5-5-3

	Density [g/cc]	Relative Density (Unscaled) [%]	Porosity Range (Scaled) [%]
Ti-6-4	4.29 – 4.47	96.6 – 99.6	0 – 3.29
Beta 21S	4.89 – 4.92	98.6 – 100.9	0 – 2.23
Ti-5-5-5-3	4.43 – 4.55	98.4 – 100.4	0 – 2.00

For both Beta 21S and Ti-5-5-5-3, the minimum porosity – or maximum density – was reported for the same sample, viz. Sample 45 (80-400-40) with a *VED* of 167 J/mm^3. However, this was not the case for the maximum porosity. Samples 7 (120-400-110) and 50 (248-2500-110) were reported to have the maximum porosities for Ti-5-5-5-3 and Beta 21S, respectively. The resulting *VED* of samples 7 and 50 were 91 and 30 J/mm^3, respectively.

5.4 D-Optimal Design Results

The response data was implemented in the *Design-Expert* software to generate the statistical model used to predict porosity. A summary of the respective model diagnostics for Ti-6-4, Beta 21S, and Ti-5-5-5-3 is reported in this section.

5.4.1 Model Diagnostics

As was hypothesised, the software agrees that a quadratic response best fits the data of Ti-6-4, Beta 21S, and Ti-5-5-5-3. However, it is also suggested that a cubic model be used for each. Before the statistical diagnostics of the quadratic and cubic responses

can be compared and an appropriate response is selected, it is important to consider whether a transform is required and then to note terms in each that are insignificant.

The need for a transform is determined with a Box-Cox transformation plot showing values denoted by lambda, which are the scaled natural log of the sum of squares of the residuals calculated to provide values that range between -1 and 1. If a lambda of 1 falls within the 95% confidence interval then the software suggests that no transformation is needed. According to the software, there is no need for a model transform for any of the alloys.

Next, the p-value criterion, AICc, BIC and adjusted R^2 criteria are used to evaluate the significance of each term. The terms removed from the quadratic and cubic models of each alloy are reported in Appendix C: Model Diagnostics. The effect of including and removing the terms is now considered.

The normal plot of residuals and adjusted and predicted R^2 values are considered to determine whether the removal of terms bares any significance on the overall performance of the model. Adjusted and predicted R^2, as well as the difference between them, are reported in Table 25. The normal plots can be found in Appendix C: Model Diagnostics. From here on, the terms A, B, and C denote laser power, scan speed, and hatch spacing, respectively.

Table 25: Influence of Adjusted and Predicted R^2 on Modified Original Response Orders of Ti-6-4, Beta 21S and Ti-5-5-5-3

	Original/Modified Quadratic/Cubic	Adjusted R^2	Predicted R^2	Difference
Ti-6-4	Original Quadratic	0.828	0.769	0.059
	Modified Quadratic	0.825	0.790	0.042
	Original Cubic	0.936	-0.262	NA*
	Modified Cubic	0.938	0.901	0.037
Beta 21S	Original Quadratic	0.824	0.758	0.066
	Modified Quadratic	0.825	0.790	0.035
	Original Cubic	0.895	-2.96	NA*
	Modified Cubic	0.887	0.811	0.076
Ti-5-5-5-3	Original Quadratic	0.735	0.646	0.089
	Modified Quadratic	0.739	0.655	0.084
	Original Cubic	0.836	-7.53	NA*
	Modified Cubic	0.839	0.732	0.107

* Negative predicted R^2 cannot be used to calculate difference. This indicates that the prediction tends to be less accurate that the average value of the dataset.

Regarding Ti-6-4, the term A^2 is removed – unanimously determined by the four criteria as shown in Table 46 (Appendix C: Model Diagnostics). There does not appear to be any noticeable improvement according to the normal plot of the residuals shown in Figure 47. However, there is a favourable 29 % reduction in the difference between the adjusted and predicted R^2 values. Therefore, the term A^2 is removed from the response equation. Next, the cubic response is considered. Table 47 reports the insignificant terms, which are ABC, A^2B, AB^2, BC^2, A^3, and B^3. After consulting the normal plot in Figure 48 and the results of R^2, there is a clear improvement in the fit of the graph. However, little improvement is seen in the adjusted R^2 (0.2 %). Based on the fit of the normal plot, the terms are removed from the response equation.

A very similar result is found for Beta 21S and Ti-5-5-5-3. However, for Beta 21S, only three of the four criteria exclude the same terms from the quadratic response, viz. terms AB, A^2, and B^2. The adjusted-R^2 criterion, however, does not exclude any terms. Therefore, it is decided to exclude the terms AB, A^2, and B^2, since their removal improves the residual plot in Figure 49 and lowers the difference between the adjusted and predicted R^2 values 47%. As with the quadratic response, the adjusted R^2 criterion suggests that no terms should be removed from the cubic model, while the other three criteria suggest that the same terms be removed, viz. ABC, AB^2, AC^2, B^2C, BC^2, A^3, and B^3. Said terms are consequently removed based on the improvements seen in Table 25 and Figure 50 in which an 8 and 4 % increase in the adjusted and predicted R^2 is seen, respectively.

The p-value, AICc, and BIC criteria all suggest the removal of the term AB from the quadratic equation of Ti-5-5-5-3, while the adjusted R^2 criterion does not suggest removing any terms, as with Beta 21S. Removing the term AB causes a slight improvement seen in the residual plots (Figure 51) and the difference in the values of R^2 (~0.1%). Despite this, it is thought to remove the term. Although this only slightly improves the response, the complexity of the model is reduced. Regarding the cubic response, the terms suggested for removal are shown in Table 51. After implementing the four criteria, the p-value, AICc and BIC criteria all suggest the removal of the terms ABC, AB^2, AC^2, BC^2, A^3, and B^3. According to diagnostics (Figure 52 and Table 25), the original model shows an unfavorable predicted R^2. The difference between the adjusted and predicted R^2 does not provide any insight due to the negative predicted R^2, as was the case for the predicted R^2 values of Ti-6-4 and Beta 21S for the original cubic model. There is a slight improvement in the normal plot. Therefore, the terms are removed.

The modified quadratic and cubic responses can be compared. The graphs of the measured versus the predicted porosity are shown in Figures 21, 22, and 23 for Ti-6-4, Beta 21S and Ti-5-5-5-3, respectively. For all cases, the data points in the cubic models tend to cluster around the 45° line more than those of the quadratic response. This

indicates that the cubic model is a more accurate representation of the measured data obtained and is, therefore, used to predict the porosity of Ti-6-4, Beta 21S and Ti-5-5-5-3.
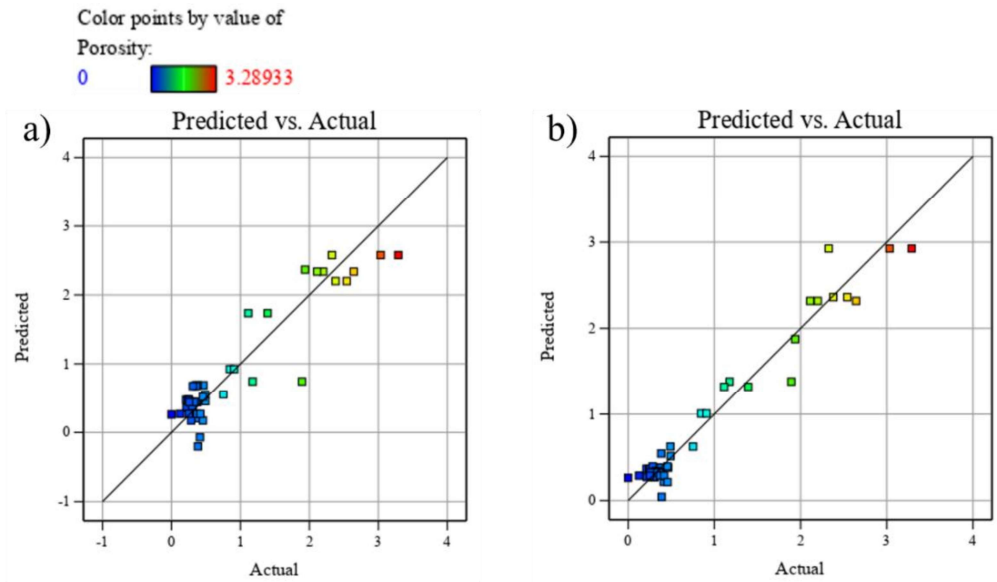
Figure 21: The predicted vs actual porosity of the modified (a) quadratic and (b) cubic responses of Ti-6-4
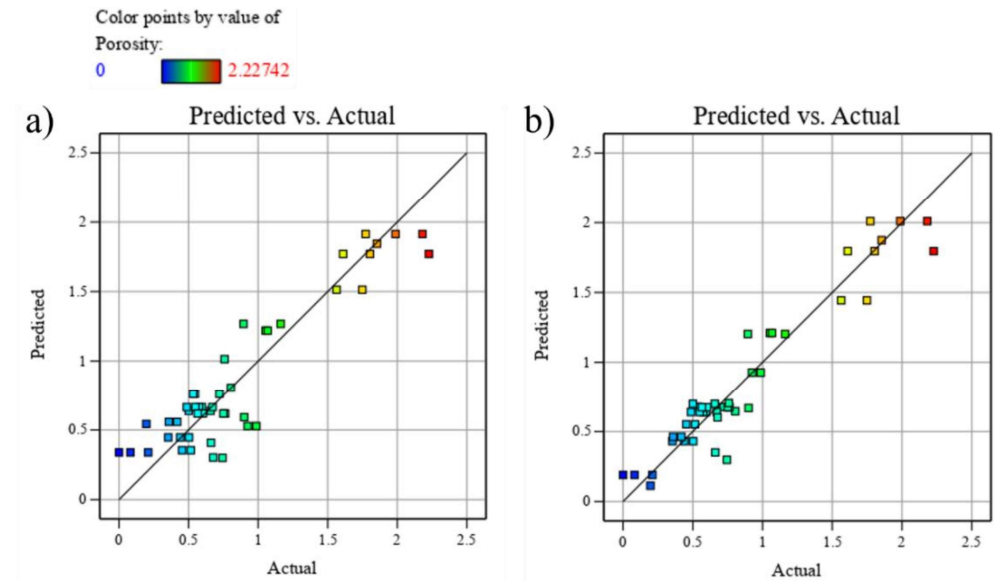
Figure 22: The predicted vs actual porosity of the modified (a) quadratic and (b) cubic responses of Beta 21S

55
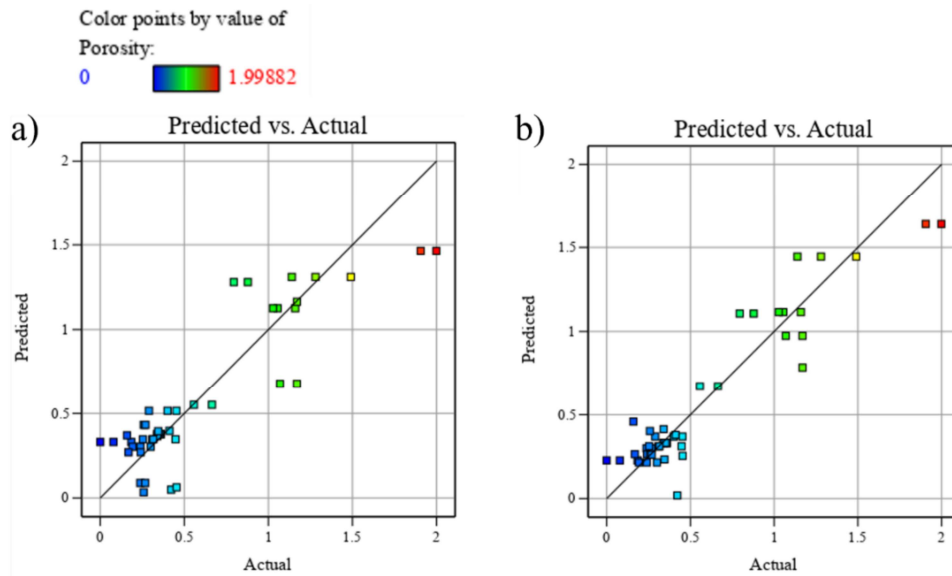
Figure 23: The predicted vs actual porosity of the modified (a) quadratic and (b) cubic responses of Ti-5-5-5-3

5.4.2 Model Equations

To compare the models of each alloy effectively, each model needs to contain the same terms. Fortunately, most terms are shared with minor discrepancies. Table 26 summarises the terms included in the modified models of each alloy and the resulting equation which accommodates the significant terms of all.

Table 26: Resultant Model Terms

Term	Ti-6-4	Beta 21S	Ti-5-5-5-3	Resultant Model
A	✓	✓	✓	✓
B	✓	✓	✓	✓
C	✓	✓	✓	✓
AB	✓	✓	✓	✓
AC	✓	✓	✓	✓
BC	✓	✓	✓	✓
A^2	✓	✓	✓	✓
B^2	✓	✓	✓	✓
C^2	✓	✓	✓	✓
ABC	✗	✗	✗	✗
A^2B	✗	✓	✗	✓
A^2C	✓	✓	✓	✓

56

Term	Ti-6-4	Beta 21S	Ti-5-5-5-3	Resultant Model
AB^2	✗	✗	✗	✗
AC^2	✓	✗	✓	✓
B^2C	✓	✗	✓	✓
BC^2	✗	✗	✗	✗
A^3	✗	✗	✗	✗
B^3	✗	✗	✗	✗
C^3	✓	✓	✓	✓

The model equations with the corresponding coefficients for Ti-6-4, Beta 21S and Ti-5-5-5-3 are reported in Table 27.

Table 27: Response Equations of Ti-6-4, Beta 21S and Ti-5-5-5-3

Porosity [%] =	Ti-6-4	Beta 21S	Ti-5-5-5-3
Intercept [%]	+9.93812	+4.65315	+5.66916
A [W]	+0.046740	+0.024273	+0.033180
B [mm/s]	-0.000542	+0.000783	+0.000498
C [mm]	-551.41208	-278.91998	-344.74720
A × B	-0.000019	-0.000018	-0.000013
A × C	-0.271944	-0.083828	-0.164757
B × C	+0.000846	+0.002028	-0.011951
A²	-0.000088	-0.000039	-0.000064
B²	$+7.87890 \times 10^{-7}$	$+4.41624 \times 10^{-7}$	$+2.50592 \times 10^{-7}$
C²	+7984.24868	+4036.10611	+5126.66448
A² × B	$+1.60975 \times 10^{-8}$	$+2.22035 \times 10^{-8}$	$+1.86801 \times 10^{-8}$
A² × C	+0.001235	+0.000480	+0.000589
A × C²	-2.89246	-1.48272	-1.11212
B² × C	$+6.65456 \times 10^{-6}$	$+3.21138 \times 10^{-6}$	$+6.44168 \times 10^{-6}$
C³	-31054.24426	-15719.62145	-20791.24930

Design Expert provides a coded form of the equation in which the coefficients are normalized. The coded response represents the unit change in porosity as a function of each normalized term. The software by default performs regression computations using the coded scale where the low setting for each factor is set to -1 and the high set to +1. The coded scale is calculated using Equation 6.

$$Coefficient = \frac{2 \cdot (Actual\ setting\ -\ Average\ actual\ setting)}{Range\ between\ low\ and\ high\ actual\ settings} \quad (6)$$

For example, if a factor has a low setting of 30 W and a high setting of 50 W, the average is 40 W, and the range is 20 W. If the value 35 W is used in a run, the coded value is −0.5. The coefficient represents the change in the response as the factor level is changed by one coded unit.

Therefore, the coded equation can be used to identify the relative impact of terms by comparing the factor coefficients. The coded coefficients for each alloy are represented graphically in Figure 24 to visually observe the influence of each term. The terms are grouped according to which parameter takes precedence, i.e., laser power, scan speed, and hatch spacing. Recalling that A, B, and C denote laser power, scan speed, and hatch spacing, respectively.

Group A has the least variation among terms for the respective alloys, while groups B and C vary significantly. In group B, B^2 has the strongest influence for all alloys. C and C^3 in group C both have the strongest influence on T-6-4 and Ti-5-5-5-3, but are the least influential terms for Beta 21S, the strongest being C^2. That being said, the terms with the most influence in group C are additionally the most influential out of every term.

These findings would suggest that hatch distance and scan speed have the highest influence on porosity. However, while the coded coefficients suggest a strong influence caused by hatch distance and scan speed, laser power seems to have a consistent influence throughout. Depending on the energy input, sufficient power may be enough to form an adequate melt pool despite high scan speeds and, consequently, short interaction times. Although, without sufficient overlap between layers and tracks, porosity is still a concern. This would explain the great influence the term A^2C has on porosity. It has a directly proportional relationship with porosity, in which high power would require a large hatch distance to avoid over melting and, consequently, keyholing.

In contrast, the influence of the term B^2C is consistently low for all alloys. An increase in both the hatch spacing and scan speed would adversely affect porosity. The higher the scan speed, the shorter the interaction time between the laser and the powder bed, which could result in an adequate melt pool should the laser power not be high enough to cause a sufficient amount of energy per unit volume. Furthermore, should the hatch spacing be too large, poor overlap could cause lack-of-fusion. However, it is very clear that complex interactions occur between the parameters and the resulting porosity.
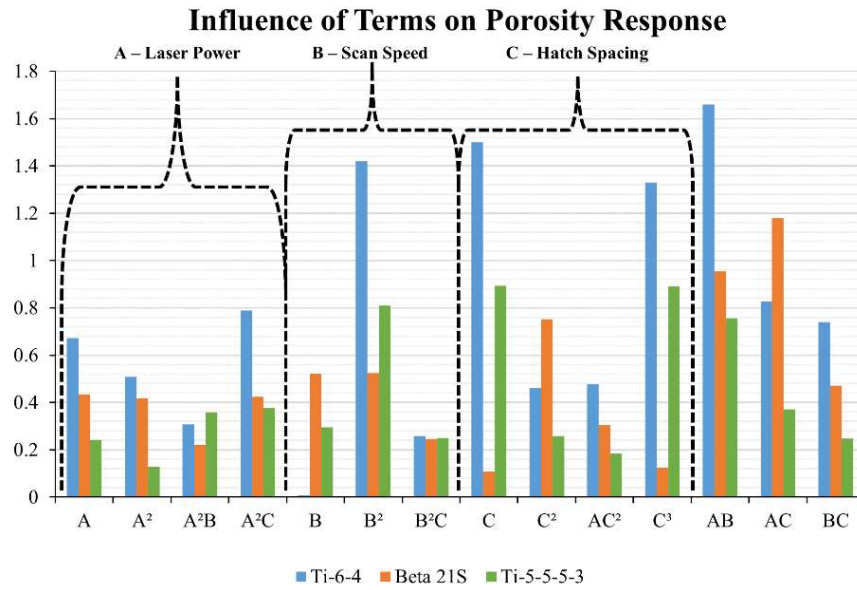
Figure 24: A bar chart illustrating the influence of each term in the modified cubic responses of Ti-6-4, Beta 21S and Ti-5-5-5-3

5.5 Pore Analysis

As discussed previously, pores can vary significantly in size and shape as a result of varying printing conditions. The overall quality of a part depends on the quality of the track. Various different phenomena occur depending on the combination of process parameters and resulting *VED*, which affect the quality of the track and result in distinguishable pore geometries. According to Figure 8 – a processing window established by Promoppatum, Onler, and Yao (2017) for Ti-6-4 – three regions point out over melting, incomplete melting, and balling effects. Therefore, various samples were selected from the collected data to identify these regions and confirm any coherence between the Ti-6-4 processing window and the alloys investigated in this study.

The range of *VED* used was divided into four levels: low, medium-low, medium-high and high. This is noted in Table 28.

Table 28: VED Levels

VED Level	VED Range [J/mm^3]
Low	30 – 90
Medium-Low	91 - 140
Medium-High	141 – 200
High	201 – 250

Of the 50 samples, 4 were selected based on the *VED* level and porosity to confirm the aforementioned regions by analyzing the pores associated with each. Unfortunately, samples within the medium-high *VED* range were not analyzed because none demonstrated significantly high porosity. Micrographs taken of the said samples did not provide enough insight into the mode of pore formation. The following samples were selected for both Beta 21S and Ti-5-5-5-3, as seen in Table 29.

Table 29: Porosity Results of Samples Chosen for Porosity Analysis

Sample No.	VED Level	VED Value [J/mm³]	Beta 21S Scaled Porosity [%]	Ti-5-5-5-3 Scaled Porosity [%]
21 (248-2500-110)	Low	30	1.804	1.055
36 (80-808-110)	Low	30	1.987	1.280
6 (120-400-110)	Medium-Low	91	1.749	1.906
18 (197-657-40)	High	250	0.924	1.070

The results reported in Table 29 are shown graphically in Figure 25. The pores of each sample were subsequently analyzed within their respective *VED* levels to identify the mode of pore formation according to the phenomena mentioned previously.
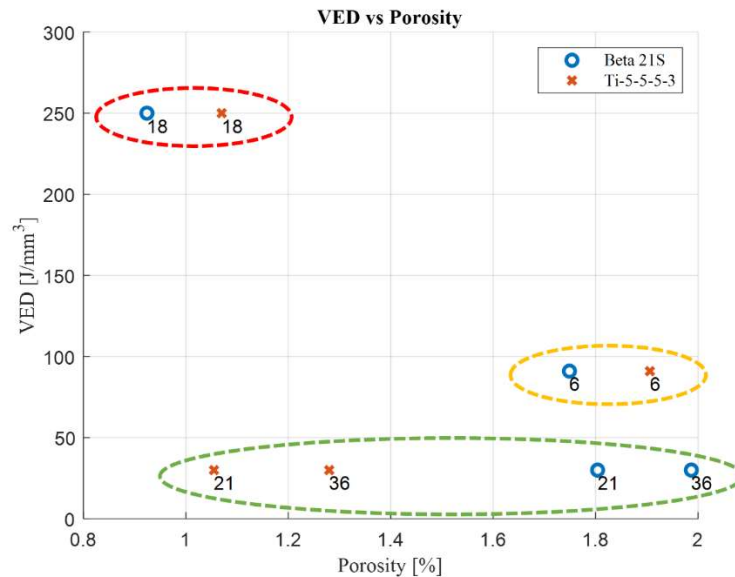
Figure 25: A plot of VED versus porosity grouped according to high, medium-low and low VED levels

The large spherical pores are clearly identified in the micrographs taken of Beta 21S and Ti-5-5-5-3 shown in Figure 26. The presence of these pores indicates that the high

60

energy input is likely responsible for the vaporization of one or more metal constituents, thus resulting in the keyholing effect.
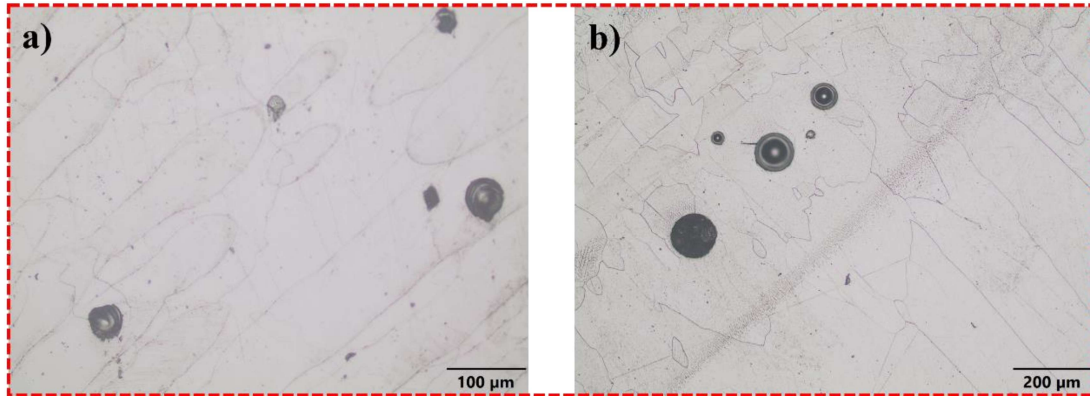
Figure 26: Micrographs of spherical pores in a) Beta 21S and b) Ti-5-5-5-3 samples produced with a high VED

The samples printed using a medium-low *VED* show the presence of spherical pores (Figure 27). Although smaller in size and less spherical in shape than those seen in Figure 26, the keyholing effect is observed. As shown in Figure 27 a), pores occur clearly at the base of the melt pool in Beta 21S, a clear indication of the keyholing effect.
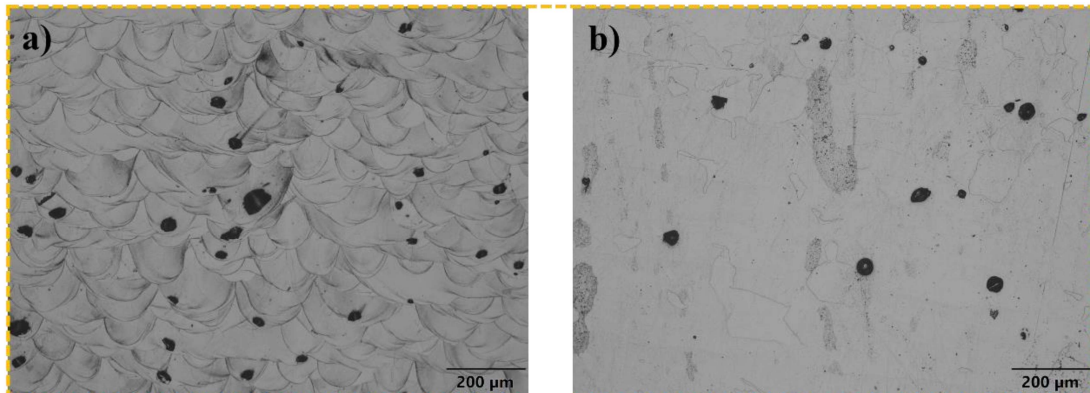
Figure 27: Micrographs of relatively spherical pores in a) Beta 21S and b) Ti-5-5-5-3 samples produced with a medium-low VED

Upon analyzing samples within the low *VED* range, the presence of incomplete melting is clear from the micrographs shown in Figure 28. Lack-of-fusion is apparent on the basis of the irregularly shaped pores which are likely the result of insufficient overlap between layers and tracks due to the low *VED* and large hatch spacing, respectively.
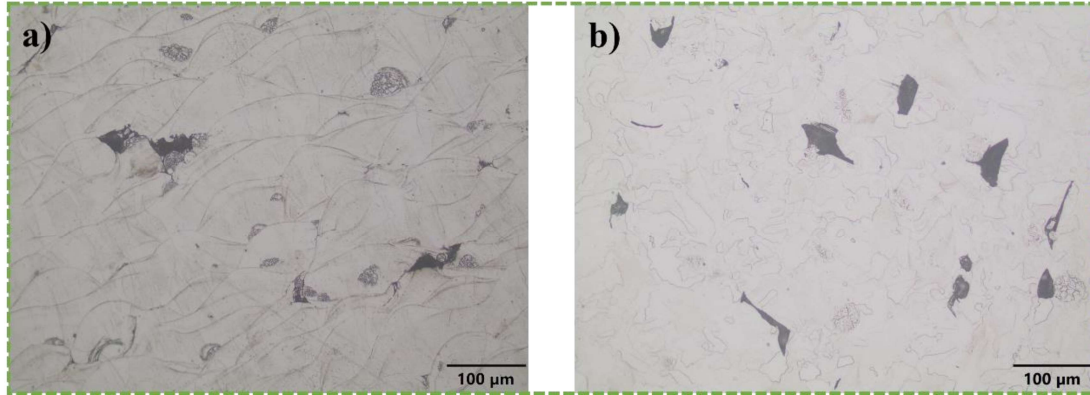
Figure 28: Micrographs of irregularly shaped pores in a) Beta 21S and b) Ti-5-5-5-3 samples produced with a low VED

Finally, the balling effect is considered. According to Yadroitsev et al. (2010), as mentioned previously, this effect occurs when the *VED* is low and the scan speeds are relatively high. The micrographs shown in Figure 29 were taken on Beta 21S and Ti-5-5-5-3 samples with a parameter set of 248-2500-110, using a high scan speed. The micrographs clearly indicate the presence of balling within irregularly shaped pores. These pores, while indicating balling, also demonstrate lack-of-fusion as a result of the large hatch spacing (110 μm) and low *VED*. The incomplete junction of the material causes cavities of unmelted powder, evidently noted in Figure 29.
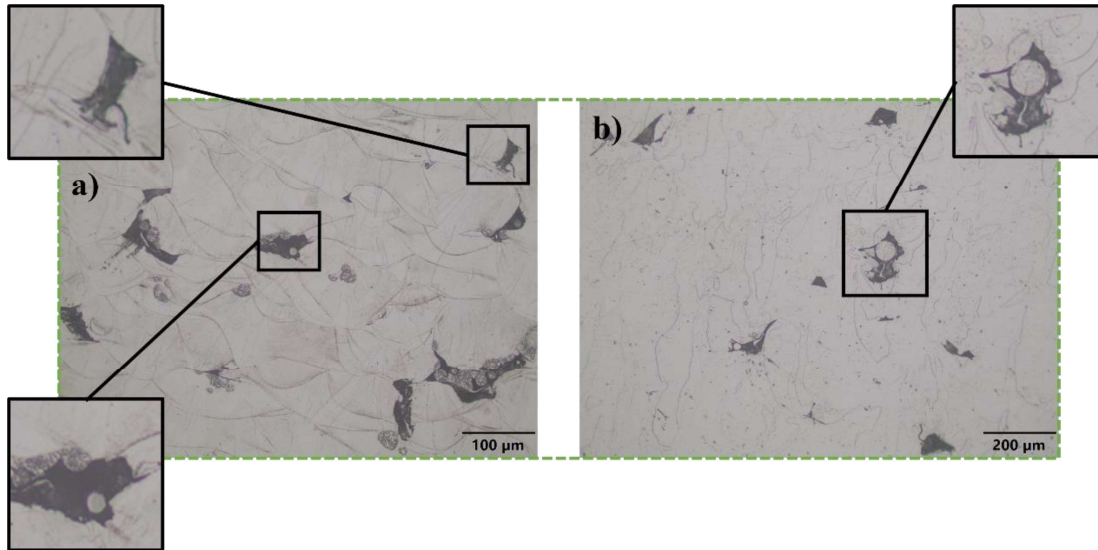
Figure 29: Micrographs of irregularly shaped pores showing signs of balling in a) Beta 21S and b) Ti-5-5-5-3 samples produced with a low VED

62

What is interesting to note is the relatively large difference in porosity between alloys at low VED levels when compared to the difference seen at the medium and low VED values. It appears the materials are more susceptible to such differences where perhaps the energy required to sufficiently melt the material is close to the threshold for the minimum amount of energy required to melt a track capable of overlapping with subsequent tracks. This would explain the differences seen between Beta 21S and Ti-5-5-5-3. Beta 21S is significantly more porous than Ti-5-5-5-3 at lower VED than at the higher VED values. Beta 21S has a higher melting temperature and would thus require more energy to melt the tracks to achieve sufficient overlap (Table 38).

5.6 Hardness Results

The hardness results reported were taken on various samples meeting the density criterion (>99 %) as a precursor for the parameter selection of tensile samples.

The samples upon which the hardness test was performed were selected within each *VED* range defined previously, viz. low, medium-low, medium-high, and high *VED*. The results for Beta 21S and Ti-5-5-5-3 are shown in Tables 30 and 31, respectively. Scatter plots of each graph are shown subsequently to provide a visual representation of the data and insight into parameters which potentially influence the hardness found.

Table 30: Vickers Hardness Readings of Beta 21S at Varying Levels of VED

Sample No.	VED Level	VED Value [J/mm^3]	Hardness [HV] Lateral Plane	Hardness [HV] Longitudinal Plane
6 (120-400-110)	Medium-Low	91	255 ± 10	268 ± 4
15 (248-2500-40)	Medium-Low	83	276 ± 6	280 ± 5
16 (350-1167-40	High	250	304 ± 10	309 ± 7
18 (197-657-40)	High	250	305 ± 7	297 ± 8
21 (248-2500-110)	Low	30	238 ± 15	247 ± 10
24 (80-808-40)	Medium-Low	83	277 ± 6	284 ± 5
27 (350-1167-40)	High	250	299 ± 9	305 ± 6
29 (274-913-60)	Medium-High	167	287 ± 3	293 ± 6
35 (183-609-110)	Medium-Low	91	262 ± 18	277 ± 10
36 (80-808-110)	Low	30	244 ± 14	245 ± 13
37 (248-2500-70)	Low	47	266 ± 8	277 ± 5
40 (205-1296-80)	Low	66	270 ± 5	272 ± 6
41 (197-657-40)	High	250	298 ± 13	302 ± 13
45 (80-400-40)	Medium-High	167	282 ± 6	290 ± 5
48 (350-1167-110)	Medium-Low	91	278 ± 6	286 ± 10

Table 31: Vickers Hardness Readings of Ti-5-5-5-3 at Varying Levels of VED

Sample No.	VED Level	VED Value [J/mm³]	Hardness [HV] Lateral Plane	Hardness [HV] Longitudinal Plane
6 (120-400-110)	Medium-Low	91	269 ± 12	267 ± 26
15 (248-2500-40)	Medium-Low	83	271 ± 8	277 ± 4
16 (350-1167-40	High	250	327 ± 29	376 ± 29
18 (197-657-40)	High	250	319 ± 7	351 ± 38
21 (248-2500-110)	Low	30	262 ± 13	268 ± 7
24 (80-808-40)	Medium-Low	83	272 ± 6	280 ± 4
27 (350-1167-40)	High	250	334 ± 25	365 ± 46
29 (274-913-60)	Medium-High	167	302 ± 3	307 ± 5
35 (183-609-110)	Medium-Low	91	263 ± 22	288 ± 9
36 (80-808-110)	Low	30	250 ± 26	263 ± 12
37 (248-2500-70)	Low	47	276 ± 8	278 ± 5
40 (205-1296-80)	Low	66	273 ± 8	280 ± 7
41 (197-657-40)	High	250	304 ± 46	354 ± 42
45 (80-400-40)	Medium-High	167	297 ± 9	308 ± 9
48 (350-1167-110)	Medium-Low	91	282 ± 6	292 ± 4

Significant scatter is observed for the relationships of scan speed and laser power with hardness. These scatter plots are found in Appendix D: Tensile Sample and Property Information in Figures 55 and 56. The relationships of interest are hatch spacing and *VED*, which have a clearer relationship with hardness. From Figure 30, there seems to be an inversely proportional relationship between hardness and hatch spacing. This could potentially be due to the insufficient track overlap resulting in increased porosity. According to Li et al. (2019), increased porosity causes a decrease in hardness. Brown et al. (2014) also report this behavior and can be explained by pores collapsing under load, resulting in a decrease in hardness.

64
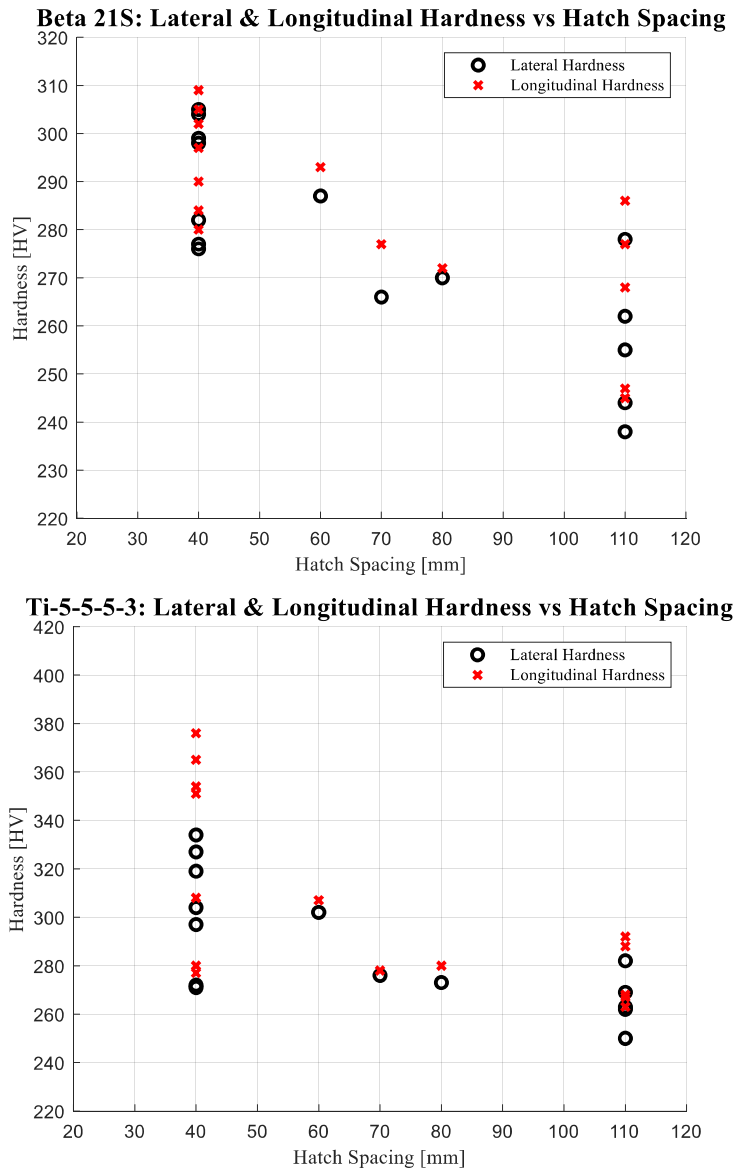
Figure 30: A visual representation of the relationship between lateral/longitudinal hardness and hatch spacing for Beta 21S and Ti-5-5-5-3

Moreover, a directly proportional relationship is found between hardness and *VED*. This is likely due to the aforementioned relationship between hardness and hatch spacing. A decrease in hatch spacing results in an increase in *VED*, thus explaining the relationship seen in Figure 31.

65
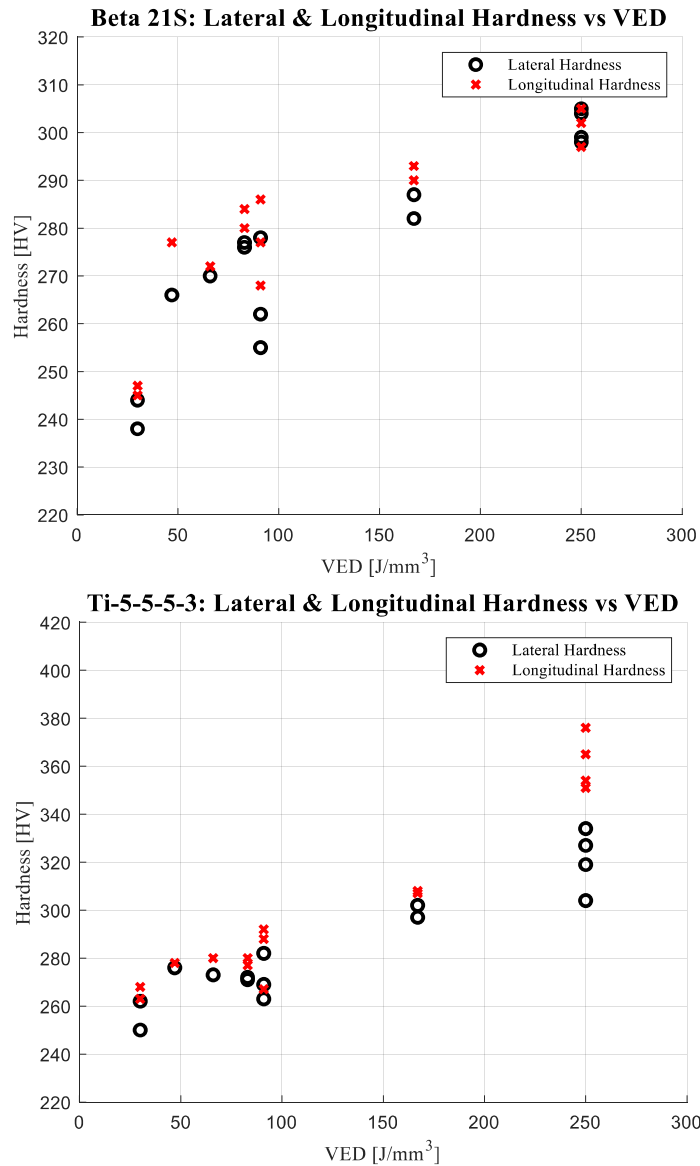
Figure 31: A visual representation of the relationship between lateral/longitudinal hardness and VED for Beta 21S and Ti-5-5-5-3

The parameters for the tensile samples were selected based on the hardness results shown in Tables 30 and 31, but it is important to confirm if this is what was exhibited in the printed tensile samples. Segments of the tensile samples were cut and analyzed. The hardness results for Beta 21S and Ti-5-5-5-3 can be seen in Tables 32 and 33, respectively.

Table 32: Beta 21S Tensile-Sample Hardness-Readings

66

Sample No.	Hardness [HV] Lateral Plane	Hardness [HV] Longitudinal Plane
T1 [**27** (350-1167-40)]	289 ± 5	288 ± 5
T2 [**45** (80-400-40)]	293 ± 5	284 ± 14
T3 [**37** (248-2500-70)]	280 ± 16	288 ± 6

Table 33: Ti-5-5-5-3 Tensile-Sample Hardness-Readings

Sample No.	Hardness [HV] Lateral Plane	Hardness [HV] Longitudinal Plane
T1 [**27** (350-1167-40)]	296 ± 9	293 ± 8
T2 [**45** (80-400-40)]	290 ± 9	301 ± 7
T3 [**37** (248-2500-70)]	Fail	

While the Beta 21S results seem to correlate, there are discrepancies between the Ti-5-5-5-3 results reported for the model samples and those reported for the tensile sample T1. The hardness values for the tensile results are ~11 and 20 % lower than previously reported for the lateral and longitudinal planes, respectively. With shorter scan tracks, as would be found for the model samples, come lower thermal gradients as a result of the reduced intervals between tracks. This influences the residual stress, which in turn affects the hardness. The degree to which this occurs should be considered for future study because residual stress may cause cracks and affect the density of components. Unfortunately, the Ti-5-5-5-3 T3 samples printed with a low *VED* failed during the build and no data on the hardness is available at present.

5.7 Tensile Results

Herein lie the tensile results for Beta 21S and Ti-5-5-5-3. Each subsection reports the respective mean σ_Y, σ_T, Young's modulus, e_f, and reduction in area. The stress-strain curves can be found in Figures 57, 58, 59, 60, and 61 in Appendix D: Tensile Sample and Property Information and are not reported in this section due to the lack of available space.

5.7.1 Tensile Properties of Beta 21S

Recalling the low, medium, and high *VED*s with which the tensile samples were printed. The mean tensile properties of each *VED* level are reported in Table 34.

Table 34: Tensile Properties Recorded for Beta 21S

Tensile Properties

VED Level	Yield Strength (Offset = 0.2%), σ_Y [MPa]	Ultimate Tensile Strength, σ_T [MPa]	Young's Modulus, E [MPa]	Elongation to Failure (25.4 mm Gauge Length), e_f [%]	Reduction in Area, RA [%]	Porosity [%]
High	877 ± 7	885 ± 4	77.2 ± 1.4	23.2 ± 1.4	42.8 ± 10.2	0.177
Medium	918 ± 2	928 ± 2	79.2 ± 0.3	24.5 ± 0.9	50.2 ± 5.5	0.673
Low	917 ± 17	938 ± 13	75.2 ± 1.4	23.6 ± 2.3	43.4 ± 6.2	1.526

Tensile samples printed with medium *VED* reported the highest σ_Y, Young's modulus, e_f, and reduction in area, while the low-VED sample group reported the highest σ_T. The samples within the high-VED group reported the lowest of all mechanical properties.

All sets of parameters were chosen based on the fact that the model samples met the density criterion (>99 %). However, the tensile samples printed with a low *VED* demonstrate significant porosity. This is likely due to the larger scan vectors used in the tensile samples, resulting in lower thermal gradients. Interesting to note is the tensile strength reported despite the porosity discrepancy. The ability to demonstrate relatively high mechanical properties despite the reduction in porosity is likely due to the ductile behavior seen, which makes the material capable of withstanding substantial plastic deformation before failure.

5.7.2   Tensile Properties of Ti-5-5-5-3

The mean tensile properties of each *VED* level are reported in Table 35. As previously mentioned, the sample T3 (low *VED*) failed during the print. Therefore, mechanical properties for T3 are not available at present.

Table 35: Tensile Properties Recorded for Ti-5-5-5-3

VED Level	Tensile Properties					
	Yield Strength (Offset = 0.2%), σ_Y [MPa]	Ultimate Tensile Strength, σ_T [MPa]	Young's Modulus, E [MPa]	Elongation to Failure (25.4 mm Gauge Length), e_f [%]	Reduction in Area, RA [%]	Porosity [%]
High	763 ± 11	774 ± 14	73.3 ± 1.0	11.4 ± 0.4	5.67 ± 0.71	0.093
Medium	856 ± 7	860 ± 7	77.6 ± 0.9	21.1 ± 1.5	28.1 ± 4.8	0.402
Low	Fail					

Similarly to Beta 21S, the mean properties improved when using medium *VED* compared to the properties reported for the high VED samples. The σ_Y and σ_T of

samples printed with a medium *VED* show an approximate increase of 90 MPa compared to those printed with a high *VED*. The e_f more or less doubles, while the reduction in area improves by approximately a factor of 5. This indicates a significant improvement in ductility. Higher *VED* levels are suspected to facilitate the formation of α-precipitates, thus resulting in a decrease in ductility.

5.8 Model Verification

To verify the model, several model samples were printed according to random parameter combinations that fall within the design space. The samples were then analyzed using methods outlined in Section 4.3 to verify whether the model gives accurate predictions of the density or not.

The parameter combinations were selected with varying *VED* values as can be seen in Tables 36 and 37 along with the measured densities and associated porosity.

Table 36: Density Results of Model Verification Samples selected for Beta 21S

Sample No.	VED Level	VED Value [J/mm³]	Calculated Density [g/cc]	Observed Porosity [%]	Predicted Porosity [%]
V1 (329-1737-54)	Medium-Low	117	4.94	0.038	0.162
V2 (233-2050-64)	Low	59	4.89	0.164	0.219
V3 (84-458-44)	Medium-Low	139	4.81	0.609	0.118
V4 (202-1111-61)	Medium-Low	99	4.93	0.706	0.210
V5 (106-541-46)	Medium-High	142	4.92	0.067	0.224

Table 37: Density Results of Model Verification Samples selected for Ti-5-5-5-3

Sample No.	VED Level	VED Value [J/mm³]	Calculated Density [g/cc]	Observed Porosity [%]	Predicted Porosity [%]
V1 (326-1357-67)	Medium-Low	120	4.68	0.243	0.103
V2 (221-1870-71)	Low	55	4.65	0.413	0.173
V3 (83-504-44)	Medium-Low	125	4.61	1.07	0.938
V4 (95-722-44)	Medium-Low	95	4.67	0.202	0.058
V5 (345-1516-54)	Medium-Low	140	4.72	0.156	0.121

The model accounts for a 0.25% variation. From the results reported, it can be seen that the reported values are more or less within range.

6. DISCUSSION

This chapter discusses the findings of this research and aims to draw conclusions from the processing windows established for Ti-6-4, Beta 21S, Ti-5-5-5-3. Additionally, connections are made between the determined properties and microstructure. The influence of process parameters is also taken into account. Finally, recommendations are made for property improvements and future work.

6.1 Processing Window

This section outlines the processing windows established based on the extrapolated data and the resulting response surfaces generated by the *Design-Expert* software.

6.1.1   Ti-6-4 Model Verification

Ti-6-4 is used as the baseline for this study to evaluate the effectiveness of using D-optimality to develop a processing window for Beta 21S and Ti-5-5-5-3. A study by Wang et al. (2019) sought to optimize the relative density of Ti-6-4 in which hatch spacing and layer thickness were kept constant at 100 μm and 30 μm, respectively. The spot size used was 90 μm. The scan speed and laser power were varied according to Figure 32 in that porosities of less than 1 % were reported for samples within the red-dotted area.
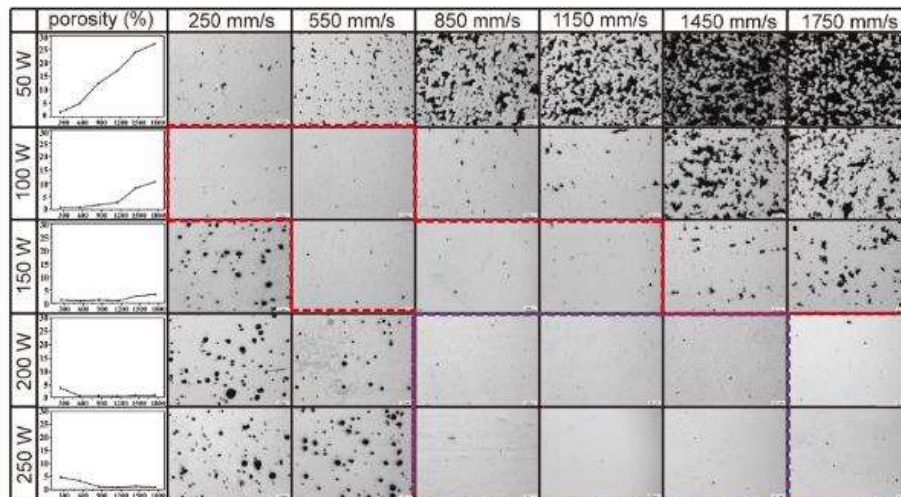
Figure 32: Porosity distribution of LPBF-produced Ti-6-4 as reported by Wang et al. (2019)

Since a similar scan strategy was used in this study – 60° scan rotation – and both the hatch spacing and layer thickness coincide with the design constraints set out, the combinations of scan speed and laser power within the red-dotted area ranging 550 –

70

1750 mm/s and 100 – 250 W, respectively, are implemented in the model. Some discrepancies are expected due to the difference in spot size. The points are shown Figure 33. The dashed lines indicate VED levels. Contour lines indicate percent porosity.
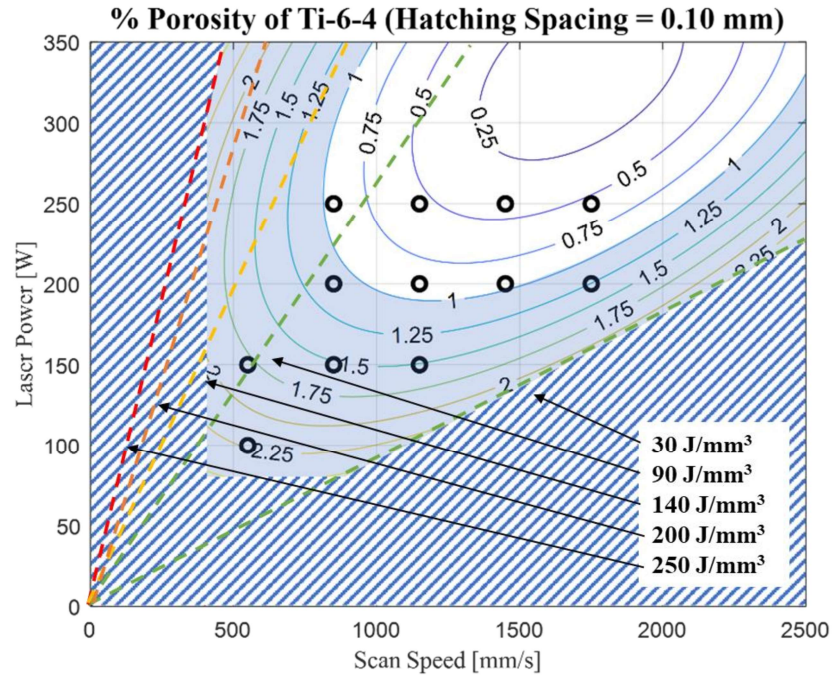
Figure 33: Processing window of Ti-6-4 at a constant hatch spacing of 100 μm showing points in which samples were determined to have a density of greater than 99% by Wang et al. (2019)

Despite the discrepancies between spot size diameter and perhaps other machine parameters, the model provides a valid processing window with which to extract parameters to obtain dense components. Results were scaled. Therefore, porosity values are lower than what is reported in the processing window, making the model more conservative in its predictive capabilities.

6.1.2   Ti-6-4 vs Beta 21S vs Ti-5-5-5-3

The porosity response for each alloy is compared herein and shown graphically in Figure 34.
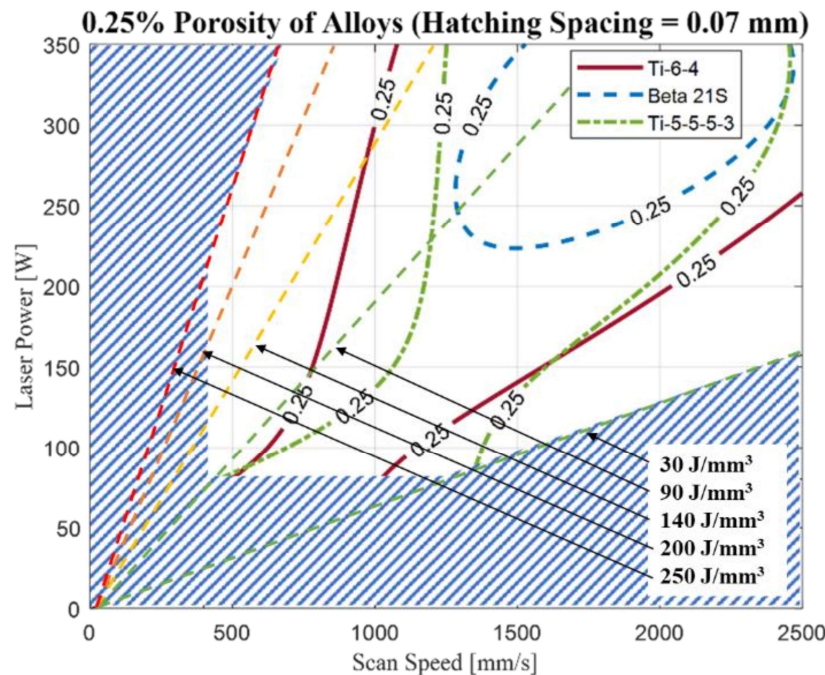
Figure 34: Processing window in which a porosity of 0.25% for Ti-6-4, Beta 21S and Ti-5-5-5-3 at a hatch spacing of 70 μm is predicted

Table 38 reports the melting temperatures of Ti-6-4, Beta 21S, and Ti-5-5-5-3, which are arranged in ascending order according to the minimum melting temperature.

Table 38: Melting Temperatures of Ti-6-4, Beta 21S and Ti-5-5-5-3

	Increasing Melting Temperature →		
	Ti-6-4	**Ti-5-5-5-3**	**Beta 21S**
Melting Temperature [°C]	1604 – 1660 (Boyer, Welsch and Collings, 1994)	1630 ± 5 (Sherov et al., 2022)	1672 – 1747 (Boyer, Welsch and Collings, 1994)

The contour lines in Figure 34 cover regions in which the density of 0.25% is expected for each alloy. What is interesting to note is that the regions between the contour lines decrease in size in the same order as the increase in melting temperature seen in Table 38. With a concomitant increase in laser power and scan speed comes a reduction in porosity. As one moves from the line of lowest *VED* (30 J/mm^3) leftwards, the contour lines of Ti-6-4, Ti-5-5-5-3, and Beta 21S follow in that order. This would imply that more energy is required to melt Beta 21S than Ti-5-5-5-3, and then Ti-6-4. Reducing the laser power along constant lines of *VED* would result in a decrease in melt pool size, thereby increasing the likelihood of porosity should the hatch spacing not be able to compensate for this. With an increase in laser power toward lines of higher *VED*

72

comes an increase in porosity beyond the leftmost bounds of the contour lines. Despite the relatively high melting temperature of Beta 21S, increasing the laser power and reducing the scan speed makes it more susceptible to over melting. Recalling that Beta 21S has the highest thermal conductivity (Table 8) when compared to Ti-5-5-5-3 – 7.5 versus 5.3 J/m°C, respectively – the rate of heat transfer in Beta 21S is thus higher. Due to the continuous reheating of the material during the process, the thermal gradient would cause heat transfer in the direction of subsequently heated layers thus impeding heat dissipation from the material. Therefore, it is likely that Beta 21S has a larger heat-affected zone, which would result in an increase in porosity should the power be increased and the scan speed lowered.

6.1.3 Processing Windows

The processing windows generated for each alloy are seen in Figures 35, 36, and 37 in which the hatch spacing is kept constant at 40, 80, and 110 μm, respectively. The hatched regions define the parameters that do not fall within the design space (Table 10). The blue areas define the combinations of process parameters that do not meet the optimal density criterion (>99 %). The areas expected to show over melting, incomplete melting and balling are labelled. The processing windows include labelled sample points. The accompanying mean porosities are reported in Tables 42, 43, and 44 in Appendix B: Detailed Design Matrix and Porosity Data for Ti-6-4, Beta 21S, and Ti-5-5-5-3, respectively.

From Figures 35, 36, and 37, it can be seen that the general appearance of the processing windows resembles that obtained by Promoppatum, Onler, and Yao (2017). The research carried out by Promoppatum, Onler, and Yao (2017) suggests that lack-of-fusion is likely to occur when the hatch spacing is larger than the laser diameter, which would imply that more energy is required to develop a sufficient melt pool to prevent incomplete melting. This is clearly seen in the processing windows in Figures 35, 36, and 37 as the region of incomplete seems to expand inwards as the hatch spacing increases.

What can be deduced from Figure 35, the region in which over melting is expected decreases from Beta 21S to Ti-5-5-5-3 to Ti-6-4. As was noted previously, the melting temperature for each alloy decreases in that order. Beta 21S thus requires higher laser power – where *VED* is kept constant – to melt material. However, due to the high thermal conductivity of Beta 21S discussed in 6.1.2, this alloy is perhaps more susceptible to over melting should the *VED* be too high. This is based on speculation and further study would need to be done to confirm this. Conversely, Beta 21S has the largest region in which incomplete melting is expected, which can be inferred from the fact that lower levels of laser power are incapable of sufficiently melting the powder material.
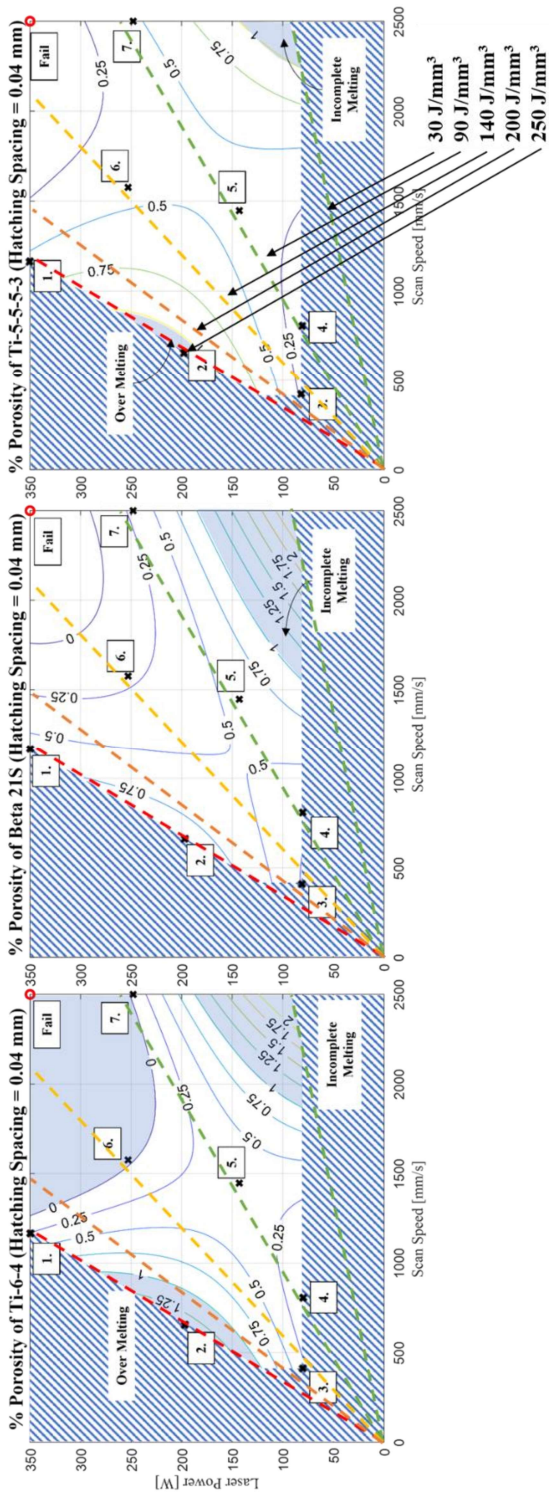
Figure 35: Processing window of Ti-6-4, Beta 21S, and Ti-5-5-5-3 at a constant hatch spacing of 40 µm
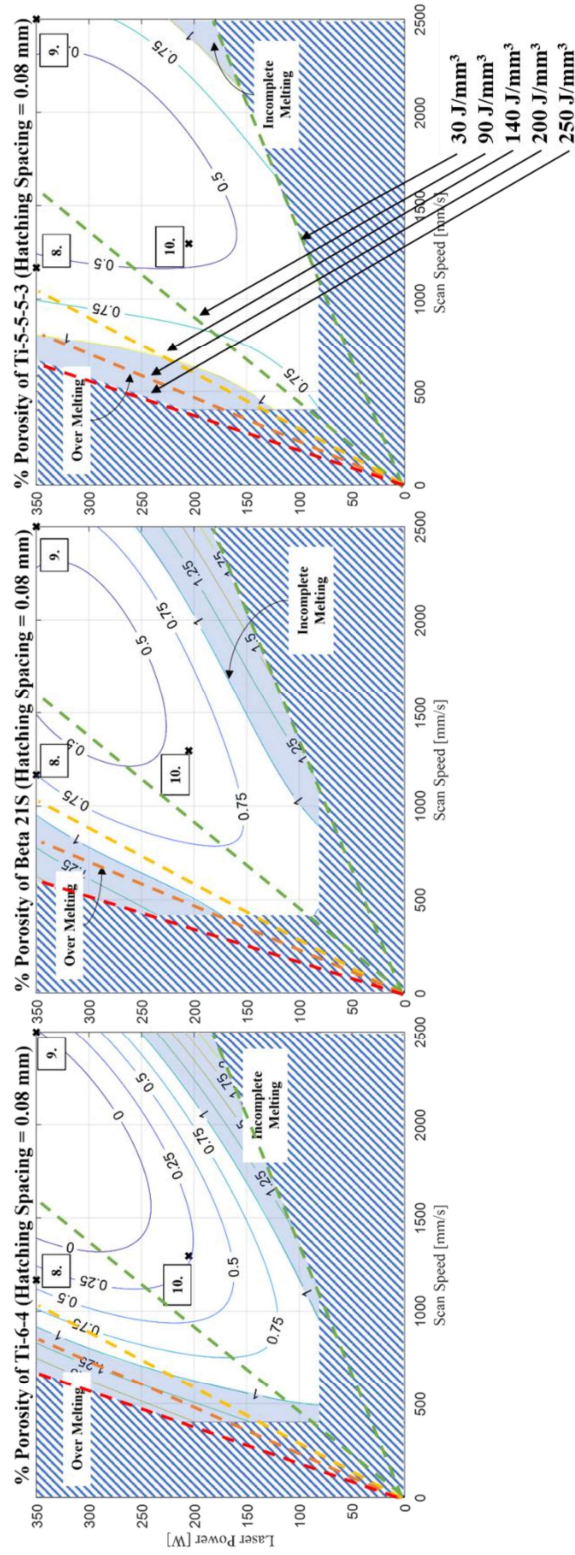
Figure 36: Processing window of Ti-6-4, Beta 21S, and Ti-5-5-5-3 at a constant hatch spacing of 80 µm

74
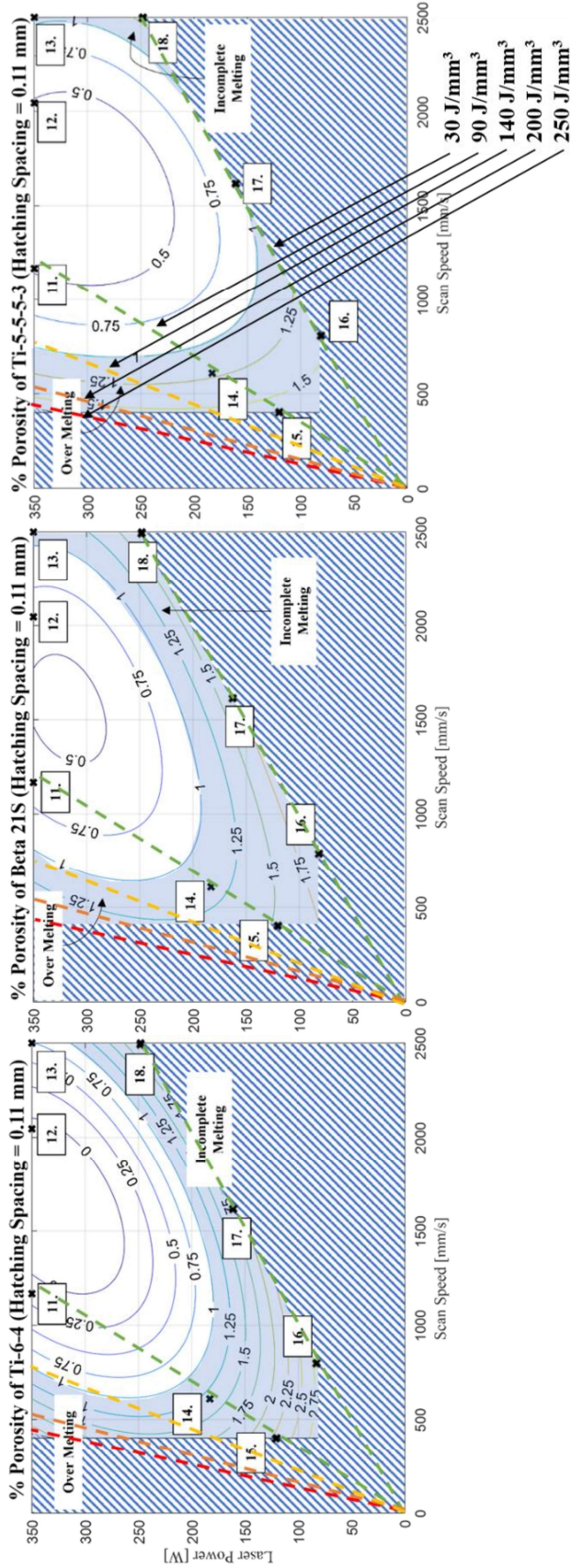
Figure 37: Processing window of Ti-6-4, Beta 21S, and Ti-5-5-5-3 at a constant hatch spacing of 110 μm

The processing windows for Ti-6-4, Beta 21S, and Ti-5-5-5-3 share a similar appearance at a constant hatch spacing of 80 μm as seen in Figure 36. Increasing the hatch spacing from 40 to 80 μm brought about a reduction in the optimal density window. The processing window is reduced further by increasing the hatch spacing to 110 μm. The onset of poor overlap between tracks and subsequent layers is evident because of the significant reduction in size. As such, an increase in laser power is required to compensate for this. However, it is clear from Figure 37 that the processing windows span a similar range of scan speeds provided that the laser power be higher than approximately 140, 175 and 200 W for Ti-5-5-5-3, Ti-6-4 and Beta 21S, respectively.

As reported by Yadroitsev et al. (2010), balling occurs when the melt-pool configuration is such that the length-to-width ratio is greater than π which is expected where the energy density is low and the scanning velocity is high. Regions in which balling normally occurs could not be verified because samples printed with parameters in this region failed due to a disrupted powder bed. However, it is likely that the region in which incomplete melting is usually reported also includes balling due to both insufficient overlap between tracks and layers, and the track irregularities caused by balling. Signs of balling were shown in the pore analysis in Figure 29.

75

6.2 Material Property Correlation

This section seeks to outline correlations between the results found in this study and those previously reported by literature.

6.2.1 Hardness Properties vs Literature

In a study conducted by Macias-Sifuentes et al. (2021), an average microhardness of 278 ± 5 HV was obtained in the as-built condition, which is similar to that of Beta 21S in the supplied condition whereby a solution treatment at 843 °C is employed, followed by air cooling (no aging). Unfortunately, the process parameters used in the study by Macias-Sifuentes et al. (2021) are not stated.

Regarding Ti-5-5-5-3, a study by Ahmed et al. (2022) reported a range of $270 \pm 20 - 288 \pm 1$ HV in which laser power, scan speed, and *VED* ranges of $270 - 330$ W, $1200 - 1400$ mm/s, and $64.3 - 91.7$ J/mm^3 were reported in as-built samples, respectively. When comparing the Vickers microhardness values of Ti-5-5-5-3 reported in Table 31 within the same range of *VED*, a range of $268.9 \pm 12.4 - 281.7 \pm 5.8$ is found. This is very similar to that reported by Ahmed et al. (2022). Zhang et al. (2022) reported similar findings as shown in Table 7.

Before considering the tensile data and its correlation with the literature, it is important to note whether the properties found describe the behavior when loaded in alternate directions. Due to the columnar growth of prior-β grains, anisotropy is expected with titanium LPBF-produced parts. Recalling that to alleviate the effects thereof, the 67° scan rotation was introduced. The lateral and longitudinal dimensions are plotted against one another in Figures 38 and 39 with the solid line showing equal hardness in both directions.
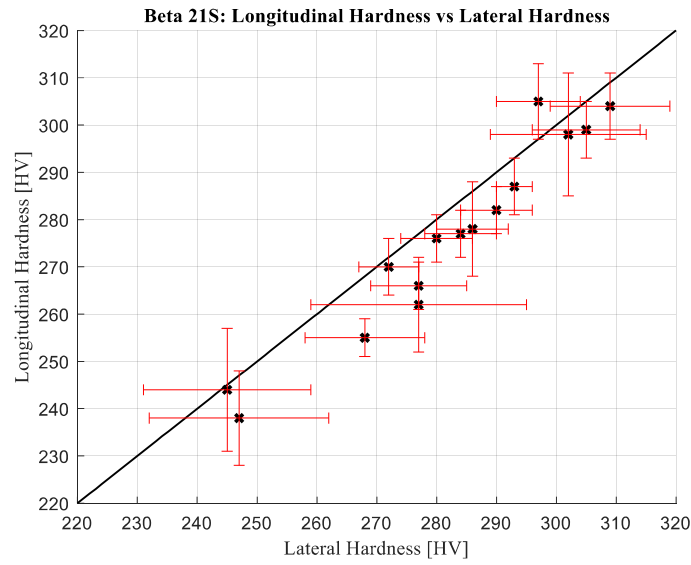
Figure 38: Relationship between mean longitudinal and lateral hardness measurements taken on Beta 21S samples

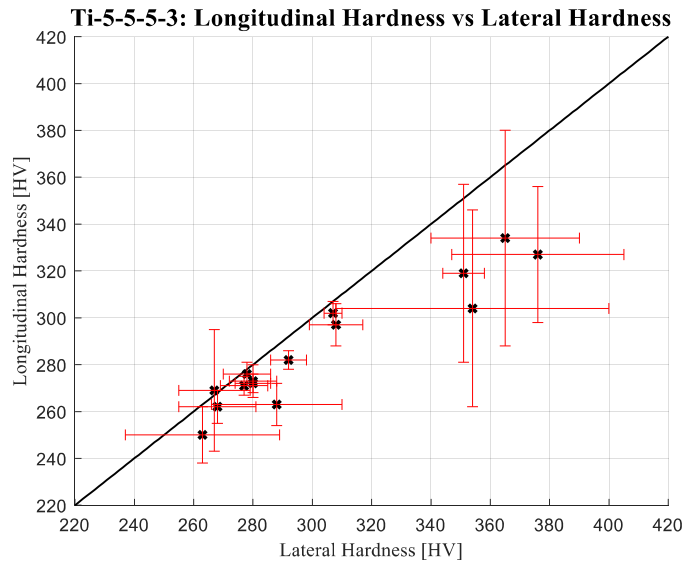*Figure 39: Relationship between mean longitudinal and lateral hardness measurements taken on Ti-5-5-5-3 samples*

It is clear from Figures 38 and 39 that a linear relationship exists between longitudinal and lateral hardness, but not equal. The longitudinal hardness is lower than the lateral hardness for both alloys. The tensile properties reported are a good indication of what

is expected in the transverse plane. Some anisotropy is expected because the data deviates slightly from the 45° line of equal hardness in both directions.

6.2.2 Tensile Properties vs Literature

The as-built properties of Beta 21S presented in the study conducted by Macias-Sifuentes et al. (2021) show a σ_Y of 917 MPa and an σ_T of 946 MPa. Recalling the tensile properties recorded in this study, Beta 21S demonstrated its highest σ_Y of 917 MPa and an σ_T of 938 MPa when printed with a low *VED* of 47 J/mm^3. Furthermore, both this study and that conducted by Macias-Sifuentes et al. (2021) report an e_f of approximately 25%. The ductility reported by Boyer, Welsch, and Collings (1994) for the wrought counterpart in the solution-treated state is significantly lower – more than half of what is reported in this study and by Macias-Sifuentes et al. (2021) (12%). In addition, the σ_Y is reported to be 883 MPa by Boyer, Welsch and Collings (1994) – lower than that reported for the LPBF-produced components. The decrease in e_f and σ_Y demonstrated in wrought components corresponds to the improvement seen in σ_T (931 MPa). Macias-Sifuentes et al. (2021) observed a higher percentage of β-phase in Beta 21S produced by LPBF compared to the wrought alloy. The tensile properties found can be attributed to this. There is a clear correlation between the results obtained and those shown in the literature.

As reported in Table 7, the tensile properties reported for Ti-5-5-5-3 in the literature correlate with those obtained for samples printed with medium *VED* (167 J/mm^3). When comparing these properties with those described by Cotton et al. (2015) for wrought T-5-5-5-3, the σ_Y of 856 MPa reported in this study is superior to that of the wrought counterpart (~800 MPa) when supplied in the solution-treated state. The σ_T, on the other hand, is lower that the wrought value by 20 MPa. Similarly, the respective σ_Y and σ_T of 838 and 885 MPa reported by Zhang et al. (2022) are inferior and superior compared to the values reported in in this study. An increase in ductility typically comes at the expense of σ_T. This is backed by the superior ductility reported in this study. An e_f of 21% shows a significant improvement in ductility compared to the 15 and 7% e_f reported for the wrought and LPBF-produced results noted by Cotton et al. (2015) and Zhang et al. (2022), respectively. The results established for Ti-5-5-5-3 in this study, much like Beta 21S, can be attributed to the high β-phase content. The superior ductility – when compared to the results reported by Zhang et al. (2022) on LPBF-produced components – are likely due to the *VED* of 167 J/mm^3. This applied *VED* is more than twice as high as what was used by Zhang et al. (2022) (69 J/mm^3). It is possible that the high *VED* used facilitated the prolonged growth of β-phase in this near-β alloy by holding the components above the β-transus temperature for longer periods of time. This is also observed by Bakhshivash et al. (2019) when comparing the results obtained from medium and high *VED* builds.

6.3 Microstructure and Heat Treatment Consideration

This section considers the microstructure investigated in conjunction with the properties found to recommend potential heat treatments to improvement properties for end use.

6.3.1 Microstructure of Beta 21S

As discussed previously, the mechanical properties recorded in this study demonstrate a strong correlation with those obtained by Macias-Sifuentes et al. (2021) in which the as-built microstructure and hardness and tensile properties were determined. When consulting the SEM micrographs obtained for the tensile samples reported to show comparable properties, there are distinct similarities between the microstructures obtained.

Although both this study and that conducted by Macias-Sifuentes et al. (2021) utilized a 67° scan rotation, there is still a clear indication of the columnar grain growth, as well as the formation of dendrites. Both SEM micrographs reveal cellular features that grew across the molten pool boundaries. The columnar grain growth can be spotted in Figure 40, outlining the growth across the melt pool boundaries parallel to the build direction.
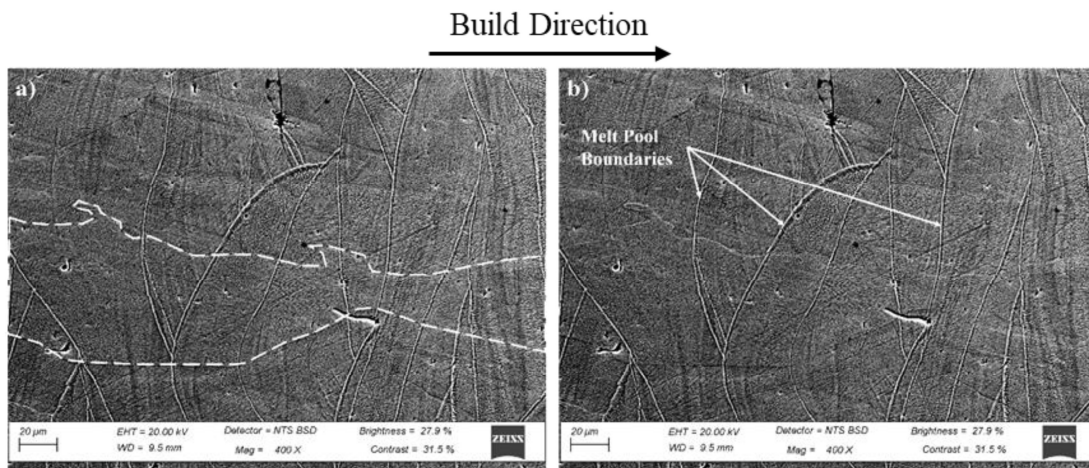
Figure 40: SEM micrograph showing a) the columnar grain growth and b) the melt pool boundaries across which the grains grow for Beta 21S

Furthermore, and what is interesting to note is the presence of columnar dendritic growth in Figure 41. This type of growth is favored where the temperature-gradient-to-growth rate is high (Macias-Sifuentes et al., 2021). High thermal gradients and low growth rates are associated with LPBF and thus facilitate the formation of these structures.
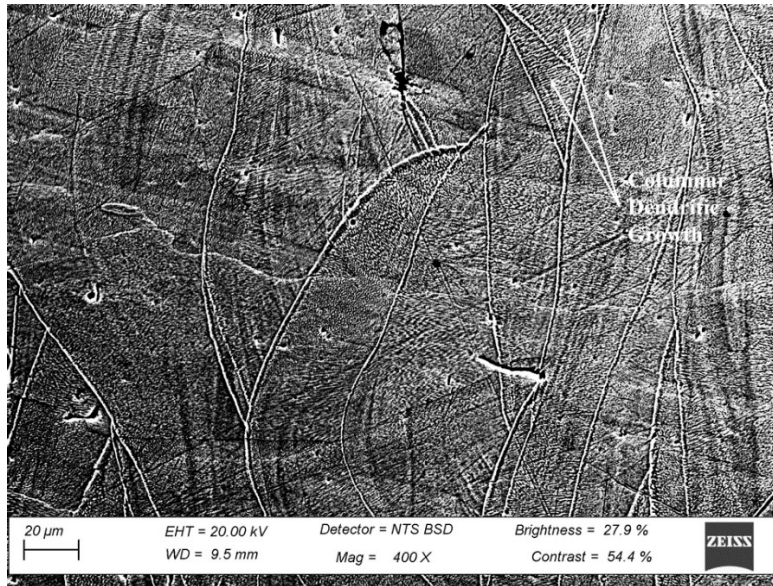
Figure 41: SEM micrograph showing evidence of columnar dendritic growth for Beta 21S

What is interesting to note is the formation of equiaxed dendrites along the boundary of the melt pool, as seen in Figure 42, which may have formed in regions with residual heat. The low thermal gradient may have been enabled by heating the base plate (200 °C), resulting in the growth of such structures.
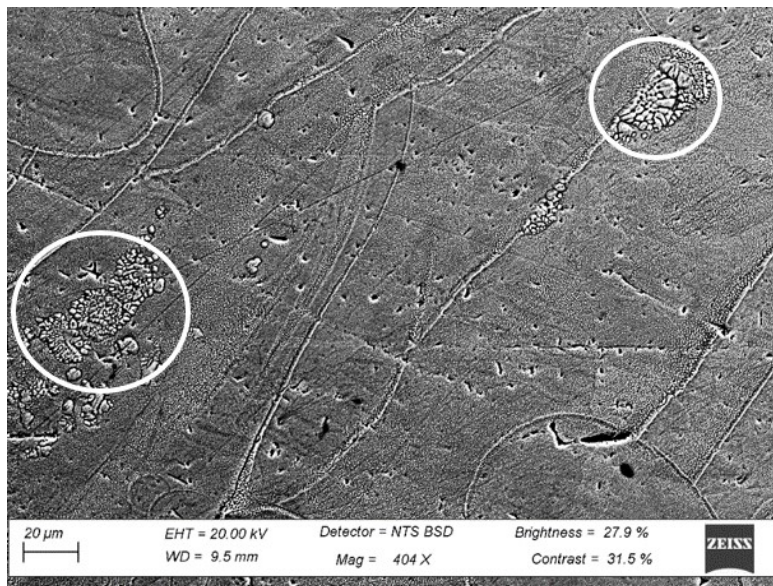
Figure 42: SEM micrograph showing evidence of equiaxed dendritic growth for Beta 21S

80

6.3.2 Heat Treatment Consideration for Beta 21S

According to Boyer, Welsch and Collings (1994), the standard STA treatment for Beta 21S consists of a solution treatment at temperatures above the β-transus temperature (805 °C), followed by air cooling and then aging performed at temperatures above the ω-solvus temperature (350 °C). Finally, this heat treatment is completed with air cooling.

Based on the findings in this study and in conjunction with the mechanical properties and microstructure found by Macias-Sifuentes et al. (2021), it is clear that the results obtained are similar to those found for wrought Beta 21S having undergone ST. This is demonstrated in Figure 43 where a comparison between the σ_Y and the σ_T of wrought and as-built ST and STA-treated Beta 21S is shown as a function of elongation, as reported by Macias-Sifuentes et al. (2021). The results obtained in this study are also shown in Figure 43. The σ_Y and the σ_T are shown on the respective graphs in which the green, orange, and red crosses indicate low, medium, and high *VED*. Should the reader not be able to differentiate the colors, the crosses are labeled with the properties. The labels can be used in conjunction with Table 34 to determine the *VED*.
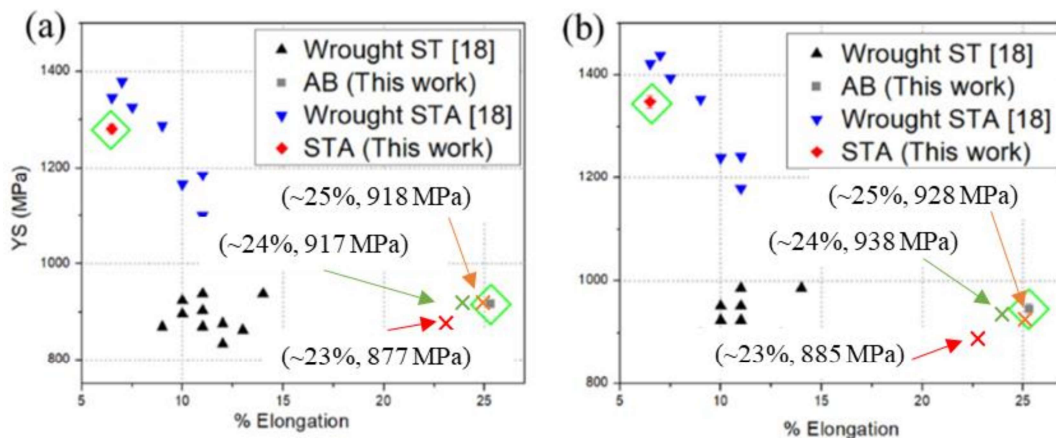
Figure 43: Comparison between wrought and as-built a) yield strength and b) ultimate tensile strength of Beta 21S as a function of elongation at room temperature (Macias-Sifuentes et al., 2021)

In the ST condition, the mechanical properties are in fact competitive with those demonstrated by the wrought counterparts. However, there is a vast improvement in ductility that is attributed to the higher percentage of β-phase found in LPBF-produced Beta 21S (Sing, Yeong, & Wiria, 2016).

Upon performing a Beta 21S aging treatment, a reduction in ductility is caused by the increase in α-phase content – noted in Figure 43. However, the precipitation of α-phase brings about improved mechanical properties and is, thus, the reason Beta 21S is used

in the aged condition. Therefore, based on the comparative results found in this study and those reported by Macias-Sifuentes et al. (2021), it is suggested that an aging treatment – much like what is described – be performed to improve the tensile properties. The aging duration can be varied to assess the hardenability of Beta 21S.

6.3.3   Microstructure of Ti-5-5-5-3

The SEM analysis performed on the Ti-5-5-5-3 tensile samples reveals cellular grain structures in which the presence of α-phase laths is found within a β matrix. The presence of these α laths is more noticeable when observing the micrographs of the sample printed with high *VED* (T1) in Figure 44. The high energy density potentially facilitated the growth of α-precipitates, thus resulting in the superior σ_T seen. The reduction in β-grain content is ultimately responsible for the decrease in ductility found with T1 when comparing the results with T2.
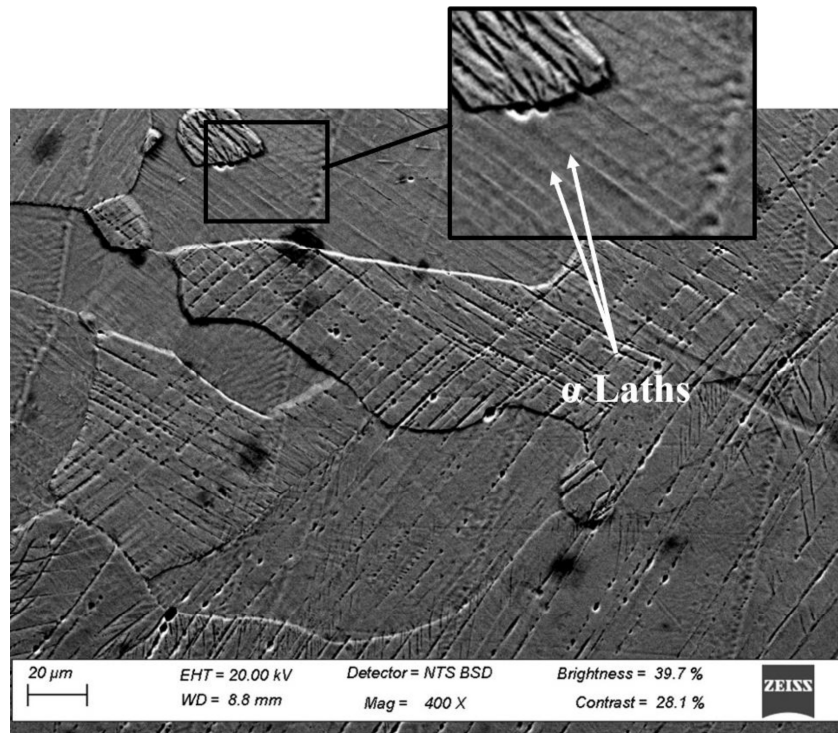
Figure 44: SEM micrograph of tensile samples printed using high VED showing evidence of α laths with β matrix

When considering the sample printed with medium *VED* (T2), the columnar prior-β grain growth is more noticeable than what is seen for T1. As expected, growth of said grains occurs across the melt pool boundaries in the build direction as seen in Figure 45. What is interesting to note is the severe columnar dendritic growth found within the grains.
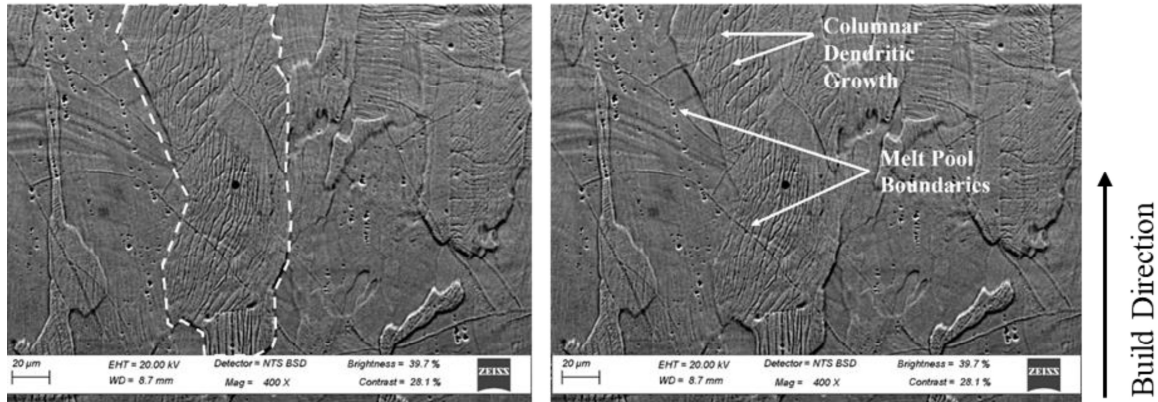
Figure 45: SEM micrographs showing evidence of prior-β grain and columnar dendritic growth in sample printed with medium VED

As with Beta 21S, a reduction in ductility and increase in σ_T is noticed when printing with higher *VED*. Recalling that Bakhshivash et al. (2019) examined the microstructures of samples printed at medium and high *VED* values, it was reported that the latter consisted of β- and fine secondary α-phase, while the former revealed the presence of only β-peaks in the XRD pattern. The steeper temperature gradient caused by the higher *VED* is likely the reason for this. As previously mentioned, the prolonged heating potentially facilitated the growth of these α laths seen in Figure 44. However, it is recommended that an XRD analysis be performed to confirm this for this study.

6.3.4 Heat Treatment Consideration for Ti-5-5-5-3

The tensile properties reported in this study show a strong resemblance to those reported for the wrought counterparts that have undergone solution treatment with the exception of σ_T and e_f. Ti-5-5-5-3 is used in the solution treated and aged condition. Therefore, an aging treatment for the as-built Ti-5-5-5-3 is considered, which would facilitate the growth of α-precipitates. This would improve the σ_T but would come at the expense of ductility.

In its current state, the presence of α' martensite is low due to the high amount of β-phase present that inhibits its formation. A study by Shekhar et al. (2015) performed a series of aging treatments at 450, 550, 600 and 650 °C for a duration of four hours each. Initially, a solution treatment was performed in which the samples were held at 885 °C for one hour and then water quenched. It was revealed that the addition of aging treatment resulted in an increase of σ_T and a decrease in ductility. The aging treatment performed at 650 °C caused a moderate increase in σ_T while maintaining its ductility to some degree. As such, this aging treatment is considered suitable for the built T-5-5-5-3 and provides a reasonable trade-off between strength and ductility.

6.4 Recommendations for Future Work

LPBF-produced Beta 21S and Ti-5-5-5-3 are still in their early phases of research. This can be concluded from the limited research papers available. Therefore, the research in this study can be used as a foundation from which to the investigate these alloys further.

The processing windows can be refined to include more accurate ranges of error to the contour lines. The predictive capabilities of the established models are limited to using the Archimedes' density principle. While it is not suggested that alternate methods be used to redefine the porosity responses, additional samples can be printed with parameter sets along 1, 0.5, and 0.25 % contour lines. These samples can be analyzed to provide an accurate range of error to the models using more accurate techniques, such as μ-CT scanning with high resolution.

Moreover, the optimal combinations of parameters used to achieve dense components will differ for different machines. However, one could argue that the processing window outlining combinations that offer density > 99% could be used as a starting point from which to select process parameters. The processing windows for each alloy will not be identical for every machine but it is likely that there will be overlap. How much the windows overlap is unknown. The degree to which the processing windows shift for different types of machines should be investigated to quantify this variation to provide a more general processing window. In addition to this, the quality of the melt pool should be considered to further refine the processing window.

Furthermore, the samples in this study can be used to define the microstructural evolution within the processing windows by using techniques such as XRD and electron backscatter diffraction (EBSD), and thereby perform various aging treatments to characterize the responses thereof. This would provide more insight into the influence of the process parameters on β-phase transformation and the degree to which Ti-5-5-5-3 and Beta 21S are hardenable. This could potentially reduce the amount of post-manufacturing heat treating needed to commission these alloys for end use.

Additional tensile samples were printed. These can be used to test the tensile behavior response to the heat treatments previously suggested. Alternatively, the tensile samples can be used to determine the performance when introducing tailored aging treatments according to the microstructural evolution.

This research also opens doors for collaborative research with other disciplines of engineering. Research focused on heat and mass transfer could potentially investigate the influence of the thermal properties of each alloy and provide deeper meaning into the influence of such properties on the proposed porosity windows.

7. CONCLUSION

The findings of this research are in accordance with the objectives set out in the introduction of this study and can be summarized herein. Recommendations for future work are also provided.

D-optimal design was implemented to define a set of processing parameters in Chapter 3 in the design of the experiment. Ti-6-4 was used as a baseline for this study due to its prominent presence in AM research. The processing window established for Ti-6-4, using the methods outlined, is in accordance with the literature. The methods were thus implemented on Beta 21S and Ti-5-5-5-3 to establish processing windows that outline parameter sets with which LPBF can be used to obtain dense components. The materials and methods discussed in Chapter 4 were used to print samples and analyze the data to create the porosity responses. The validity of the responses was assessed by comparing the predicted response with the observed data in Tables 36 and 37. The response of Ti-6-4 was compared to data in the literature to validate the processing window. The bounds of the processing windows were confirmed according to the expected pore-formation phenomena, viz. over melting (keyholing), under melting (lack-of-fusion), and balling. Therefore, the first objective has been met.

Using the processing window, parameter sets were selected where the density criterion (>99 %) was met and a variation in hardness and *VED* was found. The selected parameter sets were used to print tensile samples. The range of hardness was correlated with the *VED* used in which a proportional relationship was established. This relationship was deemed to be mainly influenced by hatch spacing. According to Equation 2, an increase in hatch spacing would result in a decrease in *VED*. An increase in hatch spacing causes a significant increase in porosity due to insufficient overlap.

The tensile properties established correlate well with what is reported in the literature. The results demonstrate competitive performance with the wrought counterparts in the solution-treated conditions. However, the behavior was shown to be more ductile in nature. Through a review of the relevant literature, it is suggested that some of this ductility can be sacrificed for an improvement in σ_T by implementing an aging treatment to facilitate the growth of α-precipitates (this was not directly investigated). Therefore, this study meets the second and third objectives to characterize the hardness and tensile properties and establish connections between these properties and the microstructure. Chapters 4, 5, and 6 report the materials, methods, results, and analyses used to meet these objectives.

Finally, recommendations for property improvements and further study are made in Chapter 6, meeting the last objective of this study.

It is shown that implementing D-optimal design to determine sets of viable parameters for LPBF is highly beneficial for studies in which resources are limited. As such, using such methods for other titanium alloys, as well as ferrous and nonferrous alloys, is recommended.

8. REFERENCES

Agarwal, N, Bhattacharjee, A, Ghosal, P, Nandy, TK, & Sagar, PK 2008, 'Heat treatment, microstructure and mechanical properties of a metastable β titanium alloy Timetal® 21S,' *Transactions of the Indian Institute of Metals*, vol. 61, no. 5, pp. 419–425.

Ahmed, M, Obeidi, M, Yin, S, & Lupoi, R 2022, 'Influence of processing parameters on density, surface morphologies and hardness of as-built Ti-5Al-5Mo-5V-3Cr alloy manufactured by selective laser melting,' *Journal of Alloys and Compounds*, vol. 910, p.164760.

Anderson, MJ & Whitcomb, PJ 2017, *DOE Simplified: Practical Tools for Effective Experimentation*, Productivity Press, New York.

ASTM Standard B311-13 2013, *Standard Test Method for Density of Powder Metallurgy (PM) Materials Containing Less than Two Percent Porosity*, ASTM International, West Conshohocken, retrieved at the Engineering & Forestry Library, Stellenbosch University.

ASTM Standard E348-10 2010, *Standard Test Method for Microindentation Hardness of Materials*, ASTM International, West Conshohocken, retrieved at the Engineering & Forestry Library, Stellenbosch University.

ASTM Standard E8/E8M – 21 2021, *Standard Test Methods for Tension Testing of Metallic Materials*, ASTM International, West Conshohocken, retrieved at the Engineering & Forestry Library, Stellenbosch University.

Bakhshivash, S, Asgari, H, Russo, P, Dibia, C, Ansari, M, Gerlich, A, & Toyserkani, E 2019, 'Printability and microstructural evolution of Ti-5553 alloy fabricated by modulated laser powder bed fusion,' *The International Journal of Advanced Manufacturing Technology*, vol. 103, no. 9-12, pp. 4399-4409.

Bernhard, G, Schade, C, Horvay, K & Sunday, K n.d., *Atomization of High Strength Titanium Alloys*. 1st edn., Hoeganaes Specialty Metal Powders, Cinnaminson, p.16.

Boyer, R., Welsch, G, & Collings, E 1994, *Materials Properties Handbook: Titanium Alloys*, ASM International, Ohio.

Brown, SGR, Cherry, JA, Davies, HM, Mehmood, S, Lavery, NP, & Sienz, J 2014, 'Investigation into the effect of process parameters on microstructural and physical

properties of 316L stainless steel parts by selective laser melting,' *International Journal of Advanced Manufacturing Technology*, vol. 76, no. 5-8, pp. 869-879.

Cain, V, Thijs, L, Van Humbeeck, J, Van Hooreweder, B, & Knutsen, R 2015, 'Crack propagation and fracture toughness of Ti6Al4V alloy produced by selective laser melting,' *Additive Manufacturing*, vol. 5, pp.68-76.

Callister, WD & Rethwisch, DG 2011, Material Science and Engineering. 8th edn., John Wiley & Sons, New Jersey.

Cheol Kim, H, Yeong Kim, D, Eun Lee, J, & Park, K 2017, 'Improvement of mechanical properties and surface finish of 3D-printed polylactic acid parts by constrained remelting,' *Advanced Materials Letters*, vol. 8, no. 12, pp. 1199-1203.

Colombo-Pulgarín, JC, Biffi, CA, *VED*ani, M, Celentano, DJ, Egea, AJS, Boccardo, AD, & Ponthot, J 2021, 'Beta titanium alloys processed by laser powder bed fusion: A review,' *Journal of Materials Engineering and Performance*, vol. 30, no. 9, pp. 6365-6388.

Cotton, J, Briggs, R, Boyer, R, Tamirisakandala, S, Russo, P, Shchetnikov, N, & Fanning, J 2015, 'State of the art in beta titanium alloys for airframe applications,' *JOM,* vol. 67, no. 6, pp. 1281-1303.

Dilip, J, Zhang, S, Teng, C, Zeng, K, Robinson, C, Pal, D, & Stucker, B 2017, 'Influence of processing parameters on the evolution of melt pool, porosity, and microstructures in Ti-6Al-4V alloy parts fabricated by selective laser melting,' *Progress in Additive Manufacturing*, vol. 2, no. 3, pp. 157-167.

Donachie, MJ 2010, *Titanium: A Technical Guide* 2nd edn., ASM International Materials Park, Ohio.

Dutrow, B & Clark, C 2020, *X-Ray Powder Diffraction (XRD),* Instrumentation and Analysis, viewed 20 October 2020, https://serc.carleton.edu/research_education/geochemsheets/techniques/XRD.html.

Elgiloy 2015, *Specialty Metals - Strip Products*, 1st edn., Elgiloy, Elgin, p.1.

Fousová, M, Vojtech, D, Kubásek J, Dvorsky, D, & Machová M 2015), '3D printing as an alternative to casting, forging and machining technologies,' *IOP Conference Series Materials Science and Engineering*, vol. 179, no. 1.

Gong, H, Rafi, K, Gu, H, Janaki Ram, G, Starr, T, & Stucker, B 2015, 'Influence of defects on mechanical properties of Ti–6Al–4V components produced by selective laser melting and electron beam melting,' *Materials & Design*, vol. 86, pp. 545-554.

Heiney, P 2018, *XRD Basics*, Datasqueeze Software, viewed 20 October 2020, https://www.physics.upenn.edu/~heiney/datasqueeze/basics.html.

Kolli, R & Devaraj, A 2018, 'A review of metastable beta titanium alloys,' *Metals*, vol. 8, no. 7, p.506.

Kumar, P, Prakash, O, & Ramamurty, U 2018, 'Micro-and meso-structures and their influence on mechanical properties of selectively laser melted Ti-6Al-4V,' *Acta Materialia*, vol. 154, pp. 246-260.

Li, C, Liu, Z, Fang, X, & Guo, Y 2018, 'Residual stress in metal additive manufacturing,' *Procedia CIRP*, vol. 71, pp.348-353.

Li, H, Ramezani, M, & Chen, ZW 2019, 'Dry sliding wear performance and behavior of powder bed fusion processed Ti–6Al–4V alloy,' *Wear*, vol. 440-441, p. 203103.

Macias-Sifuentes, M, Xu, C, Sanchez-Mata, O, Kwon, S, Atabay, S, Muñiz-Lerma, J, & Brochu, M 2021 'Microstructure and mechanical properties of β-21S Ti alloy fabricated through laser powder bed fusion,' *Progress in Additive Manufacturing*, vol. 6, no. 3, pp.417-430.

Malefane, L, du Preez, W, & Maringa, M 2017, 'High cycle fatigue properties of as-built Ti6Al4V (ELI) produced by direct metal laser sintering,' *South African Journal of Industrial Engineering*, vol. 28, no. 3.

Miller, DM 1984, 'Reducing transformation bias in curve fitting,' *The American Statistician*, vol. 38, no. 2, p. 124.

Moeinfar, K, Khodabakhshi, F, Kashani-bozorg, S, Mohammadi, M, & Gerlich, A 2022, 'A review on metallurgical aspects of laser additive manufacturing (LAM): Stainless steels, nickel superalloys, and titanium alloys,' *Journal of Materials Research and Technology*, vol. 16, pp.1029-1068.

Munk, J, Breitbarth, E, Siemer, T, Pirch, N, & Häfner, C 2022, 'Geometry effect on microstructure and mechanical properties in laser powder bed fusion of ti-Al-4V,' *Metals*, vol. 12, no. 3, p. 482.

Myers, RH & Montgomery, DC, 1995, *Response Surface Methodology: Process and Product Optimization Using Designed Experiments*, John Wiley and Sons, New York.

Myers, RH, Vining, G, Giovannitti-Jensen, A, & Myers, S 1992, 'Variance dispersion properties of second-order response surface designs,' *Journal of Quality Technology*, vol. 24, no. 1, pp.1-11.

Opini, VC, Salvador, CAF, Campo, KN, Lopes, ESN, Chaves, RR, & Caram, R 2016 'Alpha-phase precipitation and mechanical properties of Nb modified Ti-5553 alloy,' *Materials Science and Engineering*, vol. 670, pp. 112–121.

Parida, A & Maity, K 2019, 'Analysis of some critical aspects in hot machining of Ti-5553 superalloy: Experimental and FE analysis,' *Defence Technology*, vol. 15, no. 3, pp.344-352.

Pellizzari, M, Jam, A, Tschon, M, Fini, M, Lora, C, & Benedetti, M 2020), 'A 3D-printed ultra-low Young's modulus β-Ti alloy for biomedical applications,' *Materials*, vol. 13, no. 12, p.2792.

Pereira, T, Kennedy, J, & Potgieter, J 2019, 'A comparison of traditional manufacturing vs additive manufacturing, the best method for the job.' *Procedia Manufacturing*, vol. 30, pp.11-18.

Promoppatum, P, Onler, R, & Yao, S 2017, 'Numerical and experimental investigations of micro and macro characteristics of direct metal laser sintered Ti-6Al-4V products,' *Journal of Materials Processing Technology*, vol. 240, pp. 262-273.

Sánchez-Amaya, J, Pasang, T, Amaya-Vazquez, M, Lopez-Castro, J, Churiaque, C, Tao, Y, & Botana Pedemonte, F 2017, 'Microstructure and mechanical properties of Ti5553 butt welds performed by LBW under conduction regime,' *Metals*, vol. 7, no. 7, p.269.

Sefer, B 2014, 'Oxidation and alpha-case phenomena in titanium alloys used in aerospace industry,' Licentiate Degree in Engineering Materials, Luleå University of Technology, Sweden.

Shekhar, S, Sarkar, R, Kar, S, & Bhattacharjee, A 2015, 'Effect of solution treatment and aging on microstructure and tensile properties of high strength β titanium alloy, Ti-5Al-5V-5Mo-3Cr,' *Materials & Design*, vol. 66, pp. 596–610.

Sherov, K, Ainabekova, S, Kuanov, I, Myrzakhmet, B, Bekzhanov, Y, Gabdyssalik, R, Mazdubay, A, Kamarov, A, & Sherov, A 2022, 'Research of temperature distribution

in the process of thermo-frictional cutting of titanium alloy Ti-5553,' *Journal of Applied Engineering Science*, vol. 20, no. 2, pp.400-407.

Sing, S, Yeong, W, & Wiria, F, 2016, 'Selective laser melting of titanium alloy with 50 wt% tantalum: Microstructure and mechanical properties,' *Journal of Alloys and Compounds*, vol. 660, pp.461-470.

Valente, E, Gundlach, C, Christiansen, T, & Somers, M 2019, 'Effect of scanning strategy during selective laser melting on surface topography, porosity, and microstructure of additively manufactured Ti-6Al-4V,' *Applied Sciences*, vol. 9, no. 24, p.5554.

Wang, Z, Xiao, Z, Tse, Y, Huang, C, & Zhang, W 2019, 'Optimization of processing parameters and establishment of a relationship between microstructure and mechanical properties of SLM titanium alloy,' *Optics & Amp; Laser Technology*, vol. 112, pp.159-167.

Wilson, T 2017, 'β21S titanium alloy heat treatment development and improvement,' Bachelor of Engineering, University of Queensland, Australia.

Yadroitsev, I, Gusarov, A, Yadroitsava, I, & Smurov, I, 2010, 'Single track formation in selective laser melting of metal powders,' *Journal of Materials Processing Technology*, vol. 210, no. 12, pp.1624-1631.

Yan, F, Xiong, W, & Faierson, E 2017, 'Grain structure control of additively manufactured metallic materials,' *Materials*, vol. 10, no. 11, p. 1260.

Zhang, J, Bermingham, M, Otte, J, Liu, Y, & Dargusch, M 2022, 'Towards uniform and enhanced tensile ductility of additively manufactured Ti−5Al−5Mo−5V−3Cr alloy through designing gradient interlayer deposition time,' *Scripta Materialia*, vol. 223, p. 115066.

Appendix A: Experimental Methodology

This section is used in conjunction with Section 4 to illustrate the process in which the experimental procedures were carried out and serves to keep track of samples with regards to the experimental methods applied to each one.
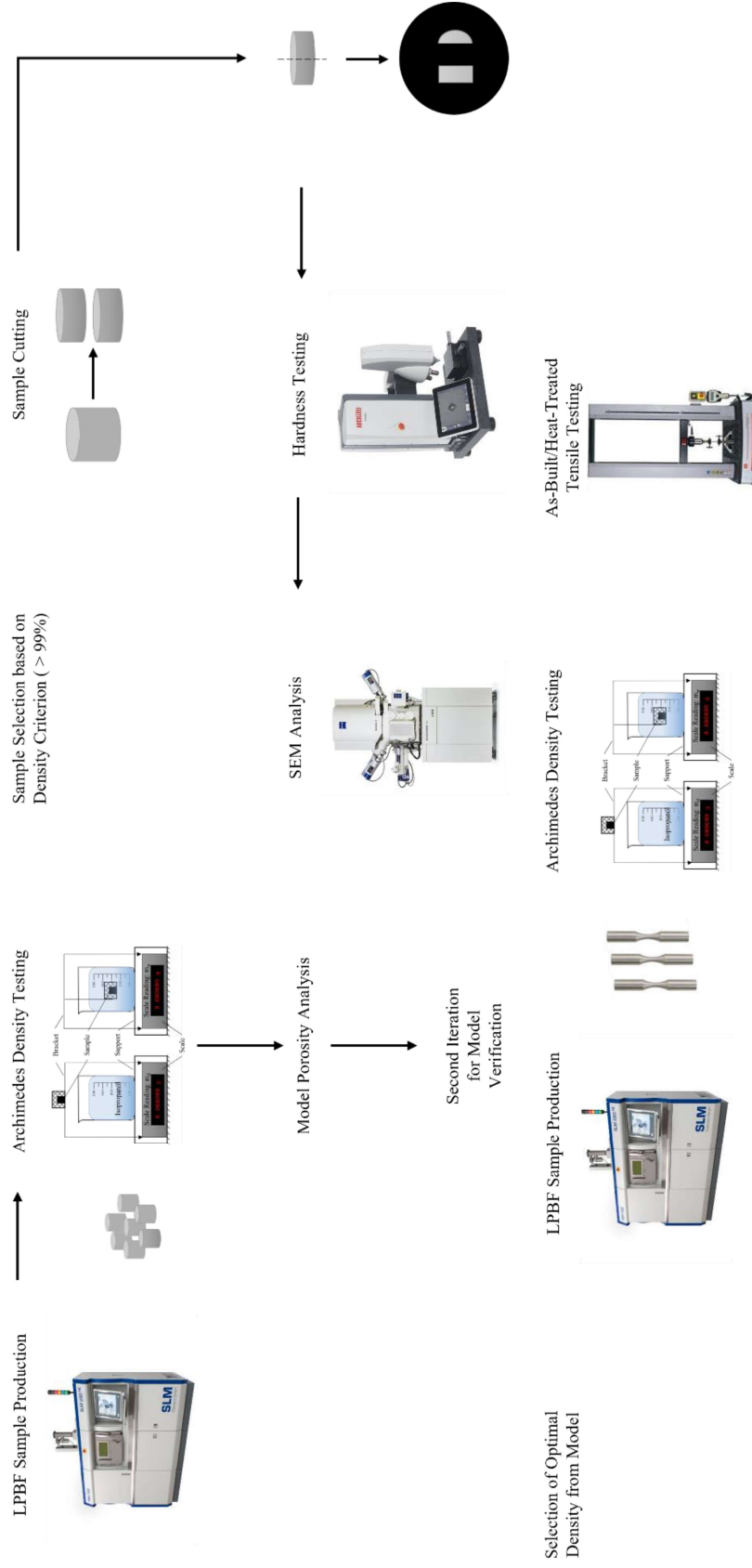

Figure 46: A diagram depicting the experimental methodology carried out on of Ti-5-5-5-3 and Beta 21S cylindrical samples

Table 39: Record of Experimental Procedures Applied to Beta 21S Samples

Sample Number	Archimedes Density Testing	Sample Selected for Hardness Testing	Parameters Selected for Tensile Testing	OM Analysis	SEM Analysis
1 (350-1167-40)	✓				
2 (350-2500-40)	✓				
3 (205-1296-80)	✓				
4 (143-1447-40)	✓				
5 (350-1167-91)	✓				
6 (120-400-110)	✓	✓		✓	
7 (120-400-110)	✓				
8 (350-1167-110)	✓				
9 (205-1296-80)	✓				
10 (253-1576-40)	✓				
11 (80-400-40)	✓				
12 (350-2500-80)	✓				
13 (80-400-40)	✓				
14 (350-2500-110)	✓				
15 (248-2500-40)	✓	✓			
16 (350-1167-40)	✓	✓			
17 (350-2500-40)	✓				
18 (197-657-40)	✓	✓		✓	
19 (248-2500-110)	✓				
20 (350-2500-110)	✓				
21 (248-2500-110)	✓	✓		✓	
22 (80-400-70)	✓				
23 (248-2500-40)	✓				
24 (80-808-40)	✓	✓			
25 (80-400-70)	✓				
26 (350-1167-110)	✓				
27 (350-1167-40)	✓	✓	✓		✓
28 (248-2500-70)	✓				

Sample Number	Archimedes Density Testing	Sample Selected for Hardness Testing	Parameters Selected for Tensile Testing	OM Analysis	SEM Analysis
29 (274-913-60)	✓	✓			
30 (248-2500-40)	✓				
31 (161-1622-110)	✓				
32 (205-1296-80)	✓				
33 (80-808-110)	✓				
34 (183-609-110)	✓				
35 (183-609-110)	✓	✓			
36 (80-808-110)	✓	✓		✓	
37 (248-2500-70)	✓	✓	✓		✓
38 (332-1849-60)	✓				
39 (350-2046-110)	✓				
40 (205-1296-80)	✓	✓			
41 (197-657-40)	✓	✓			
42 (270-1829-90)	✓				
43 (350-2500-40)	✓				
44 (350-1167-80)	✓				
45 (80-400-40)	✓	✓	✓		✓
46 (80-808-110)	✓				
47 (205-1296-80)	✓				
48 (350-1167-110)	✓	✓			
49 (143-1447-40)	✓				
50 (248-2500-110)	✓				

Table 40: Record of Experimental Procedures Applied to Ti-5-5-5-3 Samples

Sample Number	Archimedes Density Testing	Parameters Selected for Hardness Testing	Parameters Selected for Tensile Testing	OM Analysis	SEM Analysis
1 (350-1167-40)	✓				
2 (350-2500-40)	✓				
3 (205-1296-80)	✓				
4 (143-1447-40)	✓				
5 (350-1167-91)	✓				
6 (120-400-110)	✓	✓		✓	
7 (120-400-110)	✓				
8 (350-1167-110)	✓				
9 (205-1296-80)	✓				
10 (253-1576-40)	✓				
11 (80-400-40)	✓				
12 (350-2500-80)	✓				
13 (80-400-40)	✓				
14 (350-2500-110)	✓				
15 (248-2500-40)	✓	✓			
16 (350-1167-40)	✓	✓			
17 (350-2500-40)	✓				
18 (197-657-40)	✓	✓		✓	
19 (248-2500-110)	✓				
20 (350-2500-110)	✓				
21 (248-2500-110)	✓	✓		✓	
22 (80-400-70)	✓				
23 (248-2500-40)	✓				
24 (80-808-40)	✓	✓			
25 (80-400-70)	✓				
26 (350-1167-110)	✓				
27 (350-1167-40)	✓	✓	✓		✓
28 (248-2500-70)	✓				

Sample Number	Archimedes Density Testing	Sample Selected for Hardness Testing	Parameters Selected for Tensile Testing	OM Analysis	SEM Analysis
29 (274-913-60)	✓	✓			
30 (248-2500-40)	✓				
31 (161-1622-110)	✓				
32 (205-1296-80)	✓				
33 (80-808-110)	✓				
34 (183-609-110)	✓				
35 (183-609-110)	✓	✓			
36 (80-808-110)	✓	✓		✓	
37 (248-2500-70)	✓	✓	✓		✓
38 (332-1849-60)	✓				
39 (350-2046-110)	✓				
40 (205-1296-80)	✓	✓			
41 (197-657-40)	✓	✓			
42 (270-1829-90)	✓				
43 (350-2500-40)	✓				
44 (350-1167-80)	✓				
45 (80-400-40)	✓	✓	✓		✓
46 (80-808-110)	✓				
47 (205-1296-80)	✓				
48 (350-1167-110)	✓	✓			
49 (143-1447-40)	✓				
50 (248-2500-110)	✓				

Appendix B: Detailed Design Matrix and Porosity Data

The detailed design matrix generated using *Design-Expert* is reported in Table 41 below.

Table 41: Detailed Experimental Design Matrix

Run	VED [J/mm^3]	Beta 21S Scaled Porosity [%]	Ti-5-5-5-3 Scaled Porosity [%]
1 (350-1167-40)	250	0.722	0.452
2 (350-2500-40)	117	Fail	Fail
3 (205-1296-80)	66	0.672	0.339
4 (143-1447-40)	82	0.516	0.238
5 (350-1167-91)	91	0.763	0.309
6 (120-400-110)	91	1.749	1.906
7 (120-400-110)	91	1.564	1.999
8 (350-1167-110)	91	0.603	0.448
9 (205-1296-80)	66	0.549	0.340
10 (253-1576-40)	134	0.196	0.159
11 (80-400-40)	167	0.082	0.185
12 (350-2500-80)	58	0.900	0.454
13 (80-400-40)	167	0.210	0.079
14 (350-2500-110)	42	1.069	0.557
15 (248-2500-40)	83	0.354	0.192
16 (350-1167-40)	250	0.532	0.290
17 (350-2500-40)	117	Fail	Fail
18 (197-657-40)	250	0.924	1.070
19 (248-2500-110)	30	1.611	1.027
20 (350-2500-110)	42	1.053	0.665
21 (248-2500-110)	30	1.804	1.055
22 (80-400-70)	95	0.418	0.269
23 (248-2500-40)	83	0.503	0.239
24 (80-808-40)	83	0.744	0.422
25 (80-400-70)	95	0.359	0.259
26 (350-1167-110)	91	0.750	0.254
27 (350-1167-40)	250	0.546	0.400
28 (248-2500-70)	47	0.658	0.169
29 (274-913-60)	167	0.661	0.411
30 (248-2500-40)	83	0.439	0.300
31 (161-1622-110)	30	1.854	1.170

Run	VED [J/mm³]	Beta 21S Scaled Porosity [%]	Ti-5-5-5-3 Scaled Porosity [%]
32 (205-1296-80)	66	0.576	0.360
33 (80-808-110)	30	2.181	1.490
34 (183-609-110)	91	1.162	0.878
35 (183-609-110)	91	0.895	0.795
36 (80-808-110)	30	1.987	1.280
37 (248-2500-70)	47	0.501	0.241
38 (332-1849-60)	100	Fail	Fail
39 (350-2046-110)	52	0.759	0.345
40 (205-1296-80)	66	0.595	0.360
41 (197-657-40)	250	0.987	1.169
42 (270-1829-90)	55	0.804	0.340
43 (350-2500-40)	117	Fail	Fail
44 (350-1167-80)	125	0.677	0.258
45 (80-400-40)	167	0	0
46 (80-808-110)	30	1.773	1.139
47 (205-1296-80)	66	0.487	0.351
48 (350-1167-110)	91	0.566	0.316
49 (143-1447-40)	82	0.454	0.267
50 (248-2500-110)	30	2.227	1.160

Table 42: Mean Porosity of Samples Stipulated on Processing Windows of Ti-6-4

No.	VED [J/mm³]	Mean Porosity [%]
1	250	0.40
2	250	1.54
3	167	0.24
4	83	0.39
5	82	0.37
6	134	0.00
7	83	0.27
8	125	0.38
9	58	0.41
10	66	0.32
11	91	0.29
12	52	0.46
13	42	0.88
14	91	1.25
15	91	2.46
16	30	2.88
17	30	1.94
18	30	2.32

Table 43: Mean Porosity of Samples Stipulated on Processing Windows of Beta 21S

No.	VED [J/mm^3]	Mean Porosity [%]
1	250	0.60
2	250	0.96
3	167	0.10
4	83	0.74
5	82	0.49
6	134	0.20
7	83	0.43
8	125	0.68
9	58	0.90
10	66	0.58
11	91	0.67
12	52	0.76
13	42	1.06
14	91	1.03
15	91	1.66
16	30	1.98
17	30	1.85
18	30	1.88

Table 44: Mean Porosity of Samples Stipulated on Processing Windows of Ti-5-5-5-3

No.	VED [J/mm^3]	Mean Porosity [%]
1	250	0.38
2	250	1.12
3	167	0.09
4	83	0.42
5	82	0.25
6	134	0.16
7	83	0.24
8	125	0.26
9	58	0.45
10	66	0.35
11	91	0.33
12	52	0.34
13	42	0.61
14	91	0.84
15	91	1.95
16	30	1.30
17	30	1.17
18	30	1.08

Appendix C: Model Diagnostics

Table 45: Legend for Model Diagnostics

Key	Key Description
1	p-Value Criterion
2	AICc Criterion
3	BIC Criterion
4	Adjusted R^2 Criterion
A	Laser Power
B	Scan Speed
C	Hatch Spacing

Table 46: Significance of Terms in Quadratic Response of Ti-6-4

	A	B	C	AB	AC	BC	A^2	B^2	C^2
1	✓	✓	✓	✓	✓	✓	✗	✓	✓
2	✓	✓	✓	✓	✓	✓	✗	✓	✓
3	✓	✓	✓	✓	✓	✓	✗	✓	✓
4	✓	✓	✓	✓	✓	✓	✓	✓	✓

Table 47: Significance of Terms in Cubic Response of Ti-6-4

	A	B	C	AB	AC	BC	A^2	B^2	C^2	ABC	A^2B	A^2C	AB^2	AC^2	B^2C	BC^2	A^3	B^3	C^3
1	✓	✓	✓	✓	✓	✓	✓	✓	✓	✗	✗	✓	✗	✓	✓	✗	✗	✗	✓
2	✓	✓	✓	✓	✓	✓	✓	✓	✓	✗	✗	✓	✗	✓	✓	✗	✗	✗	✓
3	✓	✓	✓	✓	✓	✓	✓	✓	✓	✗	✗	✓	✗	✓	✓	✗	✗	✗	✓
4	✓	✓	✓	✓	✓	✓	✓	✓	✓	✓	✓	✓	✓	✓	✓	✓	✓	✓	✓

Figure 47: A comparison between the a) inclusion and b) removal of terms from the quadratic response on the normal plot of residual for Ti-6-4
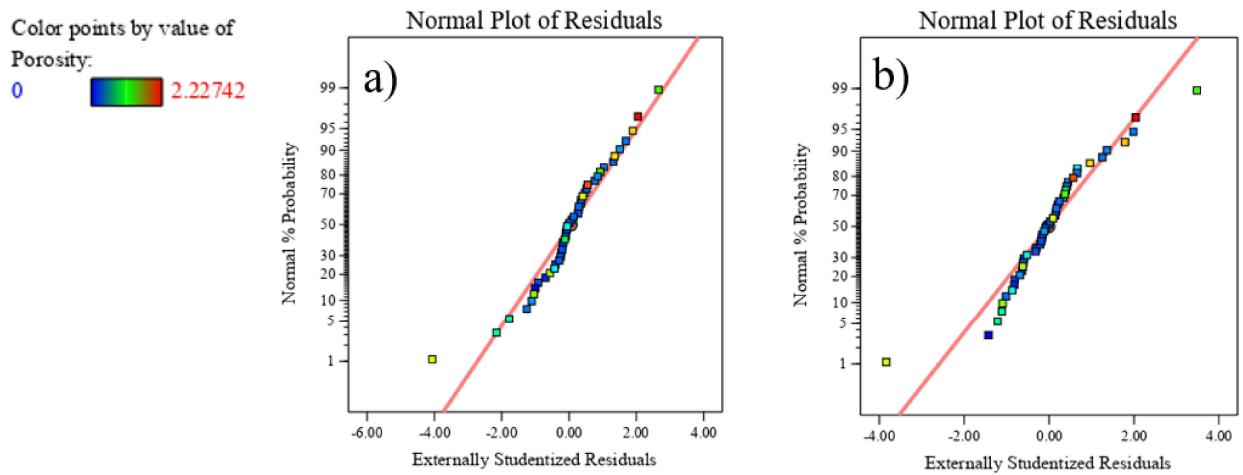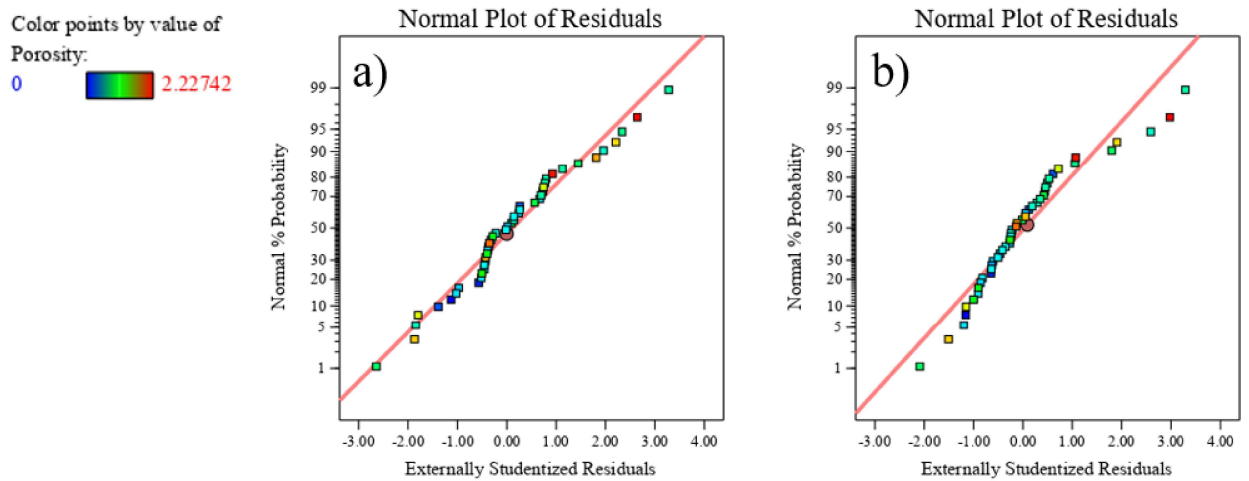

Figure 48: A comparison between a) inclusion and b) removal of terms from the cubic response on the normal plot of residual for Ti-6-4

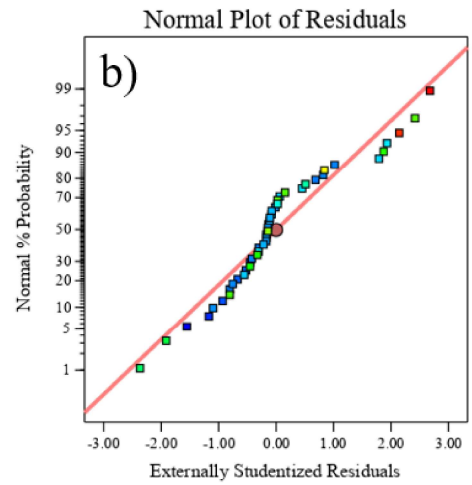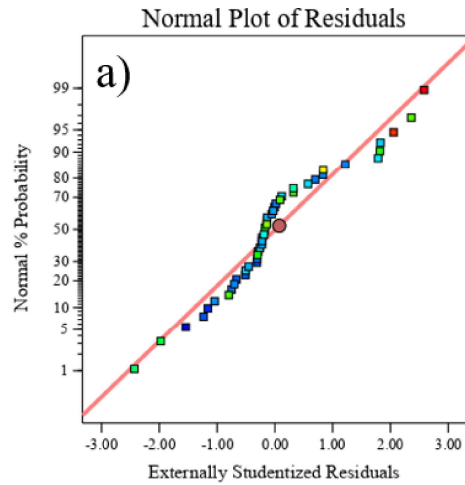*Table 48: Significance of Terms in Quadratic Response of Beta 21S*

	A	B	C	AB	AC	BC	A²	B²	C²
1	✓	✓	✓	X	✓	✓	X	X	✓
2	✓	✓	✓	X	✓	✓	X	X	✓
3	✓	✓	✓	X	✓	✓	X	X	✓
4	✓	✓	✓	✓	✓	✓	✓	✓	✓

Table 49: Significance of Terms in Cubic Response of Beta 21S

101

	A	B	C	A B	A C	B C	A²	B²	C²	A B C	A² B	A² C	A B²	A C²	B² C	B C²	A³	B³	C³
1	✓	✓	✓	✓	✓	✓	✓	✓	✓	✗	✓	✓	✗	✗	✗	✗	✗	✗	✓
2	✓	✓	✓	✓	✓	✓	✓	✓	✓	✗	✓	✓	✗	✗	✗	✗	✗	✗	✓
3	✓	✓	✓	✓	✓	✓	✓	✓	✓	✗	✓	✓	✗	✗	✗	✗	✗	✗	✓
4	✓	✓	✓	✓	✓	✓	✓	✓	✓	✓	✓	✓	✓	✓	✓	✓	✓	✓	✓

Figure 49: A comparison between the a) inclusion and b) removal of terms from the quadratic response on the normal plot of residual for Beta 21S

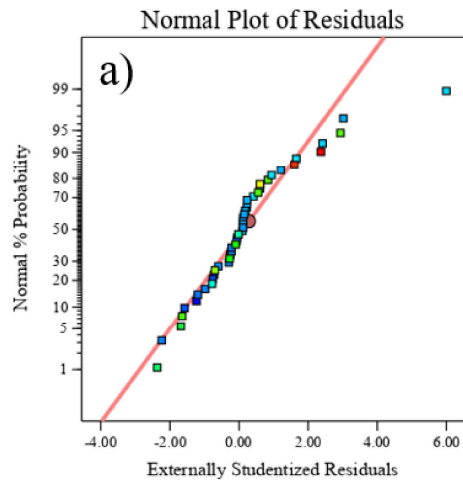*Figure 50: A comparison between the a) inclusion and b) removal of terms from the cubic response on the normal plot of residual for Beta 21S*

Table 50: Significance of Terms in Quadratic Response of Ti-5-5-5-3

	A	B	C	AB	AC	BC	A²	B²	C²
1	✓	✓	✓	✗	✓	✓	✓	✓	✓

102

2	✓	✓	✓	✗	✓	✓	✓	✓	✓
3	✓	✓	✓	✗	✓	✓	✓	✓	✓
4	✓	✓	✓	✓	✓	✓	✓	✓	✓

Table 51: Significance of Terms in Cubic Response of Ti-5-5-5-3

	A	B	C	A B	A C	B C	A²	B²	C²	A B C	A² B	A² C	A B²	A C²	B² C	B C²	A³	B³	C³
1	✓	✓	✓	✓	✓	✓	✓	✓	✓	✗	✗	✓	✗	✓	✓	✗	✗	✗	✓
2	✓	✓	✓	✓	✓	✓	✓	✓	✓	✗	✗	✓	✗	✓	✓	✗	✗	✗	✓
3	✓	✓	✓	✓	✓	✓	✓	✓	✓	✗	✗	✓	✗	✓	✓	✗	✗	✗	✓
4	✓	✓	✓	✓	✓	✓	✓	✓	✓	✓	✓	✓	✓	✓	✓	✓	✓	✓	✓

Figure 51: A comparison between the a) inclusion and b) removal of terms from the quadratic response on the normal plot of residual for Ti-5-5-5-3
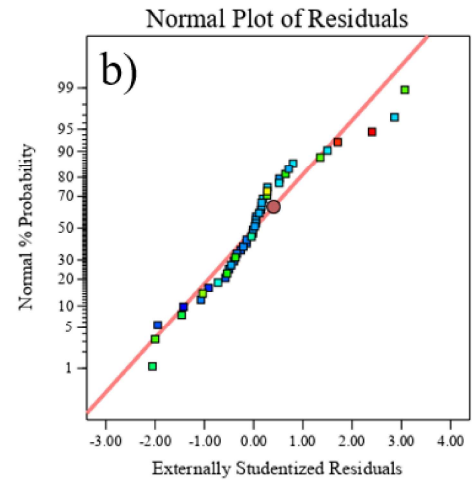
Figure 52: A comparison between the a) inclusion and b) removal of terms from the cubic response on the normal plot of residual for Ti-5-5-5-3

Appendix D: Tensile Sample and Property Information
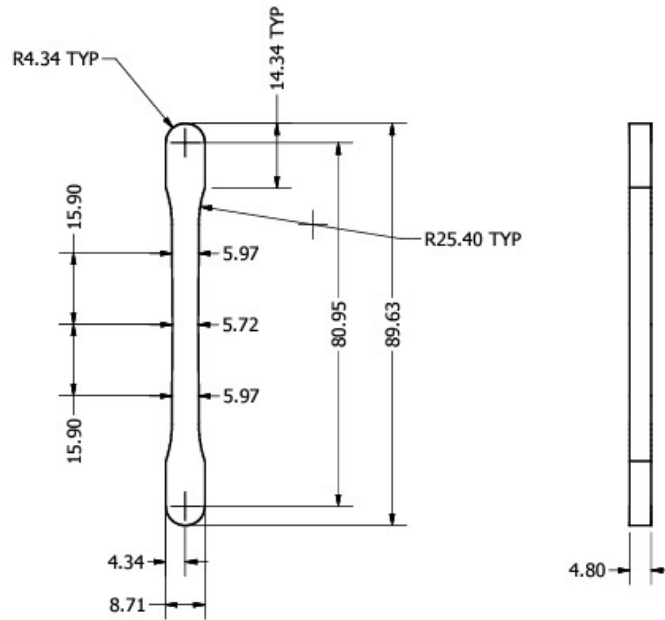
Figure 53: Drawing according to which the STL file to produce tensile samples were made. Dimensions and geometry were used as per those stipulated in ASTM Standard E8/E8M – 21 (2021).
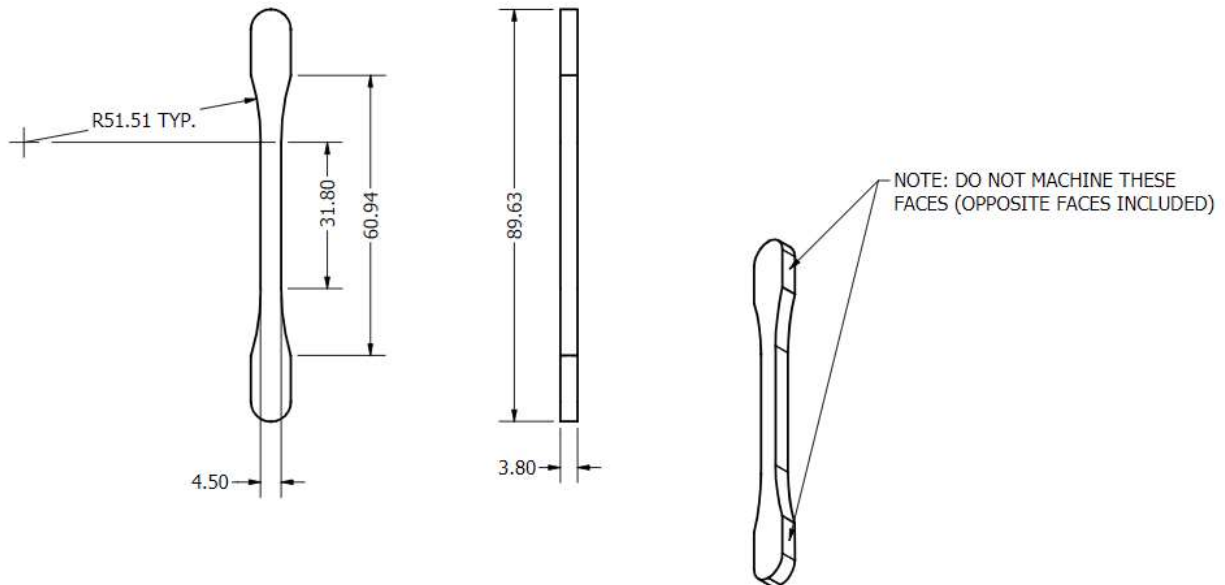
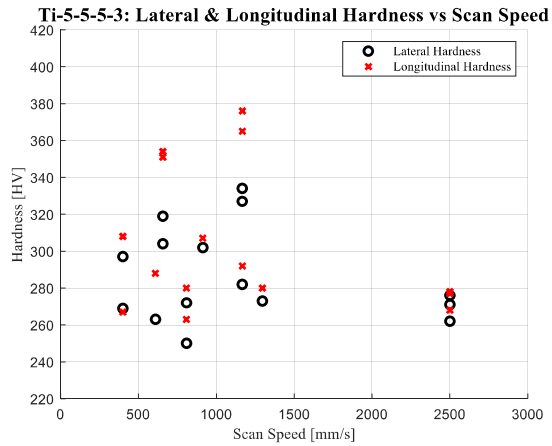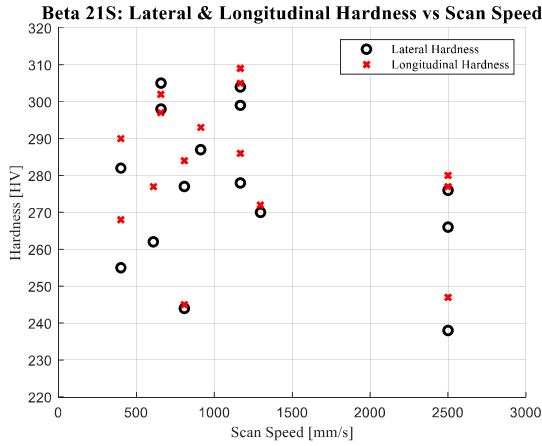*Figure 54: Drawing according to which tensile samples were machined*

105

Figure 55: A visual representation of the relationship between lateral/longitudinal hardness and scan speed for Beta 21S and Ti-5-5-5-3
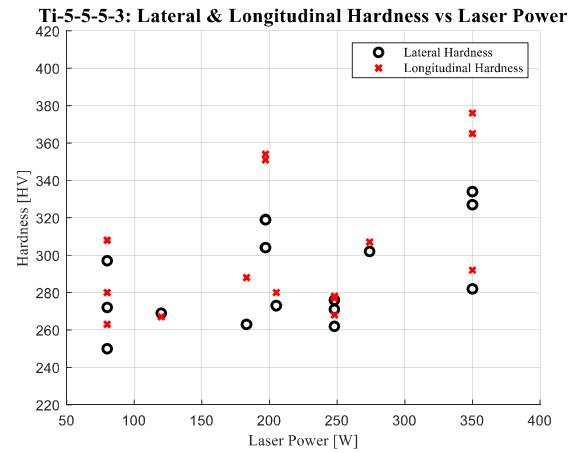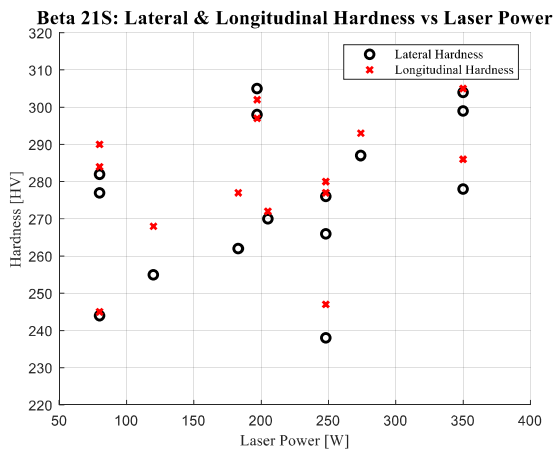
Figure 56: A visual representation of the relationship between lateral/longitudinal hardness and laser power for Beta 21S and Ti-5-5-5-3
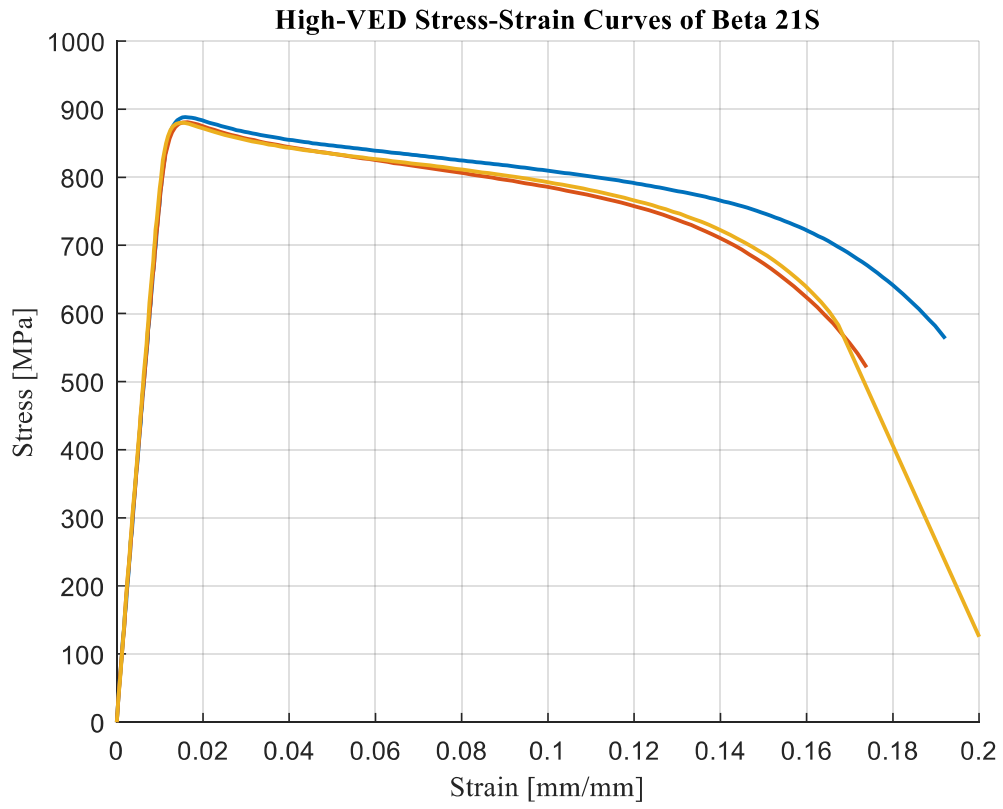
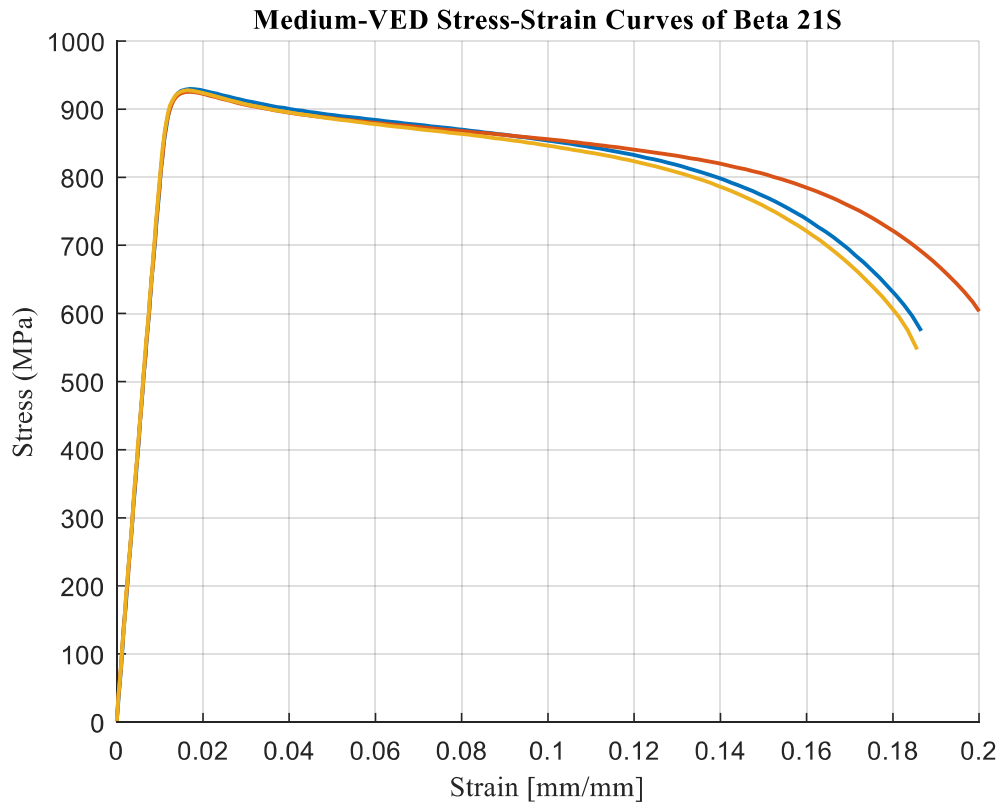*Figure 57: Stress-strain curve of Beta 21S samples printed with high VED*

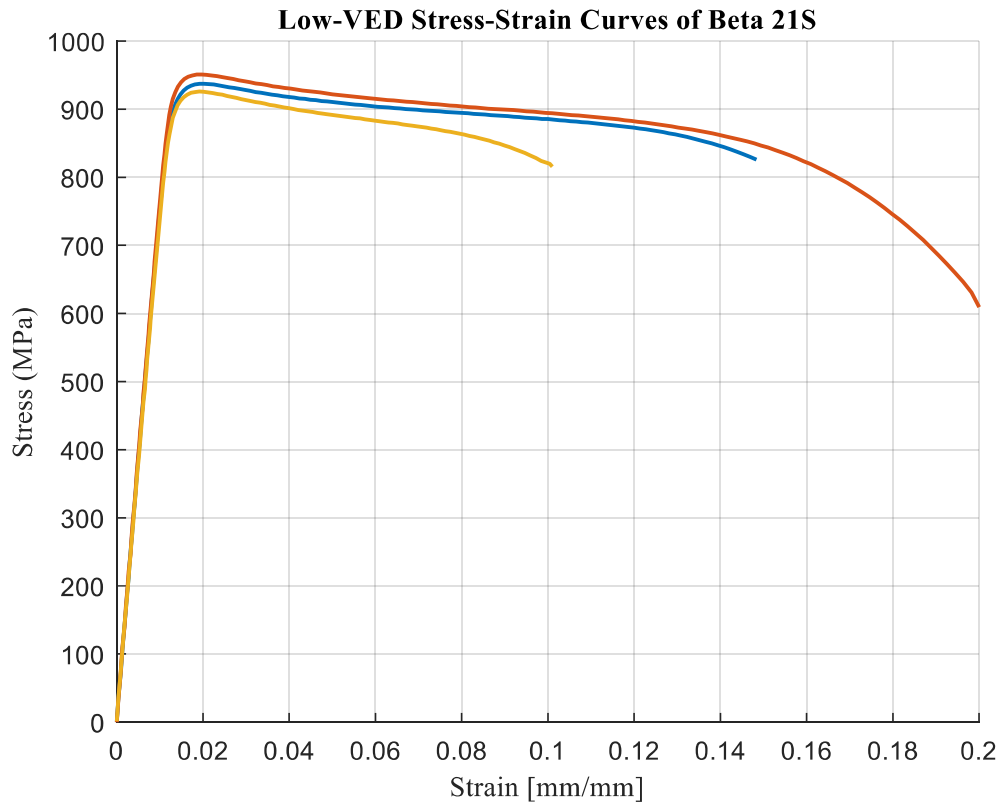*Figure 58: Stress-strain curve of Beta 21S samples printed with medium VED*

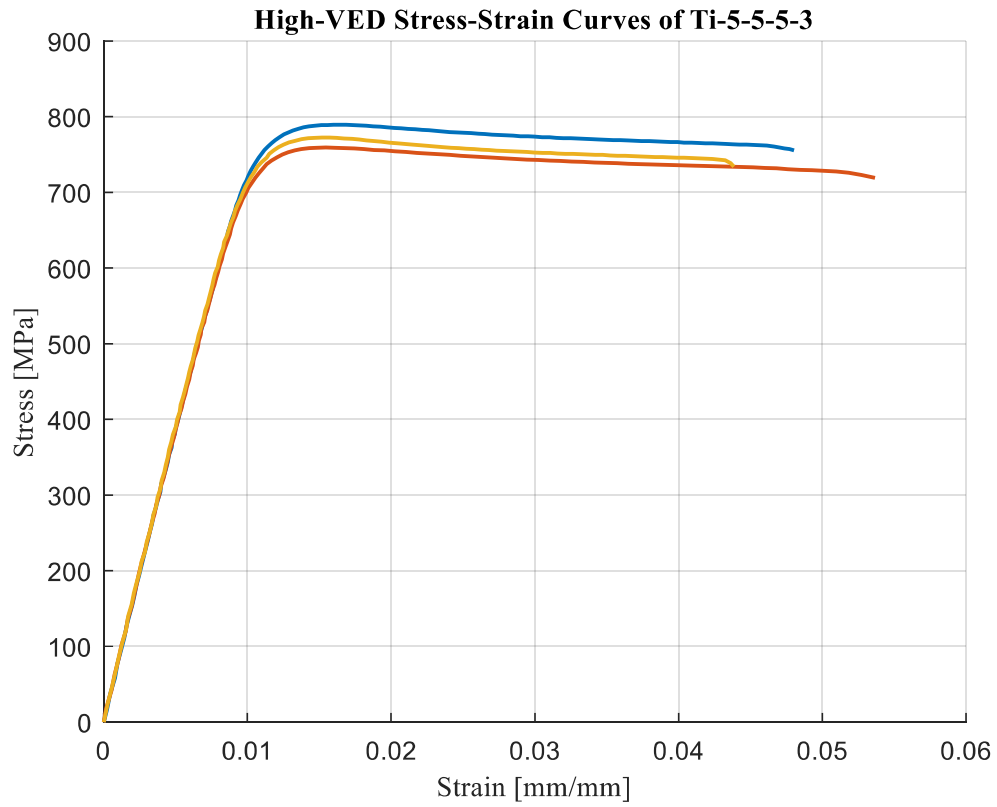*Figure 59: Stress-strain curve of Beta 21S samples printed with low VED*

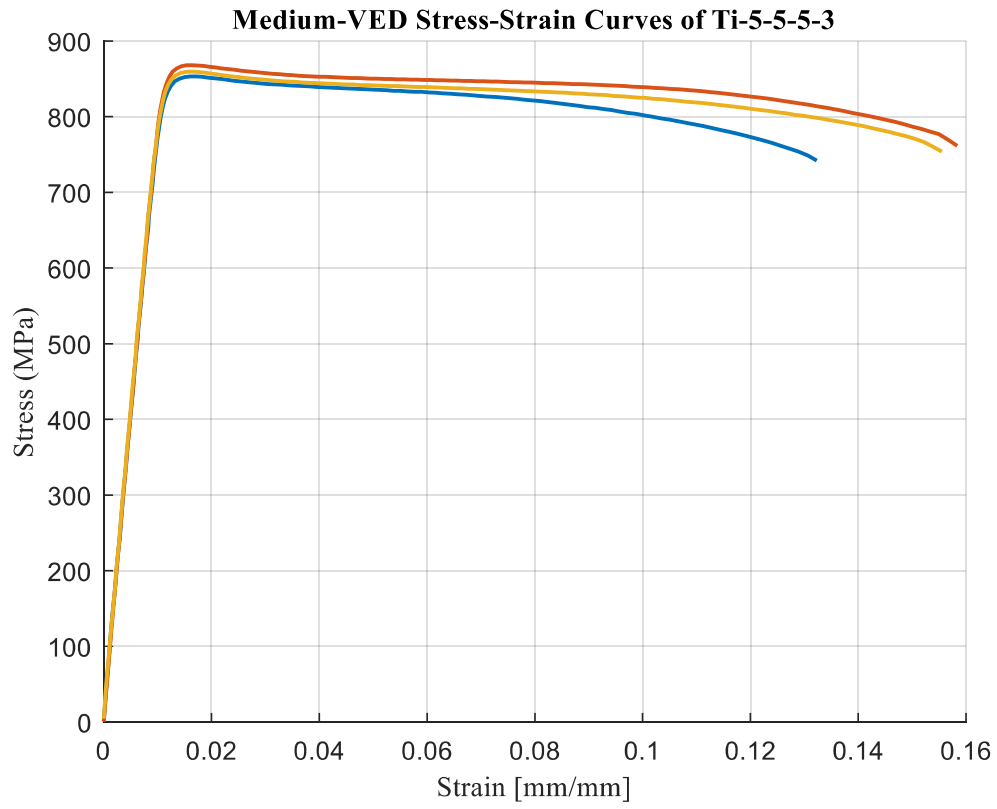*Figure 60: Stress-strain curve of Ti-5-5-5-3 samples printed with high VED*

Figure 61: Stress-strain curve of Ti-5-5-5-3 samples printed with medium VED